5-2010

Polymeric Microsensors for Intraoperative Contact Pressure Measurement

Emily R. Pritchard
epritchard@utk.edu

To the Graduate Council:

I am submitting herewith a dissertation written by Emily R. Pritchard entitled "Polymeric Microsensors for Intraoperative Contact Pressure Measurement." I have examined the final electronic copy of this dissertation for form and content and recommend that it be accepted in partial fulfillment of the requirements for the degree of Doctor of Philosophy, with a major in Biomedical Engineering.

Mohamed R. Mahfouz, Major Professor

We have read this dissertation and recommend its acceptance:

William R. Hamel, Richard D. Komistek, Wei He, Ray Wasielewski

Accepted for the Council:

Carolyn R. Hodges

Vice Provost and Dean of the Graduate School

(Original signatures are on file with official student records.)

To the Graduate Council:

I am submitting herewith a dissertation written by Emily Reagan Pritchard entitled “Polymeric Microsensors for Intraoperative Contact Pressure Measurement.” I have examined the final electronic copy of this dissertation for form and content and recommend that it be accepted in partial fulfillment of the requirements for the degree of Doctor of Philosophy, with a major in Biomedical Engineering.

Mohamed R. Mahfouz , Major Professor

We have read this dissertation
and recommend its acceptance:

William R. Hamel.

Richard D. Komistek

Wei He

Ray C. Wasielewski

Accepted for the Council:

Carolyn R. Hodges
Vice Provost and Dean of the Graduate School

(Original signatures are on file with official student records.)

Polymeric Microsensors for Intraoperative Contact Pressure Measurement

A Dissertation Presented for the
Doctor of Philosophy Degree
The University of Tennessee, Knoxville

Emily Pritchard
May 2010

Dedication

"But by the grace of God I am what I am, and his grace to me was not without effect."
1 Corinthians 15:10a

I thank God for what he has given me, and I dedicate this dissertation to my wonderful husband for his unwavering love and support.

Acknowledgements

I am grateful to the many people who have helped me grow and have supported me as I worked on this dissertation, especially my advisor and mentor Dr. Mohamed Mahfouz, who got me excited about MEMS and whose ideas on clinical applications got this whole project rolling. Thank you for mentoring me and exposing me to many of the facets of biomedical engineering; I would not be the engineer I am today without the Cornell training, all the conference presentations, and free reign to explore. The collaborative environment, interdisciplinary classes, research, and advice form the framework which supports this proposal.

There are many others who have helped in experimental assistance, use of equipment, guidance on relevant theories, and ongoing support for my work. I thank Dr. Hamel for his thoughtfulness and care when others overlooked; I thank Dr. Komistek for his level head at critical moments. Dr. Wasielewski I would like to thank for his contagious enthusiasm and clinical advice. I thank Dr. He for her graceful example as a new faculty member. I am grateful to Dr. Gary Alley for his unabated encouragement, solid leadership example, and use of ORNL cleanroom space. I would like to thank Dr. Penumadu and David Lane for their help in mechanical testing. Many thanks to Dr. Fathy for his responsiveness and lessons on grants and peer review. Thanks to Dr. Islam for support in circuit design. Thanks to Dr. Reece Roth and Sirous Nourgostar, who graciously allowed me use of surface testing equipment.

I thank both past and present students at the Center for Musculoskeletal Research for all the camaraderie and support. Specifically, I would like to thank Boyd Evans III for his patience and thoughtful advice. Thank you, Gary To, for showing me the tricks of circuit design. Thank you to Sazia Eliza and Mohammad Haider for their careful design and electrical testing, and for teaching me how. I am also grateful to Michael Kuhn, Brandon Merkl, Emam El Hak ElFatah, Brian Doll, Andrea North, and many more. And last but certainly not least, thanks to Rebecca Robertson for keeping me straight on the administrative side.

Abstract

Biocompatible sensors have been demonstrated using traditional microfabrication techniques modified for polymer substrates and utilize only materials suitable for implantation or bodily contact. Sensor arrays for the measurement of the load condition of polyethylene spacers in the total knee arthroplasty (TKA) prosthesis have been developed. Arrays of capacitive sensors are used to determine the three-dimensional strain within the polyethylene prosthesis component. Data from these sensors can be used to give researchers a better understanding of component motion, loading, and wear phenomena for a large range of activities. This dissertation demonstrates both analytically and experimentally the fabrication of these sensor arrays using biocompatible polymer substrates and dielectrics while preserving industry-standard microfabrication processing for micron-level resolution.

An array of sensors for real-time measurement of pressure profiles is the long-term goal of this research. A custom design using capacitive-based sensors is an excellent selection for such measurement, giving high spatial resolution across the sensing surface and high load resolution for pressures applied normal to that surface while operating at low power.

Table of Contents

List of Figures

List of Tables

Symbols and Abbreviations

A	area, matrix
ACL	anterior cruciate ligament
aF	attofarad, 1×10^{-18} Farads
A^T	transpose of matrix A
Au	gold
C	Capacitance, Centigrade
C2V	Capacitance to Voltage
CDC	Capacitance to Digital Conversion
CNF	Cornell Nanofabrication Facility
E	electric field, elastic modulus
F	Farad, force
FR-4	a type of flame retardant printed circuit board
HMDS	hexmethyldisilazane, $C_6H_{19}NSi_2$
HP-IB	Hewlett-Packard instrumentation bus
HTG	Hybrid Technology Group
i	discrete point, counter
k	modulus, number of discrete points on either side of point of interest in filter window
kPa	kilopascals

l	length
LCR	inductance, capacitance, and resistance
m	meter
μm	micrometer, 1×10^{-6} meters
min	minutes
mm	millimeters
MPa	megapascals
MUX	multiplexer
n	number of, counter
N	Newtons, Nitrogen
OA	osteoarthritis
PE	polyethylene
pF	picofarad 1×10^{-12} Farads
psi	pounds per square inch
P	polarization
PCL	posterior cruciate ligament
PE	polyethylene
PI	polyimide
q	charge
RMS	root mean squared
s	strain, seconds

Si	silicon
SMB	sub-miniature B
TKA	Total Knee Arthroplasty
UHMWPE	ultrahigh molecular weight polyethylene
w	transformation coordiante
χ_e	electric susceptibility
δ	offset amount
ε	permittivity
ε_0	permittivity of free space
ε_r	relative permittivity
σ	stress
ψ	field
ϕ	flux
γ	shear strain
ν	Poisson's ratio
ρ_v	charge density
Δ	difference, change
∇	gradient

Chapter 1. Force Sensing in Surgical Navigation

The need for flexible pressure mapping systems for non-planar surfaces has been recognized by several research fields, particularly biomedical measurements and robotics. These applications often require high sensitivity in low pressure ranges, up to about 1 megaPascal (MPa). Two dimensional pressure profiling is useful in determining contact area and inference of stress concentrations at the contact interface. In addition, biomedical applications require low operating voltages, robust fabrication, and small package size, making microelectromechanical systems (MEMS) a natural place to develop novel solutions.

1.1. Total Joint Replacement

Osteoarthritis (OA) is a degenerative, metabolically active disease that affects synovial joints throughout the body, resulting in progressively more extensive and painful joint damage if left untreated. As the most common type of arthritis, OA affects over 45 million Americans, according to the Centers for Disease Control and Prevention [1]. OA is characterized by the loss of hyaline cartilage and joint inflammation, and the surrounding muscles and ligaments are also affected due to physical and biological changes within the joint space and by altered function as a result of biomechanical changes and lower patient activity to manage pain. The complex nature of OA has led to

extensive research to better understand the biochemical, genetic, and biomechanical factors that contribute to the disease.

For end-stage OA, total knee arthroplasty (TKA) is a well-established surgical treatment with high success rates (>90%) with longevity from 8-20 years [2-4]. TKA involves resection of the distal femur and proximal tibial surfaces and placement of metal implants over the ends of the bone as shown in Figure 2.

Usually both femoral condyles are resected, but when only one condyle is degenerated (usually the medial condyle), a uni-condylar joint replacement is used, and all the natural ligatures are preserved. In total joint replacement, an ultra-high molecular weight polyethylene (UHMWPE) bearing surface is inserted between the metal components to provide a low friction, self-lubricating articulating surface.

TKA implant designs vary in geometry and fixation technique. Fixed bearing knee replacements were the first to be used, where the polyethylene component is rigidly fixed to the tibial baseplate. Some implants at this early stage were hinged, but that concept was short-lived. The 1970's witenessed a revolution in implant design establishing today's materials and the basis for many designs still on the market today and many innovators made their mark in this decade, including Insall, Coventry, Ranawat, Burstein, and other. Their work provided the basis for the next few decades of implant design. The addition of mobile bearing polyethylene inserts were introduced in the 1990's, allowing the polyethylene to freely rotate. Implants can also be classified by their treatment of ligamentous structures. In many TKA surgeries, the anterior cruciate

ligament (ACL) is removed. Posterior-cruciate retaining knees preserve the posterior cruciate ligament (PCL) for a passive constraint in the joint; posterior-stabilized knees, require resection of the PCL and its function compensated with a cam-post incorporated in the polyethylene piece. The PCL or the cam-post constrains the knee to mimic the natural knee to allow slipping as the knee is flexed, maintaining a desirable anterior-posterior position of the femoral condyles on the tibial component. Most designs attempt to approximate the kinematics of the natural knee and minimize stresses occurring within the implant during weight-bearing activities. Fixation is achieved using polymethylmethacrylate (PMMA) bone cement to fill the medullary and cortical cavities; a cementless design encourages bone to grow up to or even intertwined with a porous implant face.

The number of TKAs in the United States is on the rise as the population ages and as TKA has become a mainstream surgical intervention (). However, revision of the joint due to implant failure still constitutes about 15% or more of all TKA surgeries. Revision is even more invasive than primary TKA and involves removal of the old implant and additional bone resection to prepare for the second implant. Revision surgeries are more difficult to perform and generally have poorer outcomes compared to primary TKA.

Despite the success of TKA, clinical outcomes are not always ideal, and the rate of revision is increasing faster than the increase in number of primary surgeries (Figure 1). Failure mechanisms depend on proper patient selection, implant design, surgical

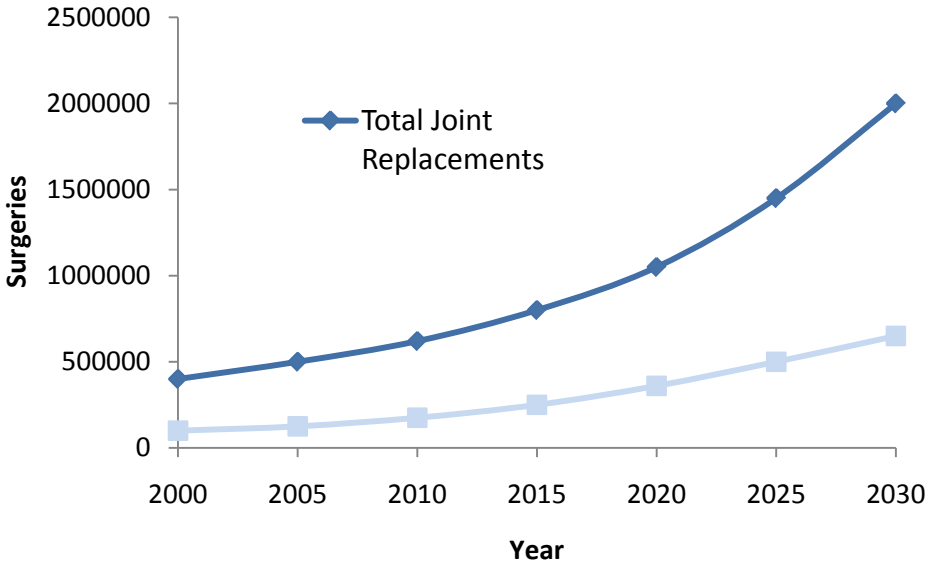

Figure 1. Number of joint replacement surgeries and revisions by year, from the National Institute for Arthritis and Musculoskeletal and Skin Disease (a division of the National Institutes of Health) (reformatted from [5]).

technique, and post-operative rehabilitation and compliance [6]. Short-term failure of primary TKA is due to infection of the joint; however, infection affects less than one percent of all primary TKA cases. Long-term failure due to polyethylene wear is the most common cause for TKA failure because the weight-bearing knee applies stresses to the polyethylene that are at or above the yield strength of the polyethylene (15-21 MPa, depending on UHMWPE formulation and treatment). As a percentage of all revisions, polyethylene wear accounts for 25%, mechanical loosening 24%, instability 20% and infection 17%, with the remaining portion due to lesser causes such as arthrofibrosis, fracture, and other factors [6].

The classification of implant failure is not clear-cut; the majority of patients in a recent study on revision had coexisting contributors [7]. Instability can cause situations of higher stresses which lead to increased abnormal polyethylene wear. Similarly, malalignment can cause abnormal biomechanics and increased stresses within the knee, which also result in increased polyethylene wear. Wear debris can also lodge in the joint space, causing heightened inflammation, aseptic loosening, osteolysis, and accelerating further wear.

Appropriate ligament balancing is a crucial factor in reducing contact stresses and preventing abnormal wear patterns in the polyethylene insert. When one of the collateral ligaments is significantly tighter than the other, the stresses on one side of the polyethylene implant will be higher due to increased compressive forces [8]. However, when the ligaments are too lax, instability in the knee can cause abnormal biomechanics which results in adverse stresses and thus increased wear. The intraoperative balancing of the medial and lateral ligaments is achieved by incremental release at the attachment site of the tight ligament. In the case of extreme laxity of both sides, a thicker polyethylene component is inserted to provide adequate tension for a balanced knee.

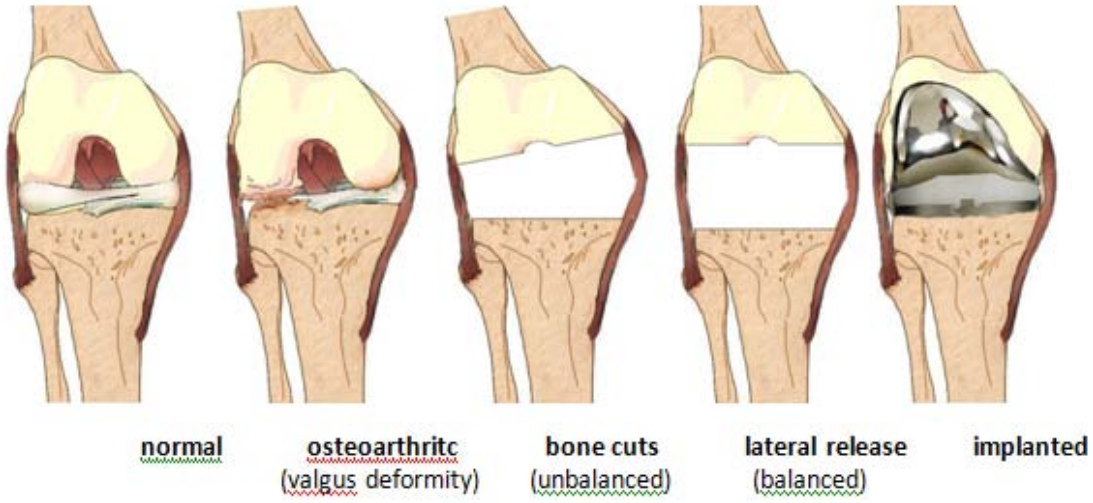

Figure 2. Anterior view of the knee showing normal, osteoarthritic, and implanted knees.

MacIntosh was one of the first to recognize the importance have having the correct instrumentatlion for ligament balancing in TKA [9]. Freeman was the first to introduce the idea of parallel and equal flexion and extension gaps and was the first to use spacers to accomplish proper soft tissue balance. He designed his own ligament balancing instruments in 1974, influencing peers like Insall to also adopt similar ligament balancing methods. Insall first used a tensor device for ligament balancing in 1978 with the Insall-Burstein Posterior-Stabilized knee [10].

1.1.1 Intraoperative Sensing

Incorporating sensors on standard surgical instrumentation during orthopaedic surgery is not a new goal for improving surgical outcomes, but it remains elusive in implementation with sufficient information gathering (sensing) and relevant, timely display to the surgeon. Computer-assisted surgery, or surgical navigation, is becoming

more common in assessing bone resection and measuring implant alignment. Thus position-tracking devices (e.g. infrared passive/active, electromagnetic) comprise the bulk of the system; few, if any, companies have incorporated active sensors (e.g. pressure, temperature, etc.). Thus the alignment may be measured within millimeters but ligament balancing may be far from satisfactory, ultimately leading to premature failure of the prosthesis. Because of the high cost of surgical navigation systems, many are used for research purposes by highly experienced surgeons; the true intention of these systems is to allow precise surgeries for inexperienced surgeons or infrequent cases. The experienced surgeon may not require a navigation system except to complete unusual cases, to assess the quality of his or her skill, or to research new implants or approaches. However, the more inexperienced surgeon may benefit from a navigated approach to ensure proper implant placement, and is also more likely to mis-balance the medial/collateral ligament balancing.

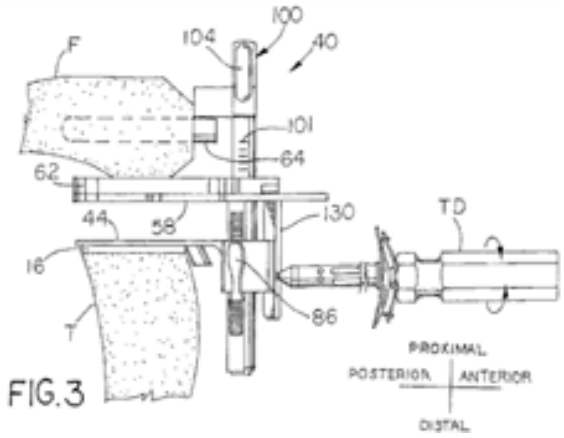

Figure 3. An example of a flexion tensioning device by Booth et al. [11]

Various groups have developed devices to measure ligament balance in the knee during TKA. These devices are usually defined as tension measurement (distraction force measurement) or pressure measurement; tension measurement often has variable distraction distances so that force and distance stretched are measured in pairs. Pressure-sensing devices usually sense at a given height or distraction distance. Tensioning devices were developed first as a way to approximate the actual tension in the ligament, often using springs or screw mechanisms to apply forces to separate bones to stretch the ligaments. An example of this type of tensioner is shown in Figure 3. Tonichi, Inc, of Japan offers a torque gear system which is calibrated to measures distraction forces for soft tissue balancing. Asano, et al. found extension forces were 70.8-182 N and 70.8-169 N for flexion and showed no correlation between ligament tension and amount of post-operative flexion [12]. Using posterior cruciate ligament (PCL) spacers to tension ligaments, Wymenga et al. reported knee flexion gaps to vary between 17.3 and 20.5 mm with 100 N and 200 N tensions, respectively [13]. The tibial forces were measured to infer the ligamental tension (Figure 5). Viskontas, et al. used a tensioning device but noted no significant change in clinical outcome for the tension-balanced patients [14].

Figure 4. A tensioning device for extension (left) and flexion (right) marketed by Zimmer, Inc [15].

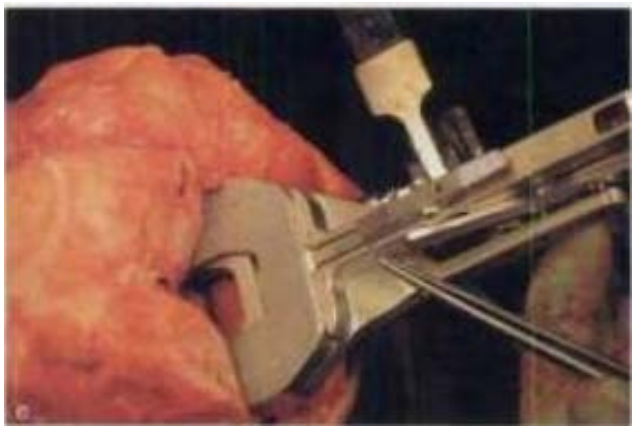

Figure 5. Posterior cruciate ligament tensioning spacer [13].

Designs that focus on pressure or force measurement rather than a net distraction force yield a more complete picture of the loading across the joint; however, inference of the amount of ligament tension is still necessary since no direct tension measurements are made. Moreover, the actual amount of ***tension*** in the ligament is rather unimportant, as the ***pressure distributions*** across the implant contact areas is the true variable the surgeon would like to affect during a balancing procedure with the goal of reducing stress and preventing wear to increase implant longevity. A pressure measurement device may be applied after initial resection but may be most useful if measurements are also taken after initial installation of the femoral and tibial components. The amount of externally applied load, especially by manual manipulation of flexion-extension exercises, could greatly affect the amount of load perceived by the sensor; thus a true passive flexion is ideal (no active muscle loads, no external loads-soft tissue passive constraint only).

Fuji pressure-sensitive films were initially used as a qualitative measurement of contact areas and peak pressures present within the knee (Fujifilm® Prescale Measurement Film). Two thin films encase a layer of microcapsules which rupture under applied pressure and react with a color developer; the stronger the pressure, the more beads ruptured, resulting in a darker areas for higher pressures. The ability to distinguish contact areas and pressure gradients make this the earliest, simplest type of "pressure profile", and the 0.2-0.5 mm thick sheets can easily be used between any two articulating bodies. However, the static nature of the imprint (i.e., a single imprint for an entire range of motion) is a significant drawback, as is the subjectivity of quantifying or calibrating the dark imprints, making comparison between patients and between surgeons difficult. The Fuji films are also temperature and humidity sensitive, and the amount of time a given pressure is held may influence the outcome. Even using low-pressure prescale film, pressures lower than about 2 MPa are not discernable [16]. Takahashi et al. used such a film to examine contact pressure orientation across the tibial trial and aid in ligament balancing, finding improved lateral stability in Fujifilm® assessed patients and no difference in post-operative range of motion with subjects not examined with Fujifilm®.

The simplest pressure sensing device measures a single point on each side of the knee to return net forces acting through those points. Problems with this approach include underestimating the applied force if the force is not located directly above the sensor; there is no ability to locate the maximum pressure or amount of contact

between the femur and the tibia. Wu et al. placed three load cells on each condyle so that the anterior, middle, and posterior thirds could be measured [17]. Suzuki, et al. present a similar design with three 12-mm force transducers per condyle [18]. Wallace used a Tekscan® (South Boston, MA) flexible resistive sensor sheet to measure contact areas and loads during various intraoperative loading conditions, and reported pressures up to 50 MPa for the unbalanced knee, and contact areas consistently less than 0.7 cm^2 [19]. Wasielewski, et al. used Novel® (Munich, Germany) capacitive sensing arrays to measure intra-articular pressure profiles during surgery, reporting forces up to 1.6 MPa (160 N/cm^2) and contact areas up to approximately 4 cm^2 [20]. Optimal, balanced pressures were reported to be less than 0.4 MPa (40 N/ cm^2). Harris compared a high-resolution resistive sensor (K-Scan by Tekscan®) with Fujifilm® Prescale measurement, and noted 11-36% decrease in contact area reported by analysis of the film as opposed to Tekscan digital measurements [21].

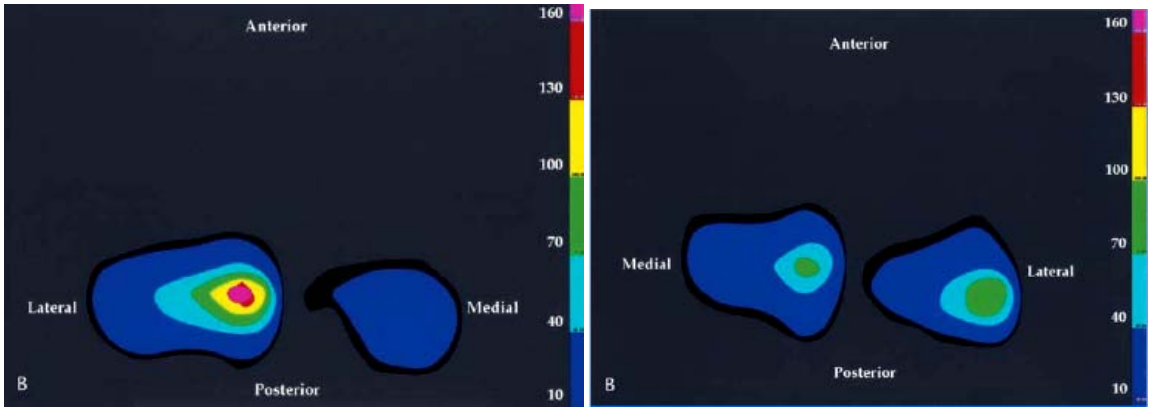

Figure 6. Wasielewski reported unbalanced (left) and balanced (right) pressure maps [20].

As surgical navigation made computers in the operating room more common, researchers turned to technology to aid in ligament balancing. The Synvasive e-LIBRA Dynamic Knee Balancing System™ uses a series provisionals of stepped thicknesses with digital readout, one for the lateral condyle, one for the medial, as shown in Figure 7 [22]. Other companies hint at products being developed, but have been released yet.

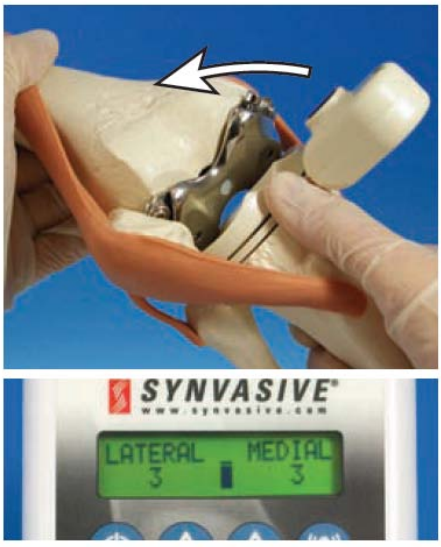

Figure 7. Illustration of the Synvasive E-Libra system [22].

1.1.2 Instrumented Joint Prostheses

It is desirable to directly measure forces across joint replacements in vivo to assess surgical outcomes, implant design, and evaluate patient-specific biomechanics directly. A few research groups have done exploratory studies with instrumented joint prostheses on a small number of patients. Rydell was the first to measure in vivo forces that act within the femoral neck. He measured forces using a disk outfitted with a central strain gauge [23], and in 1966 published results using multiple strain gauges on the femoral head for hemiarthroplasty [24]. Using two different patients, Rydell reported 2.3 and 2.8 times bodyweight for static single leg stance and 2.9 and 3.3 times bodyweight, respectively, for dynamic measurements during gait. The sensors were accessed via wires through the skin. In 1979, English and Kilvington also instrumented a femoral stem for the hip that included telemetric readout, reporting loads of 0.17 times bodyweight supine on the operating table, 0.72 times bodyweight supine in bed one day post-operatively, and 2.56 times bodyweight during gait [25]. Hodge implanted a telemetric hip prosthesis for hemiarthroplasty in 1984 that included 14 load transducers at various positions across the femoral head, as shown in Figure 8. Ten of these sensors were viable at the time of implantation, and data was collected over the course of 3 years, with the sensors articulating directly onto acetabular cartilage [26-27]. In each sensor, a diaphragm deflects due to articular pressures, which is detected by a strain-gauge based system utilizing a silicon-crystal cantilever. Radiofrequency (RF) telemetry was used to transmit the data wirelessly. For passive leg motion shortly after

implantation, Hodge reports pressures around 1.7 MPa. Weight-bearing activities recorded include 5.5 MPa for unassisted walking, and the largest reported pressure, 18 MPa, was found during a standard chair-rise one year post-operatively [27].

Davy and Kotzar also explored in vivo measurement of forces acting across the hip by outfitting the femoral neck of a total hip replacement with three sets of strain gauges to form a triaxial telemetric load cell which was placed at the base of the ball as shown in Figure 8b [28]. Results were reported in terms of axial load and transverse in and out-of-plane loading. Passive loads and unassisted gait were not reported.

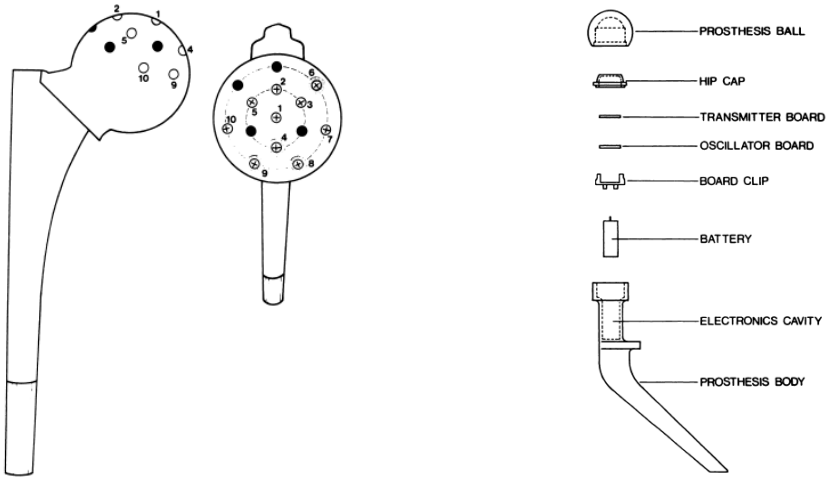

(a) (b)

Figure 8. a.) Instrumented femoral head by Hodge, et al. as reported in 1989. Black dots indicate non-functioning sensors. [27]

b.) Triaxial strain-gauge based telemetric hip implant by Davy as reported in 1988. [28]

No review of orthopaedic telemetric implants would be complete without reference to the seminal work of Bergmann et al., who started work in the early 1990s on telemetric sensing prostheses for joint arthroplasty. Beginning with the hip, strain gauges were used to measure resultant forces transmitted through the hip during various activities. During slow walking, maximum forces were 2.8 and 4.1 times bodyweight, respectively, for two patients [29]. Significantly higher forces were recorded for faster walking and stumbling. Refinements of the strain gauge placement, temperature compensation, and resultant shear force calculation and extensive study of post-operative kinematics has made Bergmann's work a hallmark for in vivo telemetric sensing, both in terms of electronics and its impact on the biomechanics community to substantiate various models of the hip.

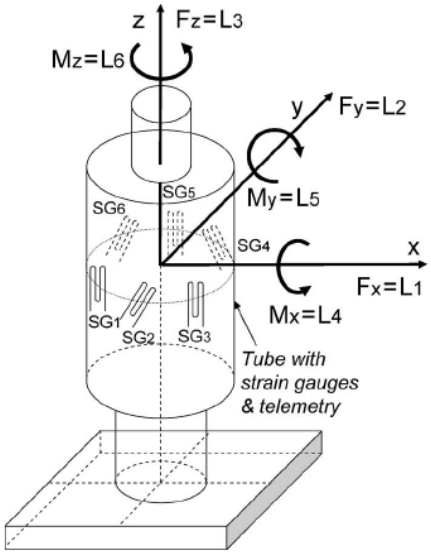

Figure 9. Bergmann's design utilizing 6 strain gauges to measure the three forces and three moments occurring within the tube. The tube is then placed inside various implants for in vivo force monitoring. [30]

Bergmann's work has since expanded to include the knee, utilizing a split-tibial component system incorporating six semiconductor strain gauges in the stem of the tibia, a 9-channel temperature sensing telemetry system, and a sampling rate of 125 Hz [30]. During in vitro mechanical testing at known points, Bergmann reports a load accuracy of 3%. The design was implanted in 2007.

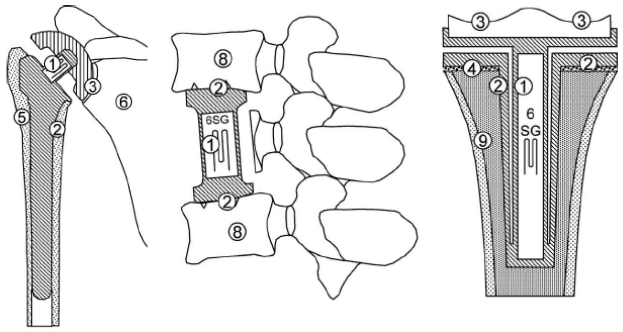

Figure 10. Location of strain gauges (SG), and encasing tube (1) from Bergmann et al. Typically 6 strain gauges are used.

Table 1. Summary of Instrumented Joint Prostheses

Group	Joint	Details	Year
Rydell	hip	wires through skin	1961, 1966
Carlson	hip	telemetric	1971
English and Kilvington	hip	telemetric, battery powered	1979
Barlow	hip	in vitro tests of instrumented implant only	1984*
Davy and Kotzar	hip	telemetric, battery powered	1988
Hodge‡	hip	telemetric, inductively powered	1989
Bergmann et al.	hip	telemetric	1993
Rohlmann et al.	spine	internal fixation implant	1995
Kaufman, et al.	knee	modified implant design, axial forces only 1996, tri-axial 2006	1996*
Bassey et al.	hip	telemetric, inductively powered, axial only, massive femoral	1997
Bergmann et al.	shoulder	telemetric, inductively powered	2001*
Bergmann et al.	knee	telemetric	2005*

* indicates published material on the implant design without in vivo data, which was published later (with the exception of Barlow, et al.)
‡ Hodge continued the earlier work of Carlson.

1.2. Strain Sensing Modalities

1.2.1 Traditional Strain Gauges

The strain gauge is a foundational sensor in mechanical measurements because it couples mechanical and electrical effects to yield the measurement of strain in a particular direction. The change in length of a material when undergoing a given stress is related to the change in electrical resistance of a conducting wire or foil. Lord Kelvin first noted this phenomenon in 1856 when measuring wire resistance under tensile stress. In the 1930's, Edward Simmons and Arthur Ruge used thin metal foil to create conducting traces on insulating sheets, or "carriers". The assembly is then glued to the object to be stressed. Today, the foil lines are placed in a serpentine shape with the longest loops in the direction to be sensed, giving a compact sensor with a higher effective conductor length, which multiplies the change in resistance of the conductor for a given strain compared the change in resistance of a single straight foil line. An example of a typical strain gauge is shown in Figure 11. This enables a highly sensitive measurement of strains when measured with appropriate circuitry. Both tensile and compressive strains can be measured, provided no plastic deformation of the gauge occurs. The concept of the strain gauge has been fine tuned to produce reliable data primarily for measurement of tensile and bending surface stresses. Because a strain gauge only measures strains in a single direction, rosettes with gauges at various angles are often constructed to resolve strains in multiple directions to and enable calculation of stress tensors. However, the design of a conventional strain gauge mounted on a flat surface,

as shown in Figure 11, does not enable measurement of out-of-plane strains; it must be mounted within a rosette such that the strains can be calculated from a system of equations generated by nearby strain sensors. It is also noted that the gauge area limits the ability to resolve the exact location of the strain; rather the measured change in resistance is a result of strains experienced across the active grid length of each loop. When arranged in a rosette, the spatial location between sensors also contributes to this error, albeit a minute error. These individual strains may vary from location to location across the surface of the specimen, but the active grid area is generally assumed to be small enough that the average[1] value suffices.

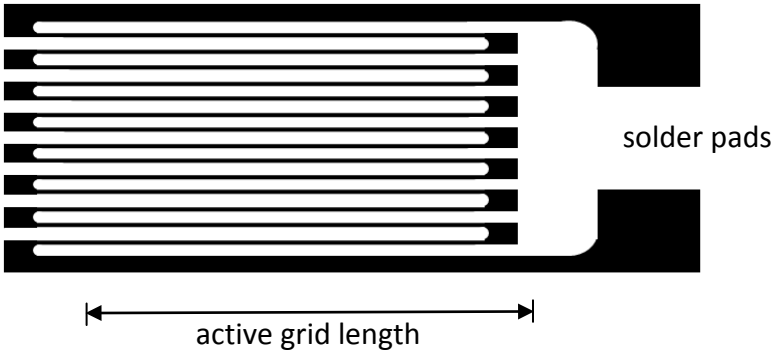

Figure 11. Typical foil strain gauge design.

[1] This is not a true average; the change in resistance of the gauge is influenced by Poisson effects, shear strains, design geometry, and homogeneity of underlying carrier and specimen.

The advent of semiconductor strain gauges enabled shrinking of the overall sensor, and increased sensitivity; the output of the sensor for a given strain is typically up to 50 times more than a typical foil gauge. Semiconductor gauges also perform over a larger range because of this increased sensitivity, and have higher fatigue lifetimes. However, they are more expensive than their foil counterparts.

1.2.2 Flexible Technologies

Flexible circuit technology has been available for interconnects, traces, and component mounting. Standard technology uses polyimide base layers with metal traces, which can be stacked to form multi-layer flex circuits. Polyimide is used for its desirable mechanical, electrical, and chemical and thermal properties, well as its low cost for mass production. Polyimide, trade name Kapton™ (DuPont®), may be used in sheet form, cast onto thin copper sheets, or spun onto silicon wafers as a step in the microfabrication process. Metal is deposited via electroplating or sputtering (with a nickel or chrome seed layer). The cheapest option is to adhere a rolled copper layer to the polyimide and subsequently etch away the unwanted copper. Typically layers are adhered together with acrylic adhesives or epoxy, which introduces an additional thickness which varies depending on manufacturer. Cast polyimide and sputtered copper approaches are both adhesiveless systems, yielding thinner, more flexible circuits. Stiffeners such as FR4 can be added for mechanical durability of connections with standard plugs and jacks. Flex circuits have become commonplace for applications

with space constraints such as laptops, cameras, and phones. Process parameters have been optimized to allow trace widths down to about 50 micrometers.

Flexible sensing modalities specialized to pressure sensing include piezoresistive, piezoelectric, and capacitive approaches [31]. Resistive-based systems are available commercially using semi-conductive pressure-sensitive inks or resistive changes due to percolating networks within polymer-conductor composites. Tekscan® is probably the most popular company using this type of approach [32]. Commercial flexible resistive strain measurement is highly non-linear; therefore careful, frequent calibration may be necessary [33]. Performance may change due to environmental factors such as temperature, humidity, and load history. Classic metal-foil strain gauges have significant spatial resolution limitations; so some researchers have harnessed the accuracy and reliability of a semiconductor strain gauge on flexible substrates. Hwang et al. demonstrate silicon islands embedded in polyimide [34].

Capacitive measurement has also been successful on the market by layering driving lines and sensing lines across a top and bottom layer and placing a dielectric material between them. XSensor® uses a fabric-based approach with conductive threads and foam dielectric [35]. Novel® and Pressure Profile Systems® have also seen success in its capacitive force sensing arrays and offers stretchable arrays, but Novel® is more prevalent in clinical research [36-37]. Capacitive measurement is valued for its high sensitivity and robust performance, but capacitor size constraints may limit spatial resolution. The change in capacitance must be large enough to reliably detect, making

the high precision specialty electronics an essential and often expensive factor. Hierold et al. incorporate a micromachined capacitive sensor into the CMOS process itself [38-39].

Piezoelectric pressure sensors typically yield low spatial resolution and poor temperature stability. However, piezoelectric sensors have been fabricated on flexible substrates by Akiyama and colleagues [40].

The desirable flexibility of polymers also carries inherent drawbacks such as hysteresis and creep; the extent of such influence can be accounted for during calibration. Many polymers have been incorporated into flexible strain sensing arrays as substrates or as dielectrics. The most common material is polyimide; other polymers used include polymethyldisiloxane (PDMS), polyethylene terephthalate (PET), SU-8 resin, parylene, liquid crystals, and various rubbers . Diaphragms are the most familiar capacitive design, but the micromachined silicon sensors have been difficult to effectively incorporate in flexible designs. Diaphragms of compliant materials make it difficult to keep strains within the elastic limit of the material which may reduce the sensor life and performance significantly. Solid construction using thin (nm) metals directly on flexible polymers is promising for contact pressure profiling.

Researchers Rogers and Litt have turned to silk substrates to release metalized circuits and silicon-based transistors for microscale monitoring. When the device is implanted, the silk dissolves to release the microarrays to be conformal to the surface, with applications in cardiac and brain monitoring [41]

1.3. Dissertation Contributions and Structure

1.3.1 Contributions

The goal of this dissertation is to develop conformable real-time capacitive pressure sensor technology suitable for implementation in a surgical ligament balancing tool. The sensors outlined here provide improved spatial resolution as well as improved accuracy and pressure resolution over flexible sensor solutions that are commercially available or presented in the literature today. This presents a valuable tool for quantitative surgical guidance for ligament balancing in total knee arthroplasty, as a stand-alone tool or as part of a surgical navigation suite. The technology presented facilitates static pressure measurement such as a surgical spacer block for flexion and extension and facilitates dynamic pressure measurement throughout the range of motion when implemented on the surface of a provisional component.

Biocompatibility is maintained to leave open the possibility of smart implants in the future. Biocompatible and fabrication processes have been developed to maintain standard biomaterials if the sensors should be migrated to a smart implant platform without degradation of sensor performance. The ultra-high molecular weight polyethylene (UHMWPE) surface characterization presented here has not yet been undertaken by others in the field of research, establishing a basis for future exploration of low-surface energy MEMS devices with micron-level resolution for electrode patterning, especially where ultra-high molecular weights may be desirable.

1.3.2 Outline

Chapter 1 covers a basic background of knee arthroplasty, establishing the clinical need for quantitative intraoperative ligament balancing and discussing current practices and research devices. An introduction to strain sensing and a literature review of current technologies, both rigid and flexible. Chapter 1 ends with an overview of fundamental contributions.

Chapter 2 outlines the design constraints and multiple variables in designing a smart instrument for ligament balancing. A conceptual solution is presented, as well as a theoretical analysis of parallel plate capacitive sensors, their utility in pressure sensing, as well as design considerations and pitfalls of a large capacitive sensing array. A microfabrication scheme is presented for the implementation of the proposed array, and two readout design methodologies are presented for reading of the sensor arrays.

Chapter 3 delves into the intricacies of surface science and examines the surface effects of plasma treatments on polyimides and polyolefins with the goal of improved adhesion of nano or microlayers on top of the bulk polymer. Surface energy and surface roughness are examined and experimental results presented.

Chapter 4 discusses the details of the system design, from prototype implementation to final testing. Starting from the basis of silicon-based capacitive

sensors presented in the literature, flexible capacitive sensing alternatives are sequentially tested for performance to meet specifications outlined in Chapter 2. Smaller test arrays are migrated to a larger, optimized design covering the condylar footprint of a spacer block or surgical provisional with 918 sensors per condyle with a raw spatial resolution of 0.5 mm.

Chapter 5 presents the final discussion and conclusions.

Chapter 6 offers insight into a plethora of other applications, specifically addressing biomechanics ground contact pressures using in-shoe pressure measurements and intracranial pressure monitoring of brain edema for critical care patients. Other scientific endeavors to further the research are also outlined.

Chapter 2. Design and Methodology

2.1. Design Constraints

The sensing array must be optimized for the application pressure range, that is, the pressure range found within an intraoperative patient under anesthesia lying in the supine position. The change in capacitance for a given change in pressure should be optimized to be maximum for the pressure range found within the implanted, passively tensed joint and allow for reasonable pressure variation between patients. For ease of calibration, the sensor response should be directly proportional to the applied axial load. In addition to the pressure resolution discussed above, the spatial resolution should also be addressed. Crosstalk between sensor lines should be minimized, as well as parasitic capacitance and capacitance to ground, to allow the clearest possible transmission of capacitive strain sensing data to enter the readout circuit for digitization. The sensor output levels must be reasonable not to saturate the readout circuitry within the desired pressure range.

Material selection is also critical to sensor performance; design constraints are divided into those for surgical instruments and the more stringent constraints for implanted devices. When intended for implant use, the sensor substrate must be implant-grade material, able to withstand prolonged contact with bodily fluids. All sensor layers should present no bodily harm to the patient if released into the joint capsule in extreme adverse circumstances. The materials should be able to withstand at least one sterilization in the case of an implant, and possibly multiple sterilizations in the

case of a smart instrument. Finally, the mechanical properties of the material must be such that no substantial hysteresis or creep is introduced during the operation of the device. The deformations caused by the material must be fully elastic, meaning no permanent deformation is caused during the use of the device. The short timeframe of the smart instrument use-case scenario places fewer constraints on material selection than the years and decades long scenario for implanted joints.

To quantify the pressure range needed for this design, a variety of biologically occurring pressures were investigated in the literature, as shown in Table 2.

Table 2. Common applications for pressure sensing arrays.

Application	*Pressure*
Vascular pulse (75-150 mmHg)	10 – 20 kPa
Human fingertip texture, shape sensing	10 – 40 kPa
Hand grip	0 – 100 kPa
Fingerprint sensor	1 – 2 kPa
In-shoe pressures	< 1 MPa
Tactile robotics	10 – 100 kPa
Passive knee flexion[2]	
Wasielewski	0 – 1.6 MPa*
Wallace	0 – 50 MPa*
Weight-bearing knee flexion[3]	0 – 32 MPa†

[2] Wasielewski reported contact areas around 4 cm^2 [20] while Wallace reports contact areas around 1 cm^2 [19]. Both used sensing arrays to take intraoperative measurements.

[3] Maximum individual pressure reported by Sharma, et al. from patients with mobile and fixed-bearing total knee replacements [42].

Strain sensing is accomplished by embedding pairs of electrodes with specific geometries in a biocompatible material. Deformation of the embedding materials causes changes in the configuration of the capacitor electrodes. This deformation is sensed as a change in capacitance by the ultra-sensitive readout electronics, as illustrated in Figure 12. The theoretical relationship between strain and change in capacitance is discussed in section 2.2.1.

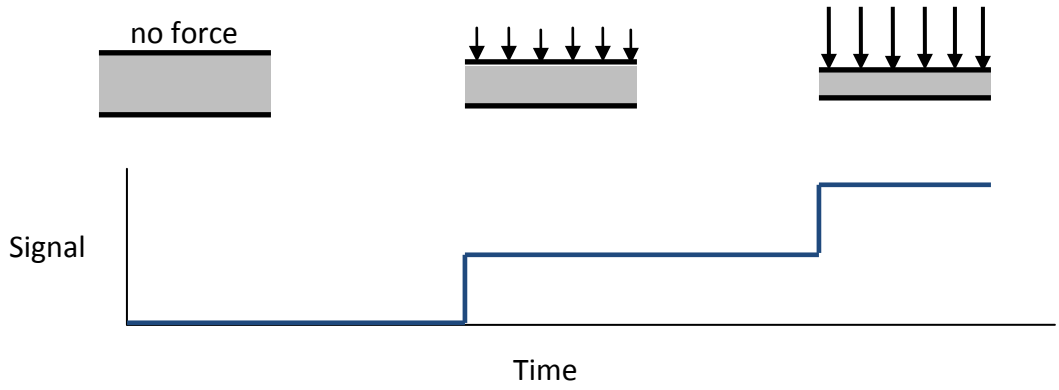

Figure 12. Conceptual illustration of a parallel plate capacitor under incrementally increased loading.

2.2. Concept for Application in Orthopaedic Surgery

The proposed capacitive pressure-sensing arrays can be used at multiple junctures during TKA, depending on which instrument is outfitted with sensors. When mounted on a flat spacer block, the ligament balance after initial bony resection can be measured; the gaps between the distal femur and the proximal tibia (in extension) and the gap between the anterior femur and proximal tibia (in flexion) can be checked for correct resection amount and resection angle. When adhered to a provisional (mimicking the shape of the polyethylene insert), the knee can be checked after final installation of the femoral and tibial components; the height of the polyethylene component can be varied for optimal ligament tension and medial or lateral release as required to optimally balance the knee. The pressure-sensing provisional provides pressure and contact area information for any angle within the range of motion of the knee, allowing the surgeon to detect and correct any abnormal tightness or laxity at any flexion angle.

The output of the pressure sensing array is a two-dimensional colormap so that areas of high and low pressure are easily identified by color, as shown in Figure 13. Numerical values for average pressure and area per condyle are also updated in real time on the screen.

Figure 13. Concept of 2D pressure profile display for intraoperative use. Pressure values and contact areas are updated in real time.

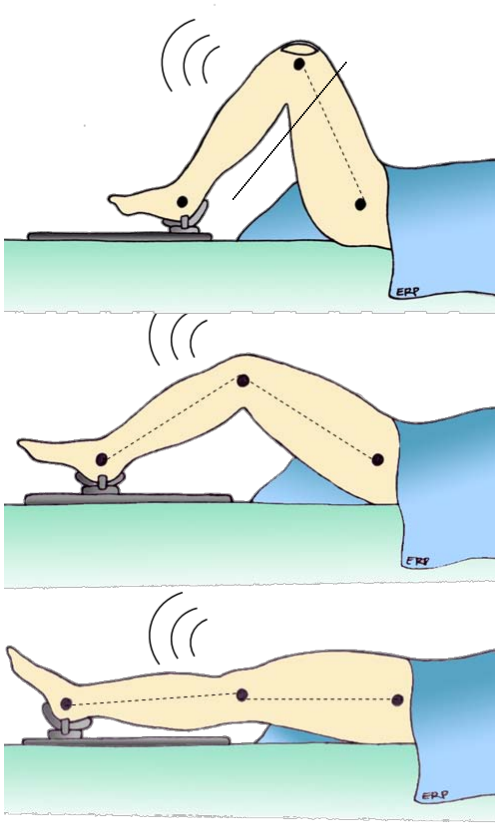

Figure 14. Clinical intraoperative trials utilizing a knee positioner that slides the ankle forward to yield consistent passive flexion of the knee. A surgical navigation system measures the actual flexion obtained.

2.2.1 Electrical Effects of Parallel Plate Capacitors

An understanding of dielectric material properties is necessary to interpret the performance of a capacitive sensor. Metals and other conductors have loosely bound outer electrons or "free electrons" that are available to move about the material, enabling the conduction electrical current (flow of electrons). Electrical conductivity is a measure of the relative mobility of free electrons within the material. Dielectrics are a subset of insulators which do not contain many, if any, free electrons, which inhibits electrical conduction. The term "dielectric" was coined by William Wehwell [42] and describes insulators (non-metals) which can sustain electric fields.

The electric susceptibility of the material, χ_e, measures the ability of a dielectric material to polarize under an electric field and is directly related to the dielectric constant as shown in Equation.

$$\chi_e = \varepsilon_r - 1 \tag{1}$$

The dielectric constant is also called the relative static permittivity. The permittivity of free space, ε_0, is the permittivity of a perfect vacuum in farads per meter and is defined to be

$$\varepsilon_0 \stackrel{\text{def}}{=} \frac{1}{c\mu_0} \approx \frac{1}{2.9979 \cdot 10^8 (4\pi \cdot 10^{-7})} \approx 8.854 \cdot 10^{-12} \tag{2}$$

Where c is the speed of light in meters per second and μ_0 is the permeability of free space in henrys per meter, also known as the magnetic constant [43]. Thus ε_0 has units of farads per meter and ε_r is therefore unitless, as shown in Equation. In some

texts, the dielectric constant is referred to with the symbol κ, and has given rise to the terms “high- κ” and “low- κ” to designate dielectrics at each extreme.

$$\varepsilon_r = \kappa = \frac{\varepsilon_s}{\varepsilon_0} \tag{3}$$

2.2.1.1 Basic Principles

The operation of a parallel plate capacitor and the influence of a dielectric material can be easily understood working from basic principles. A single, infinite charged plate in a vacuum carries a surface charge, σ, and the resulting electric field is constant at a given distance away from the plate, i.e. electric field lines run parallel to the infinite plate (Equation). Points closer to the plate experience a larger electric field, and the magnitude of the field decreases as the observation point is moved farther from the plate.

$$E = 2\pi k\sigma = \frac{\sigma}{2\varepsilon_0} \quad \text{where} \quad \sigma = \frac{Q}{A}. \tag{4}$$

In placing two infinite sheets of equal but opposite charge next to each other, separated by a distance, *d*, the electric fields cancel out, resulting in a net zero electric field.

$$E = -\frac{\sigma}{2\varepsilon_0} + \frac{\sigma}{2\varepsilon_0} = 0 \tag{5}$$

Between the plates, however, the electric field is additive, resulting in a net electric field given by

$$E = \frac{\sigma}{2\varepsilon_0} + \frac{\sigma}{2\varepsilon_0} = \frac{\sigma}{\varepsilon_0}. \tag{6}$$

The electric field is constant between the two oppositely charged plates, forming a capacitor. The electric field is the negative gradient of the voltage,

$$\vec{E} = -\nabla V. \tag{7}$$

If we define a coordinate axes so that the plates lie within x-y planes separated by a distance, *d*, along the z-axis, we can then see that the electric field (a vector quantity), points in the z-direction (neglecting edge effects). Then Equation can be reduced to form Equation . In the case of a parallel plate capacitor, since the electric field is constant (Equation), and the distance between plates, *d*, is fixed, then

$$\vec{E} = -\frac{dV}{dz} = -\frac{V}{d}. \tag{8}$$

The capacitance is related to the voltage by the relation

$$C = \frac{Q}{V} \tag{9}$$

If the plates are then separated by a dielectric medium with a relative dielectric constant, ε_r, then equation becomes

$$E = \frac{\sigma}{\varepsilon_0 \varepsilon_r} = \frac{Q}{\varepsilon_0 \varepsilon_r A}. \tag{10}$$

The introduction of a dielectric medium results in a net reduction of the electric field within the capacitor by a factor of $1/\varepsilon_r$. Combining Equations and , we see that the capacitance is constant regardless of the voltage applied and is related to the plate area, *A*, the plate separation distance, *d*, and the dielectric constant of the material between the plates, as shown in Equation.

$$C = \frac{Q}{Ed} = \frac{Q}{\left(-\frac{Q}{\varepsilon_0 \varepsilon_r A}\right) d} = \frac{\varepsilon_0 \varepsilon_r A}{d}. \tag{11}$$

2.2.1.2 A Classical Approach

In a classical model of dielectrics, each individual atom is represented by a positive point charge surrounded by a negatively charged electron cloud. When an electric field is applied, the negative charge cloud is distorted, creating a dipole between the positive charge and the net position of the negative charge cloud. The dipole moment is a function of the applied electric field. The specific dielectric properties of a given material are influenced by atomic interactions, molecular structure, homogeneity, isotropy, and presence of contaminants.

The polarization of the dielectric material creates an opposing electric field which yields a smaller net electric field within the dielectric without altering the direction. The polarization, $\vec{P}$, is defined between the center of the negative (shifted) electron cloud and the positive center, and can be shown to be frequency dependent in time-varying electric fields.

$$\vec{P} = \varepsilon_0 \chi_e \vec{E} \tag{12}$$

The flux density within the dielectric is a vector field given by

$$\vec{D} = \varepsilon_0 \varepsilon_r \vec{E} \tag{13}$$

Using equations #, #, and #, the flux density is related to the polarization density

$$\vec{D} = \varepsilon_0 \vec{E} + \vec{P} \tag{14}$$

In a simple parallel plate capacitor, two conducting plates are separated by a dielectric material; a voltage is then applied across the capacitor, causing charge to build up. To calculate the flux density, *D*, within a parallel plate capacitor, Gauss' law is applied with Equation #, the total charge, *Q*, is

$$Q = \oint_A \vec{D}\, dA \tag{15}$$

$$\nabla \cdot \vec{E} = \frac{\rho_v}{\varepsilon_0 \varepsilon_r} \tag{16}$$

where ρ_v is the volumetric charge density. The gradient of the voltage gives the electric field, as shown in equation #.

$$\vec{E} = -\nabla V \tag{17}$$

Combining equations # and #, the Poisson equation is obtained:

$$-\nabla \cdot \nabla V = -\nabla^2 V = \frac{\rho_v}{\varepsilon_0 \varepsilon_r} \tag{18}$$

The net volumetric charge density within the dielectric is zero, and the Laplace equation is then formed.

$$\nabla^2 V = 0 \tag{19}$$

For the case of a parallel plate capacitor, a voltage, V_0, is applied to one plate, and the other plate, at some distance *d* from the first plate, carries zero voltage, which allows the formation of Equation 20 from Equation 17, showing that the electric field has constant magnitude between the conductive plates and inversely proportional to their separation distance; electric field direction is also constant and normal to the plate

orientation. In Cartesian coordinates, it is customary to define the plate geometry within the x-y plane, which results in an electric field in the z-direction.

$$E = -\frac{V_0}{d} \tag{20}$$

Combining with Equation 17, an expression for the total charge is obtained:

$$\mathrm{Q} = \varepsilon_0 \varepsilon_r \mathrm{AE} = -\varepsilon_0 \varepsilon_r A \frac{V_0}{d}. \tag{20}$$

Similarly, if the individual charges, *q,* are evenly distributed across each plate of the capacitor and the plate area is significantly larger than the plate separation distance, the electric field, $\vec{E}$, can be written in terms of the charge across the plates

$$E(t) = -\frac{q(t)}{\varepsilon_0 \varepsilon_r A} \tag{21}$$

Combining with Equation 17,

$$-\nabla V = -\frac{q(t)}{\varepsilon_0 \varepsilon_r A} \tag{22}$$

which parallels Equation 10 in the previous section. Capacitance is defined as the ratio of charge carried versus applied voltage:

$$C = \frac{Q}{V}. \tag{23}$$

Rearranging Eq. 20 or Eq. 22 yields the expression for capacitance of a parallel plate,

$$C = \frac{\varepsilon_0 \varepsilon_r A V_0 / d}{V_0} = \frac{\varepsilon_0 \varepsilon_r A}{d}. \tag{24}$$

Practically speaking, a higher dielectric constant causes further reduction of the electric field within the dielectric material, which increases the charge stored and thus increases the capacitance. For a parallel plate capacitor, capacitance is independent of the voltage applied.

2.2.1.3 Capacitance and Stress-Strain Relationships

Changes in stress affect the dielectric material, causing changes in capacitance. The following section describes the relationship between applied stress and corresponding changes in capacitance for a parallel plate capacitor undergoing loading. The nominal capacitance, defined in Eq. 24, corresponds to a capacitor in an unstressed state.

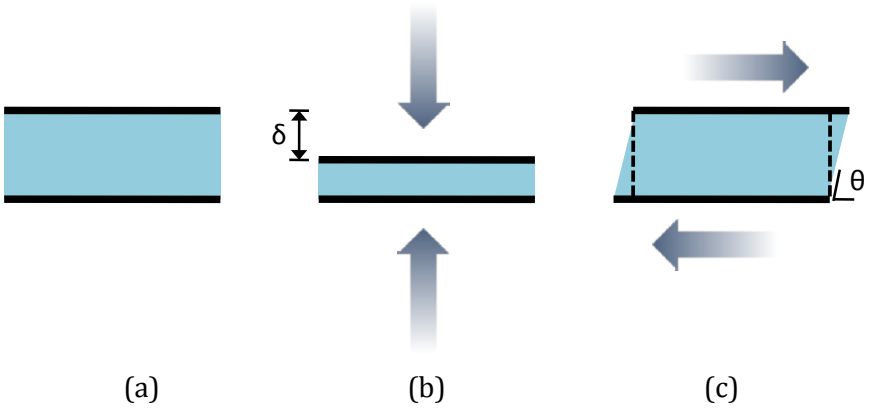

Figure 15. (a) Unstressed capacitor, (b) Applied axial stress and resulting deformation, δ, and (c) deformation θ due to shear stress.

In the case of axial stress, deformation in the axial direction causes the capacitive plates to move closer to one another. Due to Poisson effects, compressive loading also results in slight lengthening of the dielectric in directions perpendicular to loading, which yields a larger electrode area. When undergoing pure shear, the distance between plates remains unchanged except by Poisson effects, and the effective electrode area of the parallel plate configuration is reduced (Figure 15c).

Investigation of these loading effects is best illustrated with a rectangular parallel-plate capacitor, where Eq. 24 defines the theoretical capacitance as

$$C = \frac{\varepsilon_0 \varepsilon_r LW}{D}. \tag{25}$$

Where *L* and *W* are the electrode length and width in the x and y directions respectively, and *D* is the plate separation in the z direction. Upon loading the capacitor in the z-direction, deformation occurs within the dielectric in each of the three Cartesian directions to produce

$$C = \frac{\varepsilon_0 \varepsilon_r (L + \delta_L)(W + \delta_W)}{(D + \delta_D)}. \tag{26}$$

The strain is defined as

$$\varepsilon_x = \frac{\delta_L}{L}, \quad \varepsilon_y = \frac{\delta_W}{W} \quad , and \ \varepsilon_z = \frac{\delta_D}{D}. \tag{27}$$

Eq. 26 is rewritten in terms of strains

$$C = \frac{\varepsilon_0 \varepsilon_r (L(1 + \varepsilon_x))\big(W(1 + \varepsilon_y)\big)}{(D(1 + \varepsilon_z))}. \tag{31}$$

The Poisson ratios coupling the different directions are given by

$$\frac{\nu_{xy}}{E_x} = \frac{\nu_{yx}}{E_y}, \qquad \frac{\nu_{xz}}{E_x} = \frac{\nu_{zx}}{E_z}, \qquad and \qquad \frac{\nu_{yz}}{E_y} = \frac{\nu_{zy}}{E_z}. \tag{28}$$

For axial loading of the parallel plate capacitor, the coupling with the z direction is of primary interest. Only the dielectric is considered for simplicity, but thin film properties and anisotropy make further simplifying assumptions a necessity. A generalized Hooke's law is employed:

$$\varepsilon_x = \frac{1}{E}[\sigma_x - \nu(\sigma_y + \sigma_z)] \tag{33}$$

$$\varepsilon_y = \frac{1}{E}[\sigma_y - \nu(\sigma_x + \sigma_z)] \tag{34}$$

$$\varepsilon_z = \frac{1}{E}[\sigma_z - \nu(\sigma_x + \sigma_y)] \tag{35}$$

With loading only applied in the z direction, Eqns. 33-35 are simplified to

$$\varepsilon_x = \frac{-\nu\sigma_z}{E} \tag{33}$$

$$\varepsilon_y = \frac{-\nu\sigma_z}{E} \tag{34}$$

$$\varepsilon_z = \frac{\sigma_z}{E}, \tag{35}$$

which can be substituted into Eq. 31 to obtain an equation for the capacitance under applied axial loading, as shown in Eq. 36.

$$C_{\sigma_z} = \frac{\varepsilon_0 \varepsilon_r \left(L(1 - \frac{\nu\sigma_z}{E})\right)\left(W(1 - \frac{\nu\sigma_z}{E})\right)}{\left(D(1 + \frac{\sigma_z}{E})\right)}, \tag{36}$$

which simplifies to

$$C = \frac{\varepsilon_0 \varepsilon_r LW}{D} \cdot \frac{\left(1 - \frac{\nu \sigma_z}{E}\right)^2}{\left(1 + \frac{\sigma_z}{E}\right)}. \tag{37}$$

For a parylene dielectric layer with ε_r = 3.1, E = 2.76 GPa, and ν = 0.4, the Poisson effect is negligible, making the term $\left(1 - \frac{\nu \sigma_z}{E}\right)^2 \approx 1$.

This can be generalized to calculate the predicted capacitance under axial strain using any plate geometry of area A within the x-y plane:

$$C = \frac{\varepsilon_0 \varepsilon_r A}{D(1 + \varepsilon_z)}. \tag{39}$$

For a negative (compressive) strain, the capacitance increases. Similarly, the change in capacitance is derived as

$$\Delta C = \frac{\varepsilon_0 \varepsilon_r A}{D \varepsilon_z}. \tag{39}$$

2.3. Sensor Design

Sensor output optimization includes consideration of factors like electrode shape, size, spacing, dielectric thickness, dielectric properties, and material modulus. To judge what electrode size and shape is appropriate, the electrode size (area, A) was plotted against capacitance (Equation 11). Various dielectric thicknesses were plotted to visualize the inversely proportional relationship between capacitance and dielectric thickness.

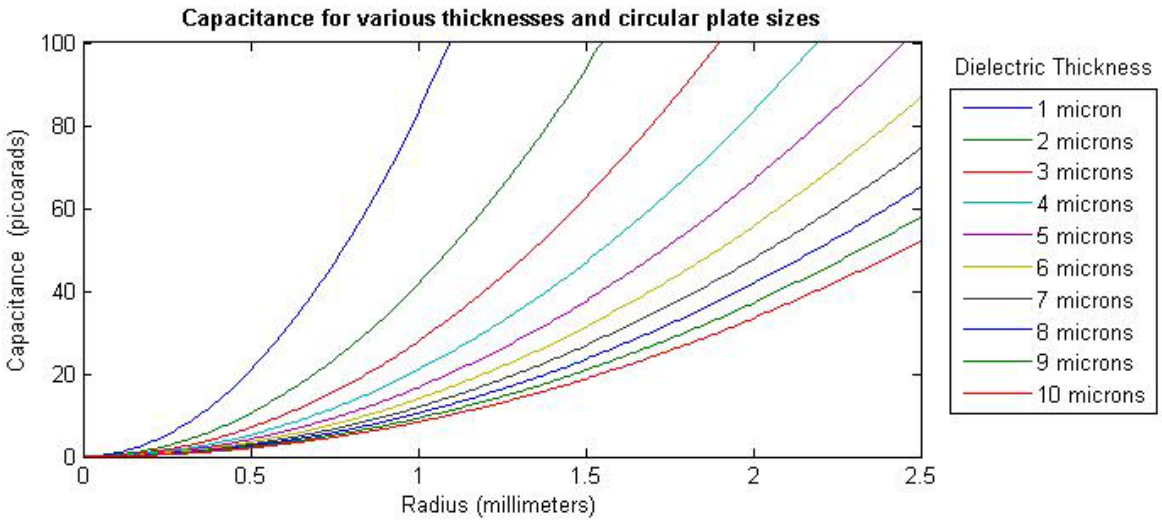

Figure 16. Circular electrode design with varying dielectric thicknesses.

As seen in Figure 16, a circular electrode with a 0.5 mm radius and 1.0 micron thickness results in a nominal capacitance of about 20 picofarads. A thicker dielectric experiences more displacement between the electrodes when a normal force is applied, but thicker dielectrics also cause decreased nominal capacitance. Thus the dielectric thickness must be thin enough to maintain a reasonable nominal capacitance but thick enough and soft enough to yield a measurable change in capacitance when strained.

With a parylene dielectric thickness of 1.5 µm and a desired nominal capacitance of 5 pF, the redius of the required circular electrode is 295 µm. Because the capacitance is inversely proportional to the dielectric thickness, the change in capacitance is expected to be highly non-linear for large deformations, as shown in Figure 17.

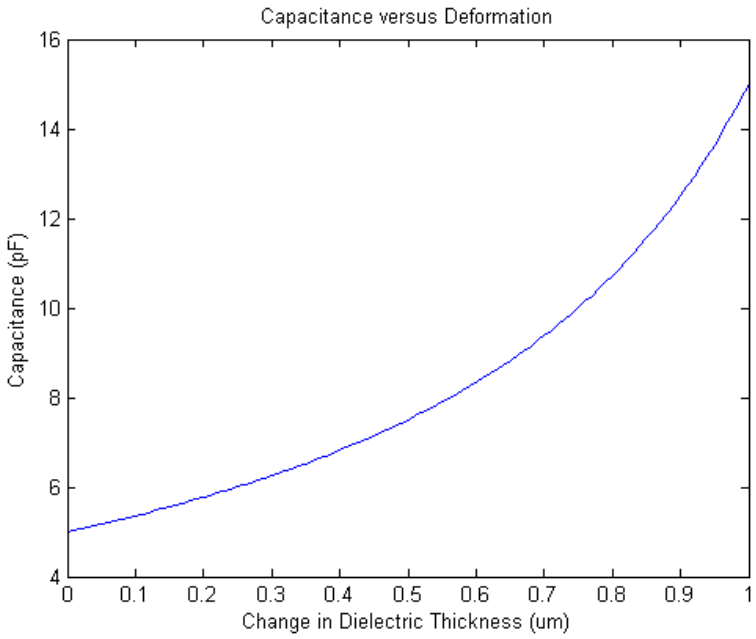

Figure 17. Capacitance change with large dielectric deformation up to 1 µm (ε= 666,666 microstrain).

However, such large deformations are not realistic for most dielectric materials. For the case of a parylene dielectric described above, an applied axial stress of 2 MPa results in a strain of 725 microstrain, which corresponds to a dielectric deformation of 1.09 nm.

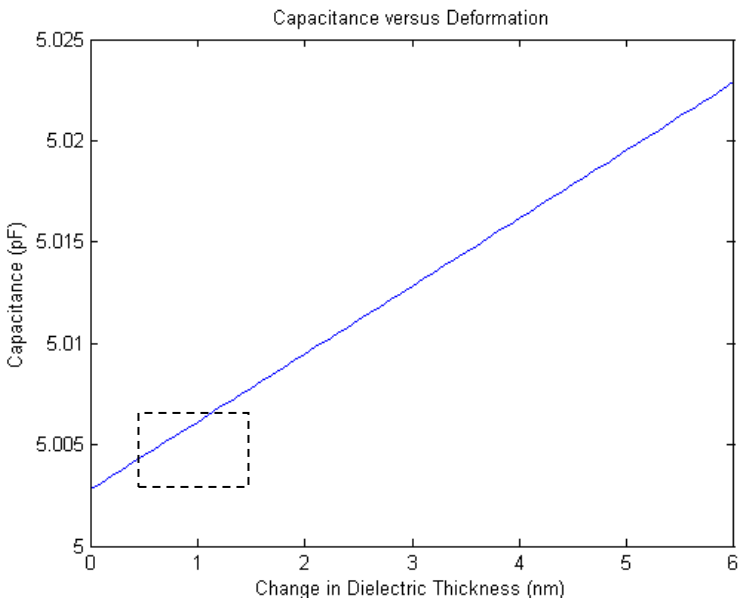

Figure 18. Analytically-predicted change in capacitance for small scale deformation up to 6 nm

(ε= 4,000 microstrain, corresponding to σ=11000 GPa). Dotted line denotes estimated operating range of the sensor.

As Figure 18 shows, when the applied stress is within the MPa or even GPa range, the predicted sensor output is quasi-linear.

The sensor may be considered "solid state", as there are no moving parts (e.g. diaphragms), and the pressure ranges and output capacitance can be controlled by the choice of dielectric medium. Stiffer dielectrics enable higher pressure operating ranges, while softer dielectrics enhance resolution of lower pressure ranges. For a fixed plate dimension, the dielectric constant of the material determines the nominal capacitance and influences the change in capacitance for a given load, making higher dielectric constant materials more desirable.

2.4. Adverse Capacitive Effects

Parasitic capacitance arises from the sensor array design and can sabotage sensitive capacitive readings. This is primarily a concern for added capacitance before it is measured, and thus applies primarily to the sensor, traces, and all circuitry before the signal reaches the capacitance to digital circuitry. Three methods are employed to decrease parasitic capacitance:

1. Array layout design to minimize inter-layer trace crossing and optimize sensor placement
2. Order of sensor excitation, switching delays, and
3. Low excitation frequency.

A portion of the sensor array layout is shown in Figure 19. A sensor is excited for reading by selecting the appropriate row and column, as selected by the multiplexer (MUX). All other MUX connections are grounded. (see appendix on MUX specifications). Potential contributors to parasitic capacitance include sensors along each of the row and column of excitation where the other plate of the sensor is connected to a grounded row or column address. The capacitance to ground or potential for parasitic capacitance (depending on excitation schema) is therefore increased a.) by increasing trace width, b.) by decreasing dielectric layer thickness, c.) by increasing plate area, and d.) increasing array size (where an increase of n numbers of row or column gives an increased parasitic capacitace proportional to n^2) . Simply put, overlapping traces and plates should be minimized and balanced with the need for more sensing nodes.

If sensors are read consecutively, the problem of crosstalk between adjacent rows/columns becomes an issue, forming an unknown contributing capacitor between

the trace lines and top plates of all sensors on the excited lines. When non-consecutive sensors are read, the problem becomes a capacitance to ground issue, where the total allowable capacitance to ground ceiling must be carefully watched. A similar issue arises when using switching delays in the multiplexers to ensure that no two adjacent lines are excited at the same time. A “dead” time is common in many multiplexers, ideally allowing break-before-make delay between sensor line switching. In this case, a 30 nanosecond break-before-make delay is implemented in addition to the 40 nanosecond switching time. This allows a consecutive reading of sensors while minimizing crosstalk. However, leakage currents can also contribute to parasitic capacitance but are difficult to measure in applied circuits. Manufacturer specification for the ADG 706 multiplexer specifies channel to channel crosstalk of -80 dB and is considered negligible.

Adjacent lines form a capacitance to ground that grows as the size of the array grows. The capacitive sensors with one plate grounded are the largest contributor, and actual trace crossings between layers (Figure 19) add an additional capacitance to ground. The capacitance per node on the multiplexer is also a factor, especially in the case when multiple multiplexers are cascaded together to account for an array of increasing size.

The connection between the microarray and the readout circuit board also carries significant potential for added parasitic capacitance and crosstalk. For experimental studies, the sensors were glued to a rigid board for using a conductive

epoxy. If too much epoxy is used, crosstalk may occur between the excited node and the adjacent node. Shielding was used to reduce any extraneous effects from around the connection nodes.

For excitation, lower frequencies are desirable. The AD 7745 capacitance to digital chip uses a 32 kHz excitation; readings with the Agilent LCR meter were set at I MHz.

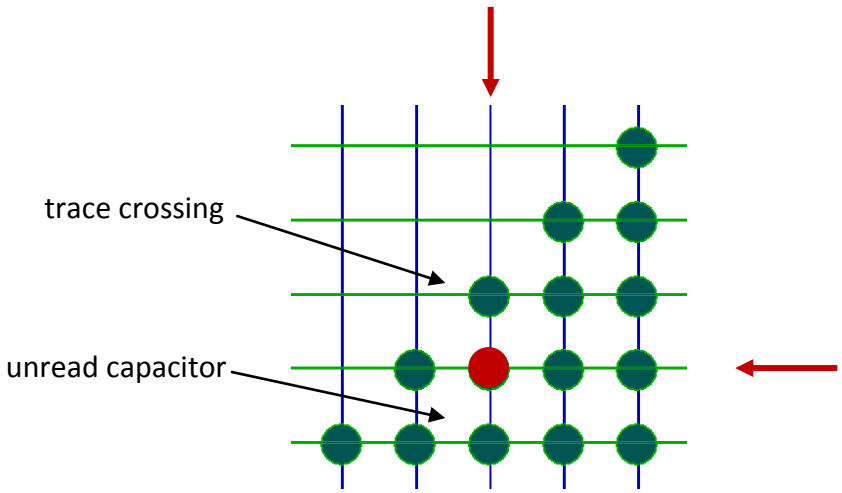

Figure 19. Array design layout demonstrating the addition of parasitic capacitance due to trace crossing and additional sensors in the array. Red represents the sensor being read, all other lines are grounded. All other sensors in the row and column of the selected sensor become capacitors to ground.

Adverse capacitive effects can also happen at the terminals where the flex sensor material meets the readout circuit board. Conductive epoxy was used to permanently mate the pads. As this was a manual process, the amount of epoxy applied was kept to a minimum but varied slightly between connections. Each pad is 0.5 mm apart from the next pad, where pad dimension is 0.5 mm across. Maxwell 11.0 (Ansoft, Boston, MA) was used to simulate the electrical fields surrounding the junction after a conformal parylene coating was applied. In reality, the junction was also covered with adhesive polyimide for protection during experimental handling, resulting in a small air gap between the electrode junctions, where the lower permittivity reduces the capacitive effect between each junction. Figure 20 demonstrates a worst-case scenario where an oversized bead of epoxy spans part of the distance between the pads.

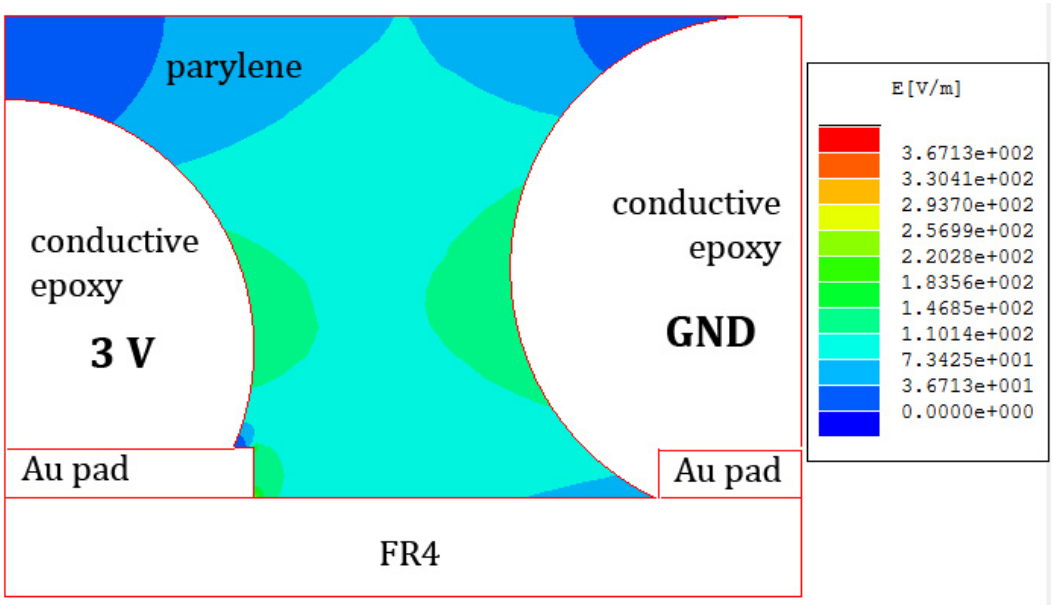

Figure 20. Maxwell simulation of electric fields between PCB and epoxy connections.

2.5. MEMS Fabrication Scheme

First, a robust microfabrication scheme must be established, and then experimental study of performance and fabrication changes for various dielectrics and substrates can be carried out. The processing parameters, material properties, and electrical characteristics are all influenced by the microfabrication process; standard semiconductor processing uses silicon wafers. Once a process has been established, the sensors are made on a variety of substrates, changing process parameters as needed to accommodate the variance in properties from one material to the next. The devices must be inspected for electrical continuity and electrodes inspected for proper adhesion to the substrate. The sensors are then removed from the wafer and mounted on FR4 printed circuit boards (PCBs). Last, the sensors are tested under axial loading conditions to establish their performance and robustness. This experimental flow is iterated until both the design and method are firmly established for the chosen materials and desired performance specifications.

2.5.1 Photolithography

A modified photolithographic fabrication approach is proposed, where a 4-inch silicon wafer is covered with a base film and a number of photolithography, metallization, and liftoff steps are used to create the two electrode layers and the dielectric layer separating the electrodes. Since polyimide is more common in semiconductor fabrication, it is used first to establish the protocols necessary for a polymeric substrate, which can then be customized for other substrate materials. A

photolithography plan is shown in Figure 22 and is used to pattern one layer of the sensing array. The process is repeated for subsequent layers that require electrode patterning (Figure 22).

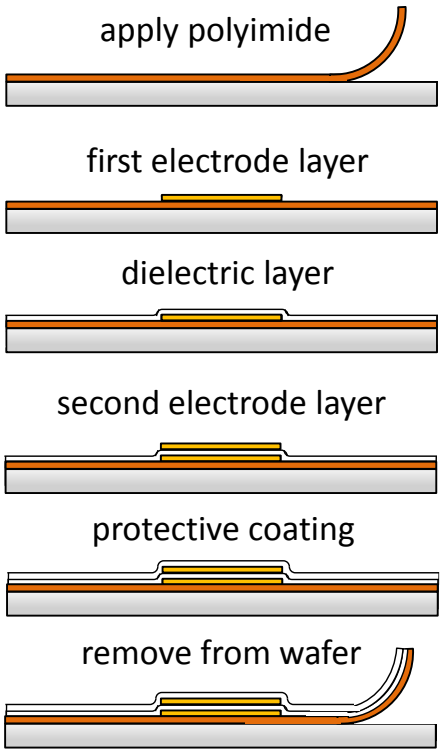

Figure 21. Photolithography method using polyimide as a substrate.

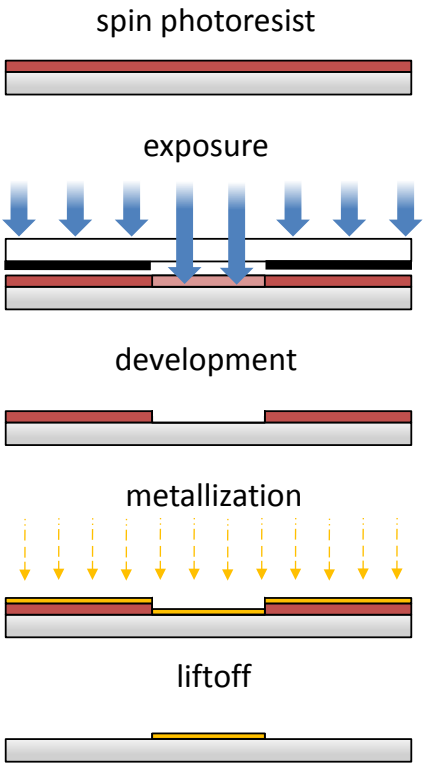

Figure 22. Photolithography process for fabrication of microelectrodes on the material.

2.6. Materials Selection

Selection of appropriate materials is one of the most important factors in ensuring proper function and longevity of the sensing array. The elastic (Young's) modulus and Poisson ratio affect the amount of strain present for a given stress; the amount of strain is related to the change in capacitance. The dielectric and conductive properties of the materials give also directly affect the nominal capacitance of the sensor. However, the practicality of fabrication and the necessity of biocompatibility

impose the primary design constraints. Practicality of fabrication includes the following considerations:

1) Ability to process in conventional machines designed for semiconductor use:
    a) Must not contaminate the machine with byproducts during development, etching, and exposure to ultraviolet radiation.
    b) Must not significantly degrade, lose bulk properties, or become inherently non-biocompatible when exposed to solvents, mild bases (i.e., developer), reactive ion etching, or vacuum conditions.
2) Must be flexible.
3) Must be manufactured to ensure uniform thin film thickness of the material.

For intraoperative use, biocompatibility dictates that the material must not produce an adverse reaction for the given exposure time (i.e. minutes). The material must also not release any harmful debris or substance if damaged during typical use. For implant use, the material must remain inert for an extended period of time (i.e. years), remain functional and intact while withstanding weightbearing loads, and, if cover material is eroded away by wear mechanisms, must not further irritate the joint when the sensor is exposed. In addition, the material must be integrated with existing surgical or implant components while maintaining structural integrity and. This requires compliance matching and shape considerations to decrease or eliminate stress concentrations within the instrument and must also maintain the structural integrity of the device.

Materials that meet basic biocompatibility requirements were selected for initial testing of fabrication. These materials and their reason for initial selection are listed in Table 3.

Table 3. Materials Selected for Initial Investigation

Material	**Reason for Selection**
Ultra-high molecular weight polyethylene (UHMWPE)	FDA-approved. Common material in joint replacement.
Polyimide	Used in standard flexible circuits (via electroplating). Demonstrates basic biocompatibility. [44]
Parylene C	Biocompatible conformal thin film coating.
Polydimethylsiloxane (PDMS)	generally biocompatible in animal studies, flexibility can be varied by adjusting amount of stiffener
Polymethylmethacrylate (PMMA)	Used as photoresist for electron-beam lithography, also used in bulk form in orthopedic implant fixation.
SU-8	biocompatible epoxy-based photoresist

The method of manufacture is the primary factor in final material thickness. Thickness affects the overall flexibility of the sensing array when used as a substrate, and when used as a dielectric, the thickness should be as thin as possible to maximize the nominal capacitance. In addition, for materials that cannot be deposited directly onto the substrate, a layer of adhesive may be necessary to assemble the device, which introduces additional thickness. Medical-grade UHMWPE (Figure 23) is often manufactured by compression molding which substantially limits the ability to make thin specimens, which may also require subsequent annealing to flatten thin samples. Implant components can also be made from machining extruded UHMWPE rods. High and low molecular weight polyethylene may be extruded into sheets or even films, and can be used a tape when an adhesive is applied to one side of a polyethylene film. Polyethylene films are typically low to mid molecular weights designed for non-stick tape applications. Polyimide can also be manufactured in extruded sheet form, and is available in liquid form for spinning directly onto a wafer to obtain thinner layers. The amount of solvent present affects the viscosity of the polyimide and thus dictates thickness when spinning. Care must be taken to properly cure the polyimide to obtain the material properties desired in the final polyimide film. Some formulations of polyimide are photoreactive and can be used in place of photoresist. Parylene C is deposited in a vacuum chamber by a vaporization-pyrolysis-deposition process as shown in Figure 25. Manufactured by Dow Corning as Sylgard Elastomer 184, PDMS is prepared by mixing the base with stiffener, pouring, and subsequent curing. PDMS can also be

spun onto a substrate to obtain thinner layers; additives may be necessary to thin the liquid prior to spinning to obtain thinnest results. The basic chemical composition of PDMS is shown in Figure 27. The length and temperature of curing, presence of additives, and method of mixing all influence whether pinholes are present in the final film. PMMA is commonly used in semiconductor processes as a resist (i.e. for electron beam lithography) or as a sacrificial layer. Both applications utilize spin-on and partial or full curing by baking (Figure 26). PMMA is used in bulk form in orthopaedics as bone cement for implant fixation. Polymerization is rapid and exothermic, requiring mixing in the operating room directly prior to application to the bone.

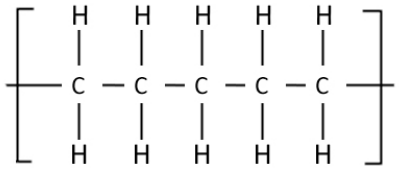

Figure 23. Polyethylene, showing five blocks. Crosslinking can be obtained by crosslinking agents during polymerization or by gamma irradiation.

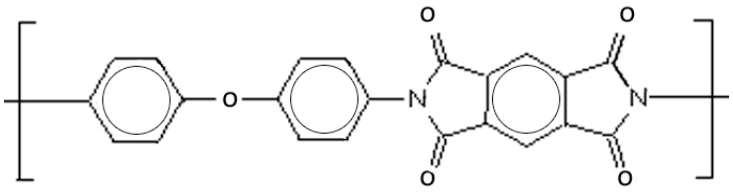

Figure 24. Chemical composition of polyimide (Kapton® Dupont) after curing. Variation may occur between brands and can be changed for intended use (e.g. photosensitivity, etc).

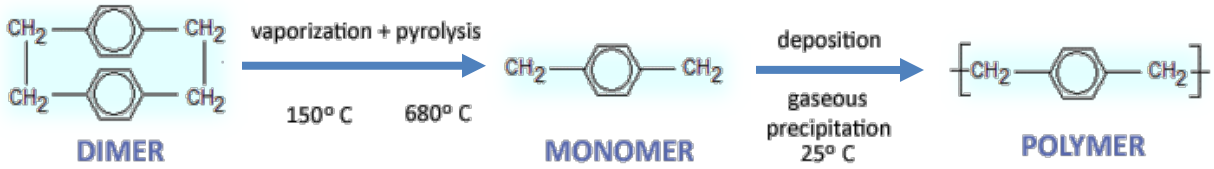

Figure 25. Parylene deposition process.

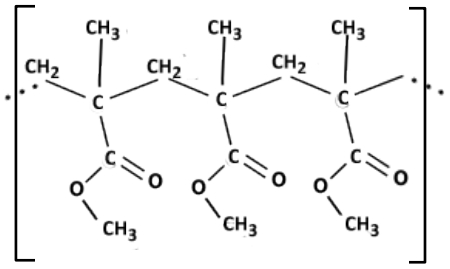

Figure 26. Chemical composition of PMMA, showing a chain of three monomers.

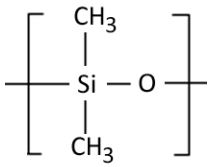

Figure 27. Chemical composition of PDMS.

2.7. Readout Schemes

Two readout schemes are presented in this dissertation. A commercial capacitance to digital chip is implemented with multiplexers and a Bluetooth interface. Two two-layer stacked printed circuit boards are designed to fit within the instrument footprint. Two microcontrollers are used to control the sensor reading and the Bluetooth interface (respectively). More detail on the circuit design and specification is provided in Chapter 4.

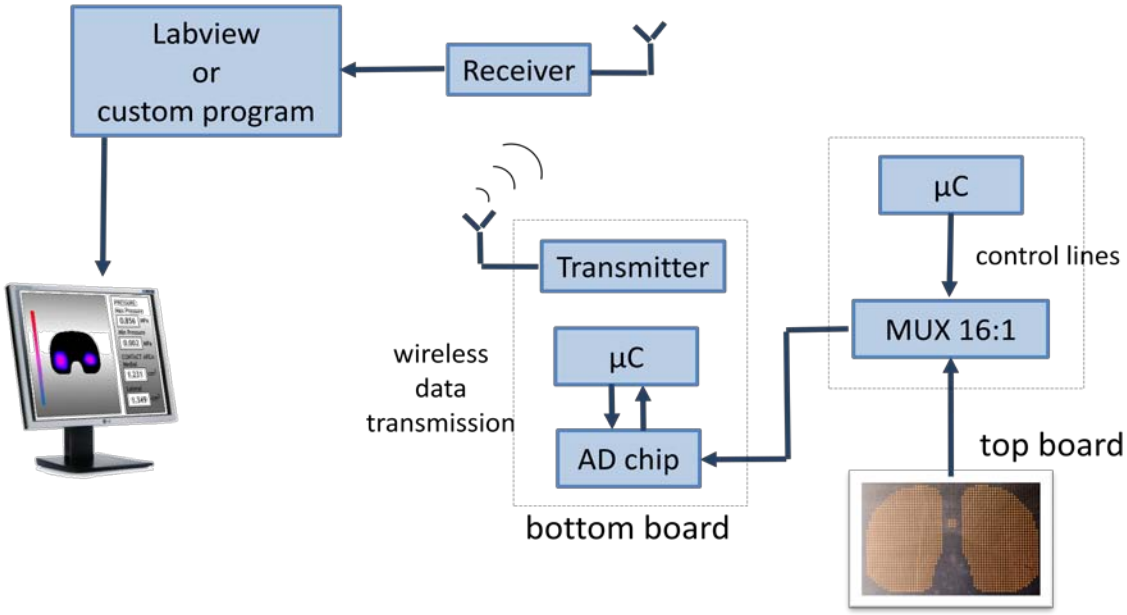

Figure 28. Concept of Bluetooth readout for capacitive ligament balancing instrument.

A custom readout scheme was developed by Haider, et al [45] and implemented in an application specific integrated circuit (ASIC) specifically for the capacitive sensors presented here. High resolution and wide dynamic range sensor signal processing circuit is essential for detection of very low level changes from the sensor and to achieve potential ability to operate with a wide range of sensor variation. High resolution read-out circuit requires precise design and careful layout. Most of the time, track capacitances are in the range of attoFarads (aF, 10^{-18} Farads) or femtoFarads (fF, 10^{-15} Farads) and thus can easily overwhelm the sensor signal and result in poor circuit performance. Leakage current is another problem when designing a circuit using bulk CMOS process. Therefore, proper shielding is required to interface the sensor with the read-out circuit. The circuit is designed to read variable capacitors with nominal capacitance in the picoFarad range (pF, 10^{-9} Farads .

The circuit is designed to measure changes in capacitance from 50 aF to 50 fF with high resolution. The circuit processes the sensor signal into a DC voltage that can be processed by the high capacity analog to digital converter developed under the smart spacer block project. Simulated resolution is 440μV/200aF. Additional capability includes differential capacitive reading for multiaxial sensing being developed for smart implant research.

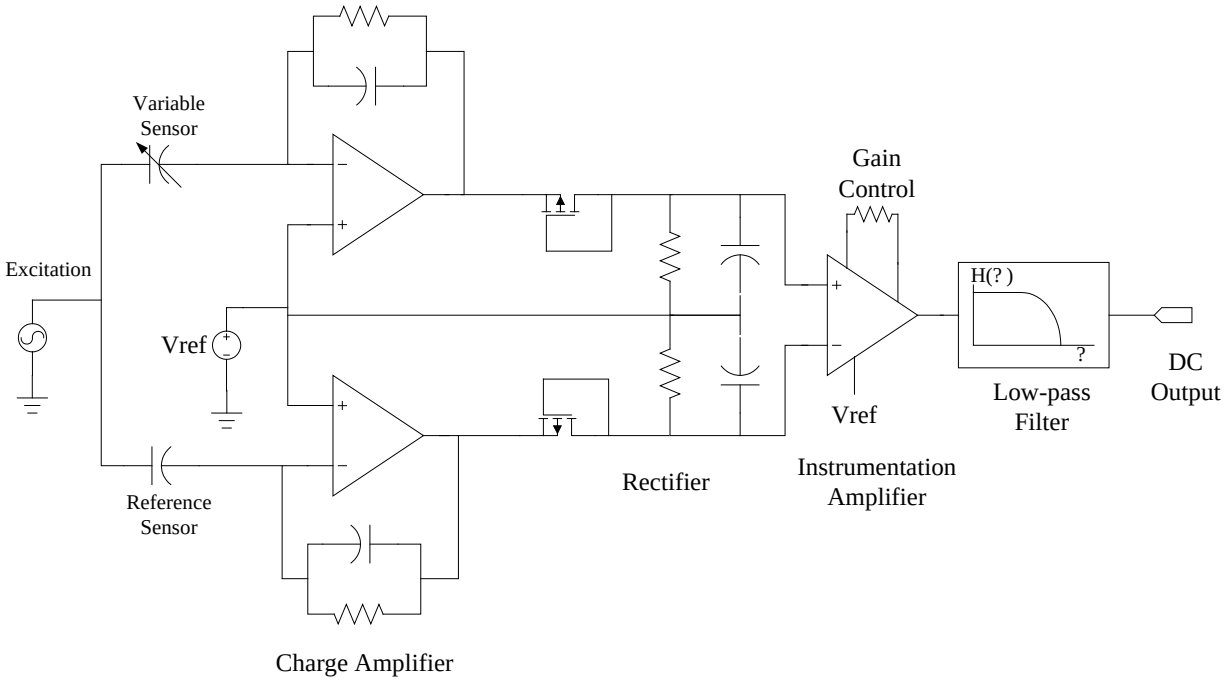

Figure 29. Circuit Diagram for capacitance to voltage converter.

Chapter 3. Surface Modification of Substrates

3.1. Background

MEMS has emerged as a promising new field in the 1990s and has subsequently spread to include many biomedical applications in the last decade. However, the materials and processes used in microfabrication have been generally governed by the needs of the semiconductor industry. The *Williams Dictionary of Biomaterials* defines biocompatibility as "the ability of a material to perform withan appropriate host response in a specific application," and few semiconductor materials can live up to this standard [46]. Functional requirements vary greatly between bioMEMS applications, thus requiring different levels of biocompatibility. ISO 10993 provides minimum testing guidelines, and the United States Food and Drug Administration (FDA) blue book memorandum #G95-1, including animal implantation studies for the specific device materials, configuration, and enough data to demonstrate biocompatibility sufficient for patient safety over the life of the implant. However, many materials currently in use in bulk form with various implantable devices on the market are not compatible with traditional MEMS fabrication processes.

Two scenarios are available for *in vivo* operation of MEMS devices: 1.) use of standard MEMS techniques and implementation of a hermitic seal for biological use or 2.) utilization of biocompatible materials for design fabrication. Examples of hermitic seals include pacemakers' laser-welded titanium cases, glass encapsulation of telemetric antennae [24, 47], and many of these techniques require high temperature levels which

are undesirable for bioMEMS devices. Wafer-level sealing techniques such as eutectic, anodic, and fusion bonding also necessitate the use of traditional semiconductor materials such as silicon, silicon dioxide, and polysilicon.

Deposition of thin polymer coatings have also been used to increase the biocompatibility of silicon-based MEMS devices by shielding non-compatible materials from the bodily environment and reducing corrosion and biofouling. Parylene has also been used to protect MEMs devices that cannot withstand high temperature processes, as its polymerization procedure at room temperature yields a pin-hole free conformal layer. Due to its non-polar nature, parylene shows poor adhesion to non-organic surfaces, although silane-based adhesion promoters are available (e.g. A-174). Parylene C is biocompatible and its method of deposition forms hermitic seals [48]. Parylene is also commonly used for coatings on catheters, pacemakers, and other bio-applications requiring a moisture barrier and reduced corrosion or friction. Other common biocompatible thin polymer coatings include poly ethylene glycol (PEG), poly methyl methacrylate (PMMA), polyvinylidine fluoride (PVDF), and cyanoacrylate (CA), and their co-polymers.

A few researchers have turned to the second option of direct fabrication from biocompatible which allows device electrode contact with the body, which is essential for many bioMEMS applications. In cases where mechanical loading may cause surface wear, surface materials must also show sufficient fatigue strength to determine that undue wear does not occur. The coefficient of friction is a factor in wear consideration,

and all layers must be biocompatible so that any wear debris that may be released is not additionally irritating to the body. In addition, many traditional MEMS materials such as silicon are brittle and unsuitable to undergo loading in the body and may thus cause stress shielding or stress concentrations.

As bioMEMS have been developed for monitoring *in vivo* conditions, existing integrated circuit fabrication materials and processing techniques have been harnessed for bioMEMS purposes. At first, there was little or no substantive evidence of biocompatibility of these materials. First efforts involved testing of materials in for specific applications such as implant coatings , not necessarily MEMs applications. Kotzar et al. performed baseline ISO 10993 biocompatibility and sterilization tests on single crystal silicon (Si), polysilicon, silicon oxide (SiO_2), silicon nitride (Si_3N_4), single crystal cubic silicon carbide (3C-SiC or b-SiC), titanium (Ti), and SU-8 epoxy photoresist [29]. The results are promising, and silicon-based microdevices show decent results in animal testing.

Using well-established biomaterials as a basis for bioMEMS requires the development of new microfabrication techniques and modification of cleanroom processes to accommodate existing biomaterials. This work focuses on MEMS pressure sensor arrays intended for intraoperative use and eventual *in vivo* operation, with the recognition that the fabrication processes here may be applied to other types of bioMEMS devices.

3.2. Plasma Surface Modification

Any of the materials in the previous section can be used as a substrate; the only requirements are a flat, 4-inch disk for processing in semiconductor equipment, flexibility upon device completion, and proper adhesion of electrodes and dielectrics. The low surface energy of polyimide and especially polyethylene may require surface modification to improve adhesion characteristics prior to sensor fabrication on these substrates. A plasma surface activation and nanoroughening is proposed to improve adhesion and raise the overall surface energy. The reactive ion etch (i.e. plasma) bombards the surface with high energy gas, resulting in physical removal of material (roughening) and also undergoing chemical reaction with surface polymer chains, breaking them, or reacting with them to form functionalized groups (Figure 30). It is proposed to test both oxygen and nitrogen low-pressure plasmas' effects on polyethylene to optimize the surface for microfabrication. Plasma gas, flow, power, exposure time, and shelf life are all factors affecting the surface modification.

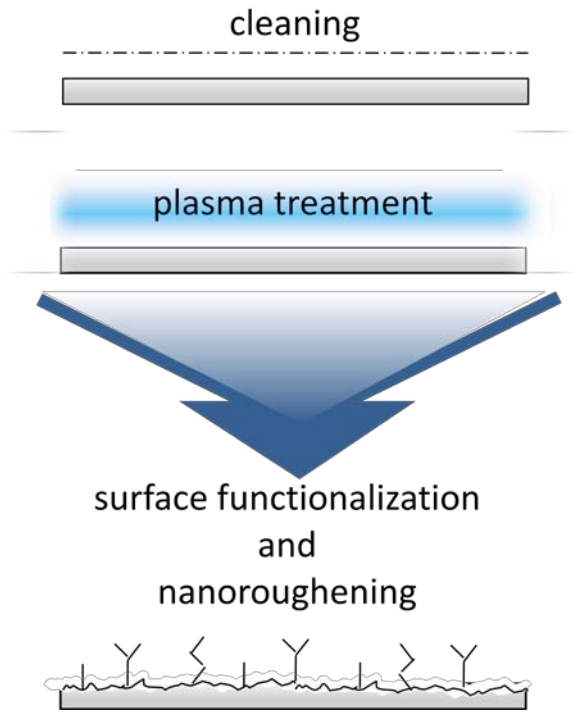

Figure 30. Plasma surface modification scheme.

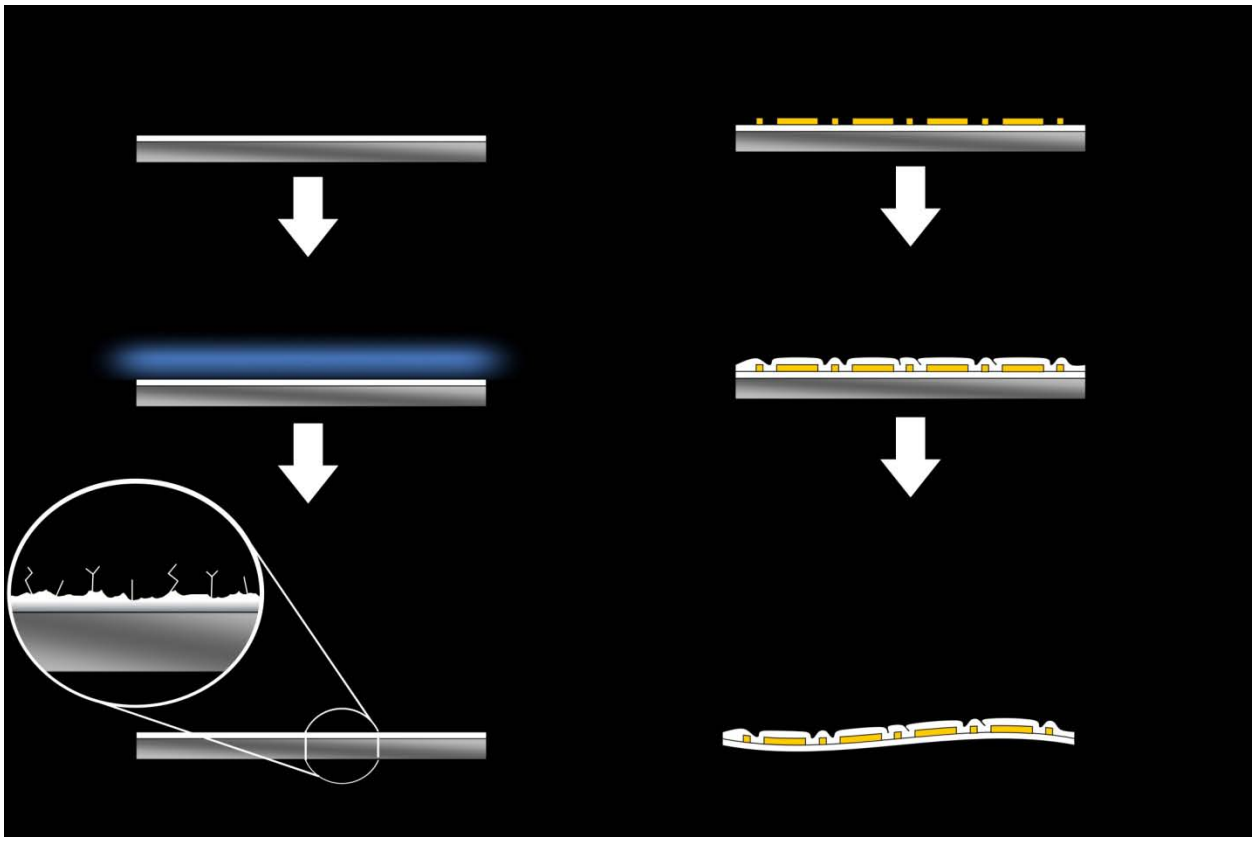

Figure 31. Plasma treatment process where a flexible substrate is adhered to a carrier wafer and then removed after the surface treatments and fabrication.

3.3. Surface Measurements

3.3.1 Surface Energy

A simple measure of surface energy can be obtained via sessile drop contact angle measurement; deionized water is a standard fluid for contact angle measurement. High contact angles represent low surface energies; lower contact angles correspond to higher surface energies. Other fluids can be measured to create enough datapoints to calculate the surface energy of the sample. The half-angle measurement method measures the radius of the drop and the height of the drop to find half the contact

angle. In a typical sessile drop measurement setup, a microdrop is dispensed onto the surface of interest, and the drop is magnified and projected onto a measurement grid for reading. The reading must be taken quickly before the microdrop evaporates; evaporation causes a rapid decrease in contact angle.

Contact angle measurement is an economical and repeatable method of establishing whether or not the plasma treatment has indeed modified the surface of the polymer. Young's equation [49] describes the behavior of the drop:

$$\cos\theta = \frac{\gamma_{\text{solid}} - \gamma_{\text{interface}}}{\gamma_{\text{liquid}}}. \tag{22}$$

Similarly, the work of adhesion is described as

$$W_{adhesion} = \gamma_{liquid}\,(1 + cos\theta) = \gamma_{substrate} + \gamma_{film} - \gamma_{interface}\,. \tag{23}$$

The surface tension of deionized water is 72.9 mJ/m^2 [50], which allows the estimation of changes of surface energy via contact angle measurement and thus track changes in adhesion characteristics. The work necessary for adhesion is given by Eq. 7. The known surface energy of gold is then used in calculation of an approximate value for the interfacial energy between the gold and the polyethylene using Eq. 8. The surface energy of the polyethylene is calculated using the Girifalco–Good–Fowkes–Young (GGFY) method

$$\gamma_l(1 + \cos(\theta)) = 2\sqrt{\gamma_l\gamma_s} - \pi \tag{24}$$

where the vapor pressure, π, is assumed to be negligible.

3.3.2 Surface Roughness Measurement

The surface roughness before and after plasma treatment can be characterized by contact profilometry, atomic force microscopy, and non-contact profilometry (optical). Profilometric measurements are convenient, fast, and offer a longer scan range; the longer scan ranges allow a better view of surface features on the order of millimeters or fractions of a millimeter. For contact profilometry, a stylus is lowered until it touches the surface to be examined. It is then gently moved across the surface as the stylus tip height is measured to provide a one-line measurement of the surface profile.

Atomic force microscopy works via a similar mechanism, where a microcantilever with a nanoscale tip is lowered onto the surface to be measured. Modes include non-contact and tapping; tapping is the primary mode used in this dissertation. The cantilever is driven to oscillate back and forth, tapping the surface as it is moved in a line across the surface. Van der Waals interaction forces with the surface create damping as the cantilever approaches (cantilever oscillation is on the order of tens or a couple hundreds of nanometers). The cantilever is scanned back and forth so that the multiple scan lines create a 3D mapping of the surface features. Thus AFM images can be viewed in 3D, or as line plots of single scan lines (Figure 32). Parameters must be carefully selected for the surface type to be imaged and be well controlled to produce accurate results without scan artifacts.

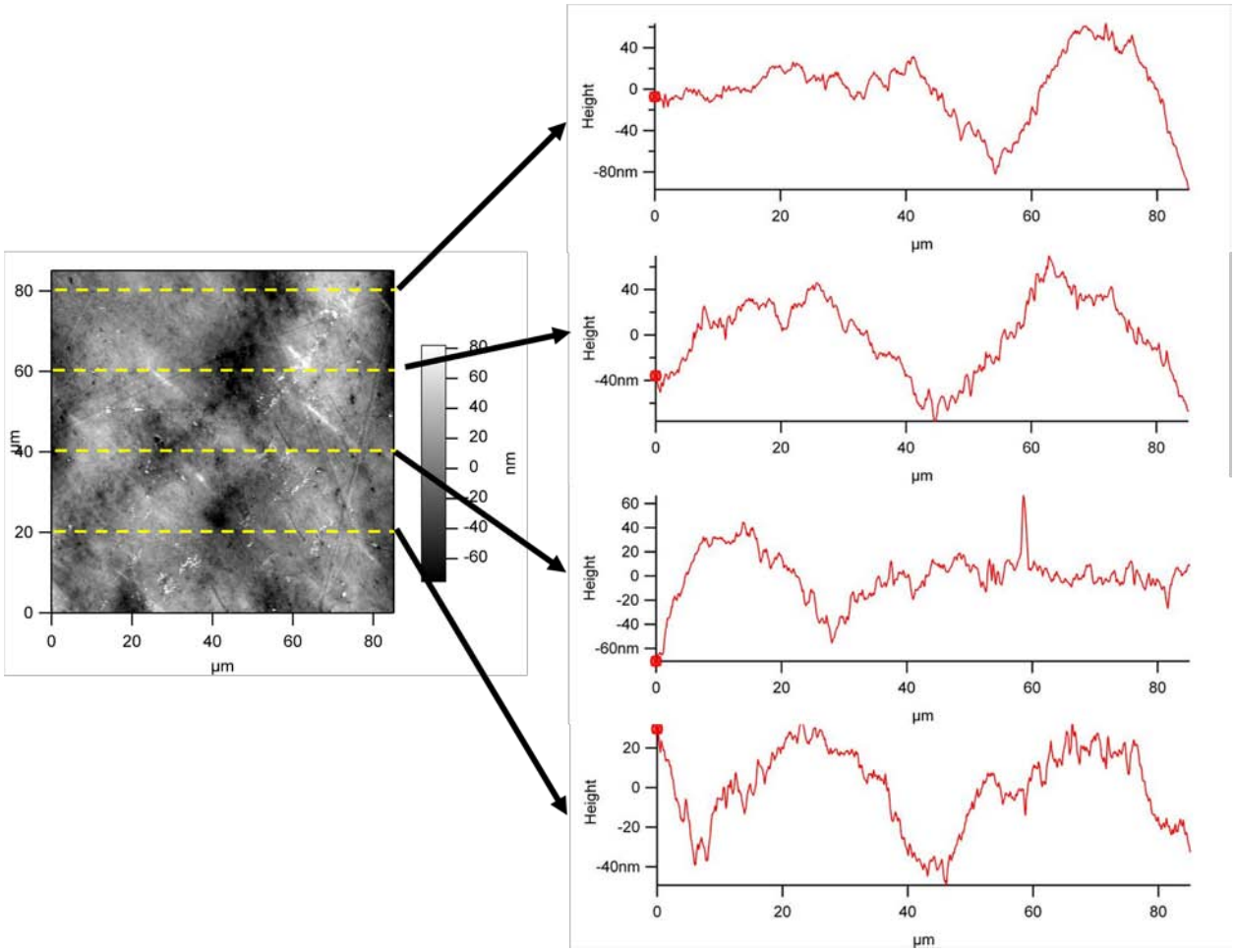

Figure 32. AFM scan of Zimmer UHMWPE compression molded disk, showing various profiles within the scan.

3.3.3 Surface Functionalization Measurement

To measure the amount and type of surface functionalization, the surface should be measured immediately after treatment. Ideally measurement occurs in a vacuum environment before the sample is exposed to air to reduce oxidation and degradation of functional groups. X-ray photoelectron spectroscopy (XPS) can identify the composition of surface elements within the top 1-10 nm and their chemical states, while also giving an idea of the distribution of those elements when multiple scans are combined. Secondary Ion Mass Spectrometry (static or dynamic) is also capable of measuring surface elements on the sample; a focused ion beam is directed at the surface while ejected surface atoms are measured. Static SIMS may only damage the top few angstroms of the sample, but dynamic SIMS may damage deeper levels (i.e. microns). However, both XPS and SIMS systems are expensive and access is often limited.

3.3.4 Polyethylene Surface Modification

Low pressure glow discharge plasmas have been used for surface treatments of polymers in the past to improve adhesion characteristics. Multiple mechanisms are at work during a plasma treatment that can help adhesion characteristics, which is also correlated with increased surface energy. Plasma surface modification enhances the surface by multiple mechanisms. It removes organic residues, introduces new functional groups such as C=O, C-O, ethers, and esters. Chain scission and increased crosslinking

further modify the material properties within the surface layer. As a common polyolefin, polyethylene was an early candidate for plasma surface modification research.

Existing research has shown successful surface modification of low density polyethylene (LDPE) and high density polyethylene (HDPE), which have densities of 0.91-0.94 g/cm^3 and 0.94-0.97 g/cm^3 respectively. Less data is present in the literature to compare these effects to those observed with plasma modification of ultra-high molecular weight polyethylene. The extremely long chains of UHMWPE give it desirable bulk properties for biomedical applications, particularly in orthopaedics.

Corona discharge and atmospheric plasma can be used for similar outcomes with reduced cost of manufacturing. Mangipudi at al. showed an increase in polyethylene surface energy from 33 mJ/m^2 to 55 mJ/m^2 with corona discharge treatment at room temperature and atmospheric pressure [51]. O'Kell et al. demonstrated an increase in surface energy from 37 mJ/m^2 to 47 mJ/m^2 and 46 mJ/m^2, respectively, with low-power air and nitrogen plasma treatments [52].

3.3.4.1 Substrate Preparation and Measurement

Surface treatments can be used to increase adhesion of gold onto low surface energy substrates such as polyethylene. When deposited on a substrate via physical vapor deposition (evaporation), a gold film's crystalline structure is oriented with the (111) plane facing upward from the film surface. The Au has a free surface energy of approximately 45 mJ/m^2. In comparison, polyethylene has a surface energy of 30-40

mJ/m^2. This low surface energy contributes to inherent hydrophobicity and poor adhesion characteristics [50, 53].

Contact angle measurement is used as an estimate of surface energy modification of the polyethylene surface as a result of plasma exposure. Microroughening effects are examined using optical microscopy for qualitative comparison of large features between treatment groups and atomic force microscopy is used to quantitatively examine the surfaces at the micro-scale.

3.3.5 Surface Characterization Results

An initial study was conducted using 4 inch diameter 1 mm thick high density polyethylene (HDPE, Piedmont Plastics, Knoxville, TN) extruded sheet and 4.5 millimeter thick compression-molded ultra-high molecular weight polyethylene (UHMWPE) Zimmer, Inc (Warsaw, IN) [54]. Successful microfabrication of single-layer gold patterns were demonstrated on the HDPE sheet, but gold adhesion on UHMWPE was not achieved. This was primarily attributed to the surface roughness characteristics of the compression-molded samples, which were produced without an optimized molding process. In addition, significant surface scratches were noted on the UHMWPE substrates, which inhibited continuous metal traces across the surface and may have also contributed to peeling of the metal due these discontinuities.

Next, 3-inch discs were compression-molded using a custom-polished mold and improved processing parameters. Two powder formulations were used for these compression-molded disks. GUR 1050 resin (Ticona, Oberhausen, Germany) and 1900

resin (Basell Polyolefins, Wilmington, DE). Ten compression-molded disks were made at Zimmer with 1050 resin, and 10 disks with 1900 resin. (Note: The 1900 resin was discontinued from production by Basell in January 2002, and the remaining limited supply continued to be used by two implant manufacturers for certain orthopaedic implants [55].) Disk thickness was less than 2 millimeters. The third type of UHMWPE tested was a film (75 micrometers thick, obtained from CS Hyde, Lake Villa, Illinois) which was manually cut and adhered via acrylic adhesive to the top side of a 4-inch silicon wafer for processing.

Surface roughness and morphology were measured using atomic force microscopy (Pacific Nanotechnology Nano-R system). Linear image correction followed by second-order correction for piezoelectric scanner "background bow" were implemented after image acquisition. Compression-molded samples were found to have an undulating pattern (Figure 33) from powder agglomeration during compression as well as microscratches from the mold. Both aspects of the surface finish can be improved through tweaking process parameters such as amount of powder, pressure, temperature, piston speed, and cycle time. While these are carefully set for implant materials, the time and care taken to optimize these may improve surface finish. Improved mold finish (i.e. optical grade smoothness) will also minimize microscratches present on the surface of the finished product.

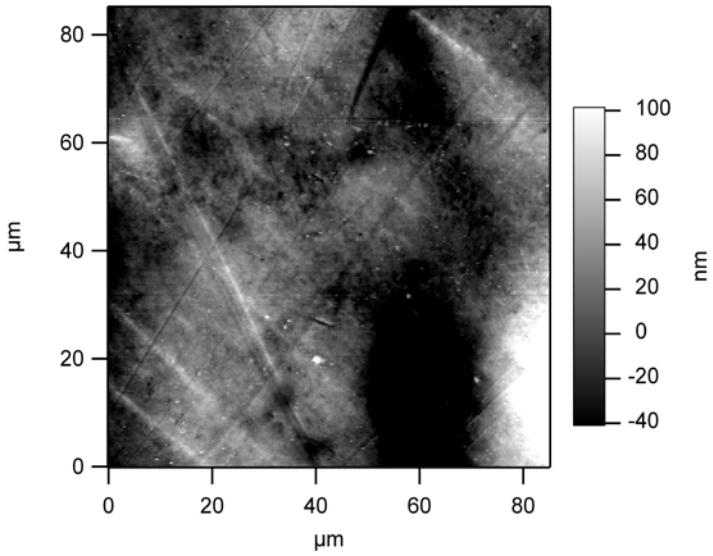

Figure 33. Representative compression-molded UHMWPE prior to treatment, showing micro scratches from the mold and undulating features from the agglomeration of resin powder.

No significant differences between oxygen-only and nitrogen-only were found in AFM analysis, as demonstrated in Figure 34 and Figure 35. However, qualitative analysis via optical microscopy revealed morphologic changes in all treatment groups, especially the oxygen/nitrogen combination treatment group (Figure 36) having smaller feature sizes.

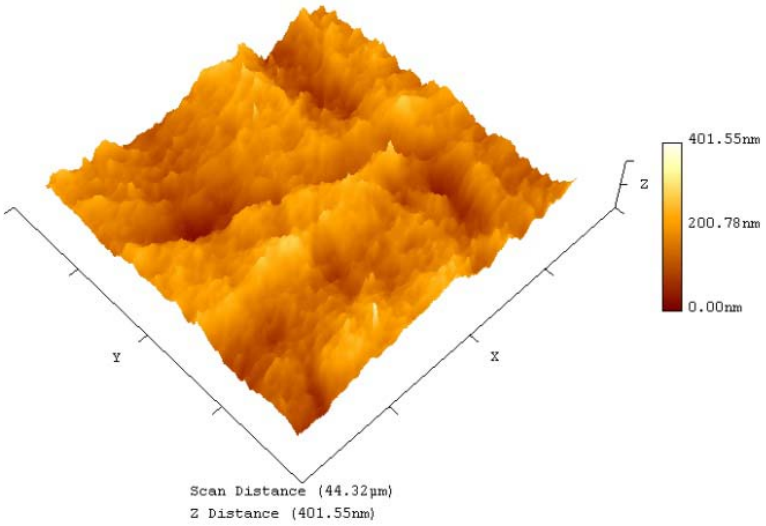

Figure 34. AFM image of an oxygen-treated sample. Scan size is 45 x 45 um. RMS roughness is 35.4 nm.

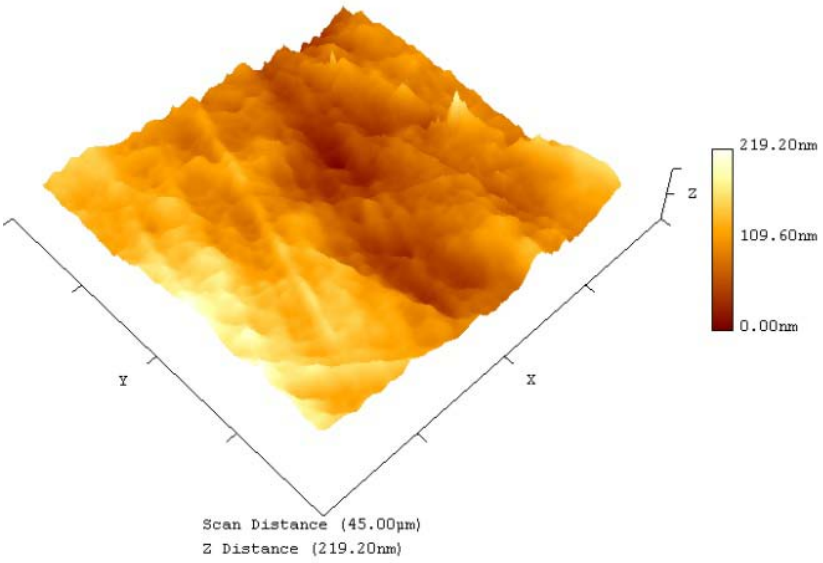

Figure 35. Nitrogen-treated sample. Scan size is 45 x 45 um. RMS roughness is 41.4 nm.

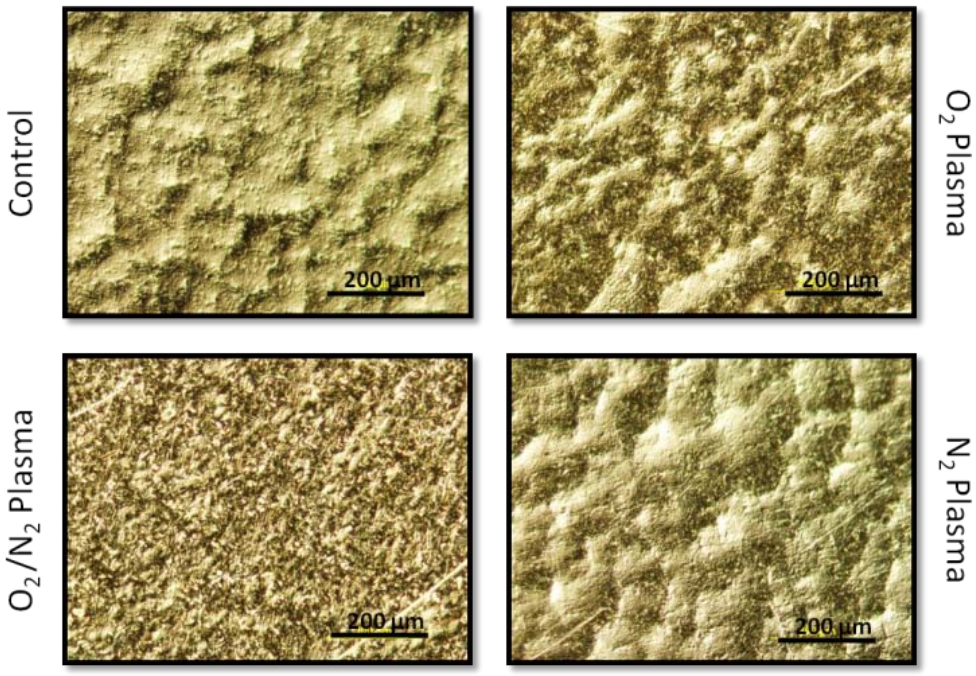

Figure 36. Micrographs of UHMWPE samples after treatment (5x magnification). A gold layer was evaporated onto the surface for enhanced visualization of surface features (no photolithography). Roughening effect of oxygen/nitrogen plasma treatment is evident.

Surface modification of commercial UHMWPE was experimentally investigated by sessile drop contact angle measurement with deionized water using a Tantec CAM-Plus contact angle meter (ChemInstruments, Fairfield, OH). A programmable syringe pump (New Era Pump Systems, Wantagh, NY) was used to dispense metered deionized water droplets on the surface for measurerment via a 150 µm diameter tube . A half-angle method was employed where the height and diameter of the drop are measured and the resulting angle is then calculated, not directly read. This improves both the manual measurement accuracy and precision. Ten measurements were taken at varying

locations across the diameter of each sample for 20-40 measurements per treatment group.

Figure 37. Sessile drop measurement setup.

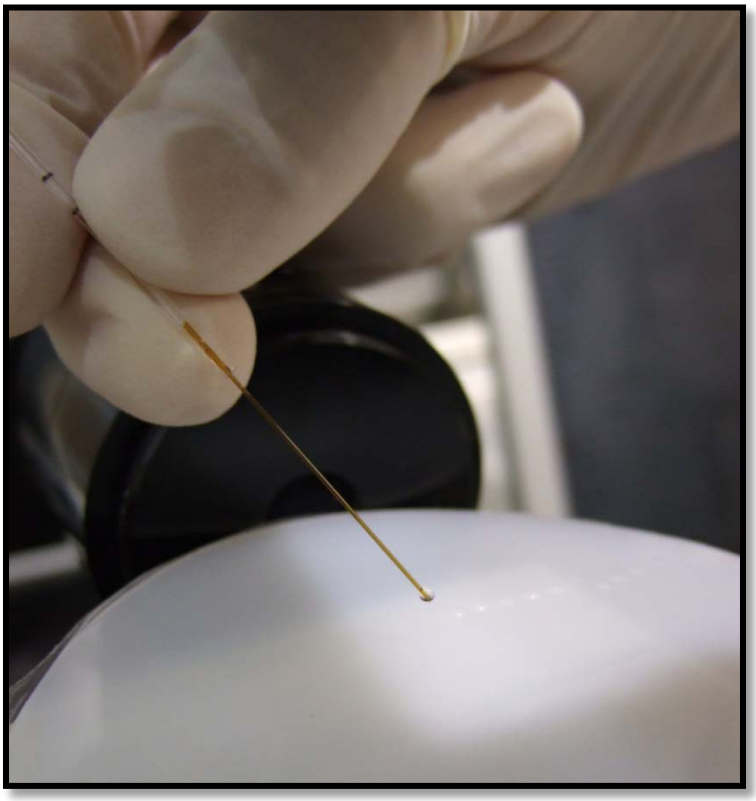

Figure 38. Experimental setup showing microtip on the pipette and the droplet formed on the end. Also note the line of droplets showing how the 10 measurements were taking across each sample to account for any spatial variations.

All samples, including controls, were cleaned. A 2% liquinox solution was used with light rubbing to remove any particulates or residue on the substrate, followed by a rinse in deionized water. The samples were subsequently rinsed in succession with acetone, methanol, and finally, isopropyl alcohol. The substrates were then blown dry with clean dry air.

Plasma treatment groups were divided into oxygen, nitrogen, and simultaneous oxygen/nitrogen. A Trion Technologies (Clearwater, FL) Oracle Reactive Ion Etcher was used for plasma treatment. For oxygen, 50 standard cubic centimeters (sccm) of O_2 was ignited at 100 W for 30 seconds at low pressure (12-15 mTorr). Similarly, the nitrogen treatment group underwent N_2 plasma at 50 sccm and 100 W power for 30 seconds. For the combined O_2/N_2 treatment group, 50 sccm O_2 and 5 sccm N_2 were used together at 100 W for 30 seconds. Samples were bagged individually for storage at room temperature and atmospheric pressure.

As expected, the plasma treatment of the substrates also aided in adhesion of the parylene dielectric layer, which typically exhibits poor adhesion unless a coupling agent is introduced. In addition, an unexpected phenomenon was observed after the parylene dielectric deposition. Polyethylene is more permeable to oxygen than nitrogen by a factor of 4 for HDPE and approximately a factor of 3 for LDPE ([53]).

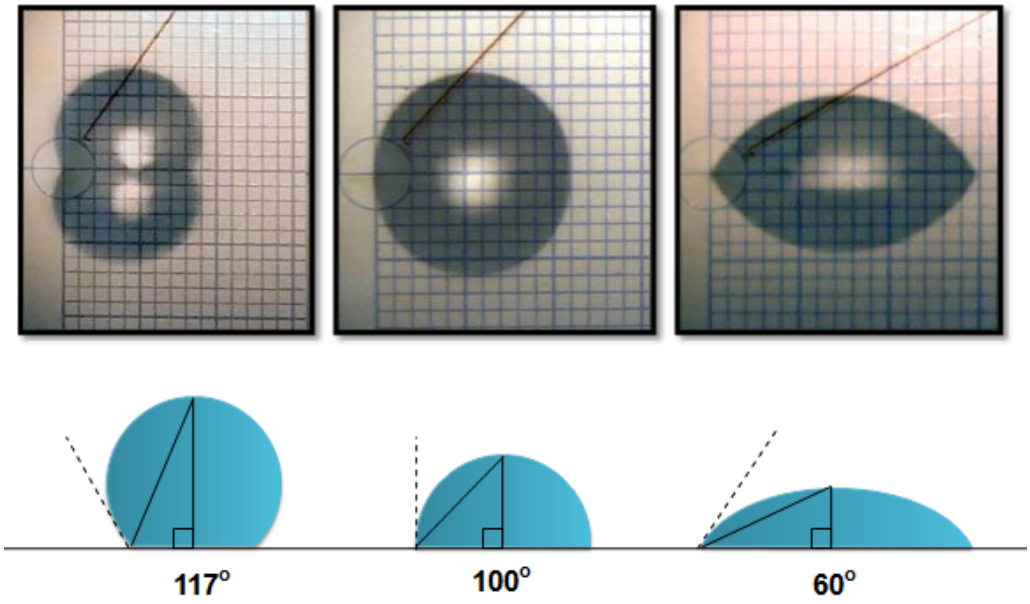

Figure 39. Examples of sessile drop measurements by half-angle method: (a) hydrophobic: nitrogen treatment, (b) control sample (c) hydrophilic: oxygen treatment.

As shown in Figure 40, nitrogen was significantly different from the control group but maintained higher contact angles. The oxygen-only and oxygen-nitrogen treatment groups showed marked lowering of the surface angles, demonstrating an increase in surface energy (Figure 41). In all cases except for control, with aging the surface changes reverted back towards the control values. This illustrates the importance of choosing a relevant surface treatment plasma gas, as well as timely utilization of the modified surface energies before surface reconfiguration to the lowest energy state of the polymer occurs.

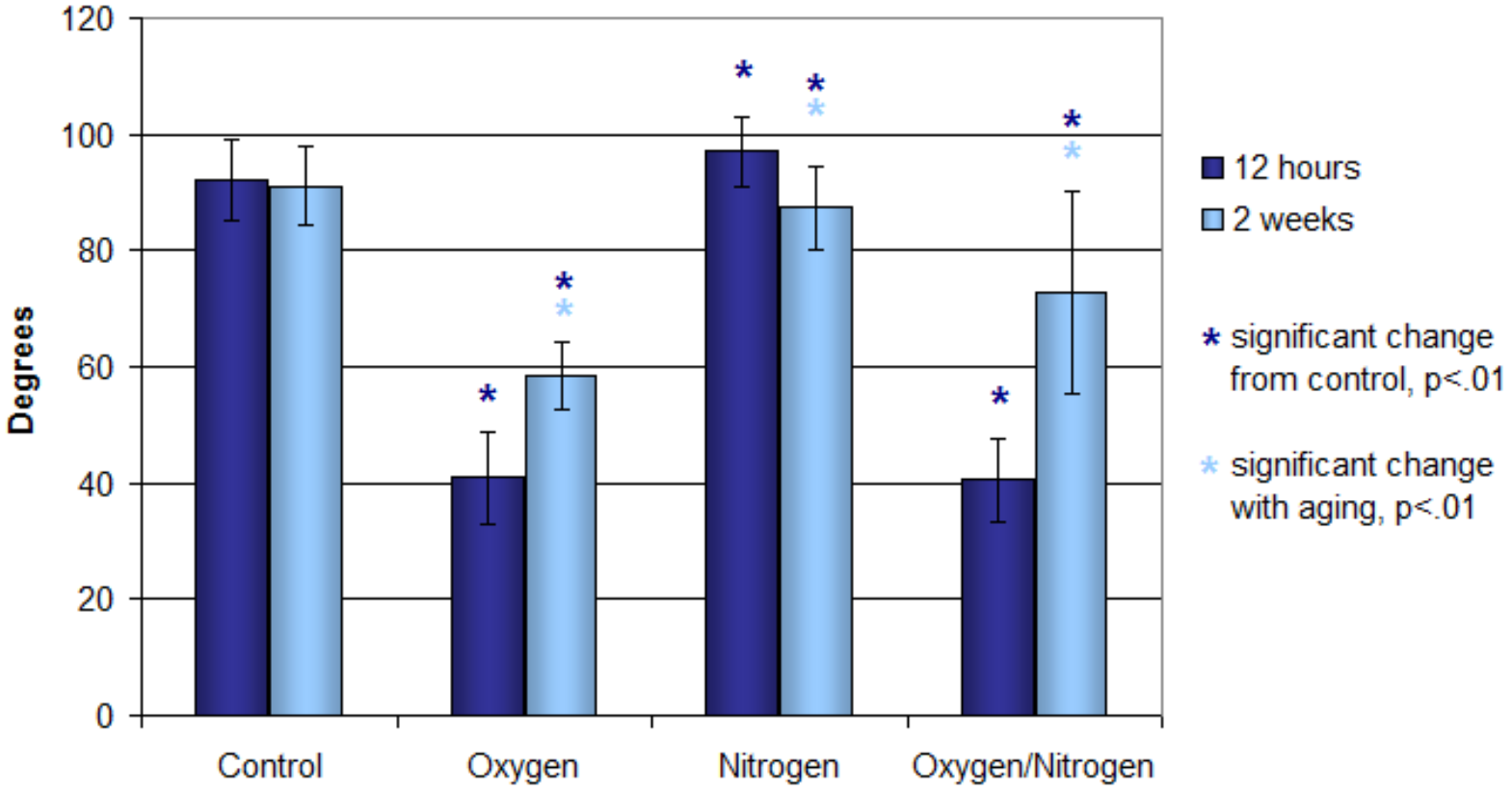

Figure 40. Contact angle measurements across treatment groups.

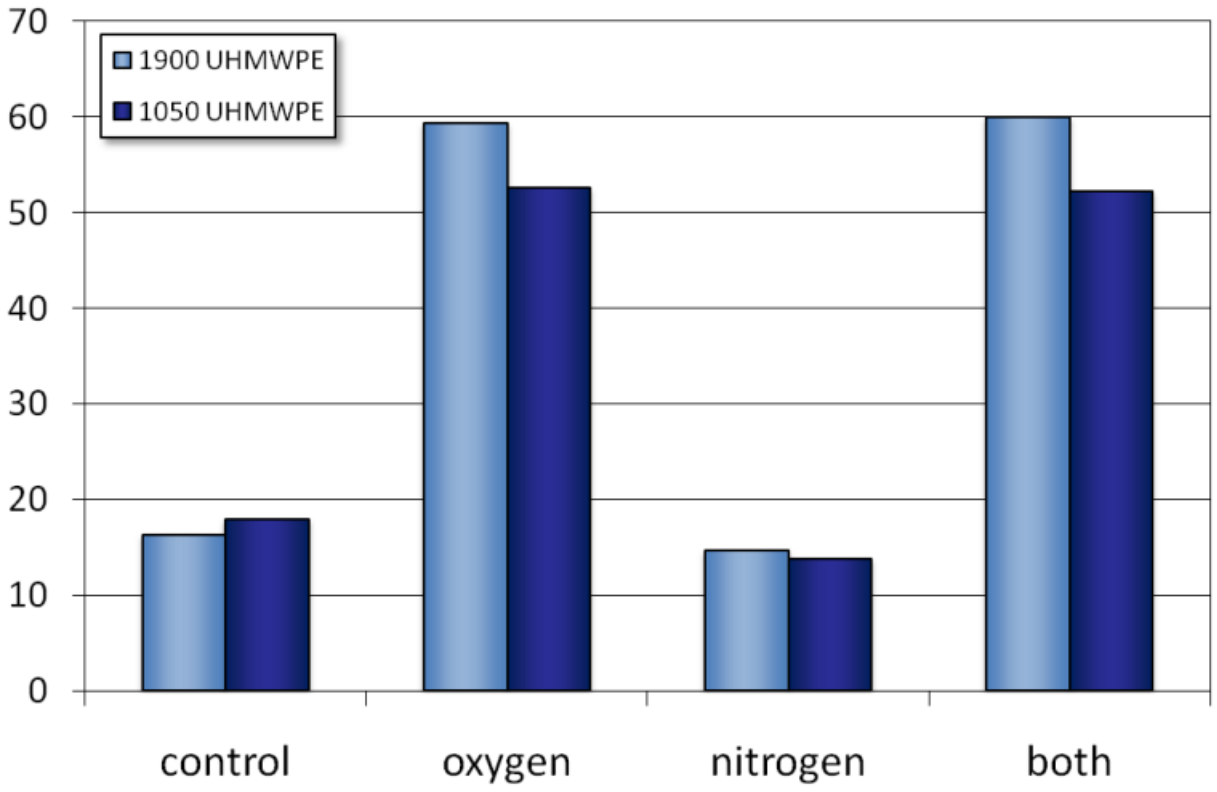

Figure 41. Average GGFY surface energies per treatment group on UHMWPE.

It is also useful to note that plasma sterilization utilizes the addition of small amounts of oxygen to argon or nitrogen to enable enhanced bacterial killing. Integration of surface treatment for application at atmospheric temperature and pressure or manufacturing integration using standard plasma sterilization machines may both be viable solution. Plasma sterilization has gained popularity in the orthopaedic field after gamma radiation in air was shown to adversely affect bulk properties in UHMWPE components. Gamma sterilization is still used, but the required reduced oxygen environment increases the expense of the process.

Plasma exposure time and power are known factors to affect the amount of surface roughening, functionalization, and crosslinking. In addition, the molecular weight of the polyethylene and degree of crystallinity may also be contributing factors to different surface adhesion properties, as they modify the bulk and surface properties. Amorphous regions are more susceptible to chemical attack than crystalline regions, and the degree of crystallinity is a function of deposition parameters and post-deposition handling. The ultraviolet exposures used in photoligthography can also have an effect on the makeup of the parylene surface, but are minor (residing primarily in the top 5% of the parylene layer [56].

A new phenomenon was observed in the parylene layer on some polyethylene substrates. A crystalling pattern with large formations, approximately 5-10 μm across, with a rounded square morphology were observed via optical microscopy. In terms of aspect ratio, their depth appears to be shallow. The size and shape is highly unusual.

Because of the desirable refractive index (1.609-1.678) and practically no optical loss, parylene has emerged as a common coating material in optical applications (especially at visual wavelengths) where artifact free coatings are of utmost importance. The crystals observed are on the order of a few nanometers (Figure 42). Under initial observation under an optical microscope, these structures appear layered within 1.5 µm of parylene atop a plasma-treated UHMWPE sheet film (127 µm thick). The samples with the observed structures were coated at room temperature in a Specialty Coating Systems LABCOTER® system, and underwent storage at room temperature. Parylene-C does not exhibit crystalline melting until 290^{o}C, therefore no melting or recrystallization is assumed to have occurred. Yeh, et al. report the crystallinity of parylene-C films deposited at 25^{o}C to be approximately 35% with a deposition rate of 0.18 g/min [57].

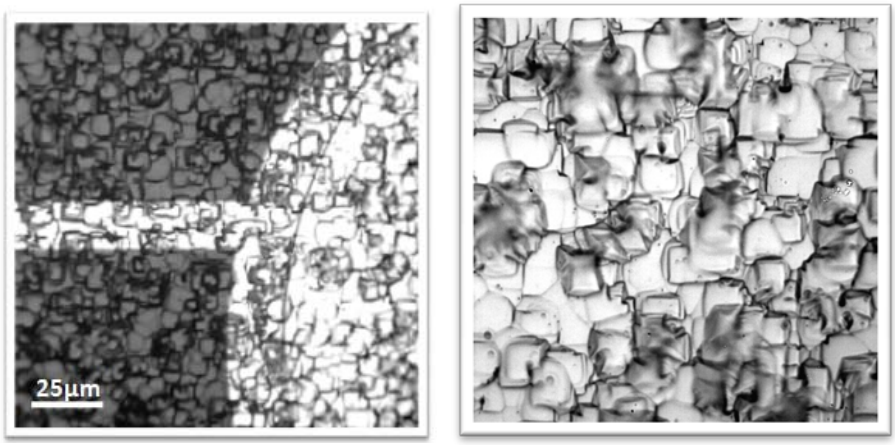

Figure 42. Micrographs of large crystal formation within a 1.5 µm layer of parylene on UHMWPE and gold electrodes, at 50x magnification (left) and 100x magnification (right). Patterned photoresist is present over most of the surface with the exception of the 2nd plate opening.

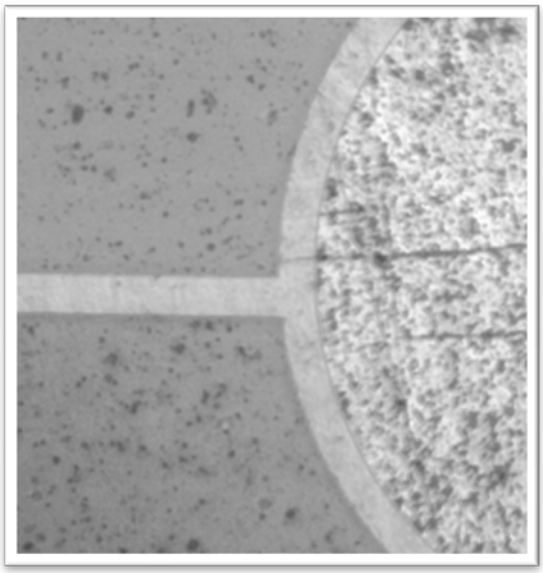

Figure 43. Polyimide wafer showing uniform parylene coating. (Wafer is from same batch as polyethylene wafer in Figure 42 and has also gone 2nd layer patterning without 2nd layer metallization.)

The parylene-C surface is extremely smooth, ranging from 10-25 Å RMS roughness [58-60]. Due to its highly conformal nature, the parylene layer tends to mimic the surface roughness of the underlying surface which is often orders of magnitude larger than the smooth parylene. Furthermore, parylene surface roughness is unaffected by oxygen plasma treatment, but significantly reduces contact angles, demonstrating a very hydrophilic surface [60]. Furthermore, parylene-C is impermeable to laboratory solvents such as acetone, ethanol, and any organic solvent [59] at room temperature up to 150^{o}C.

This discovery leads to many interesting questions and possibly exciting new applications. Does the effect of this new crystal structure affect the surface morphology of the film? Further research is needed to understand the underlying mechanisms and

harness this property of composite polymers for application in cell cuture studies, microfluidics, sensor design, or any other purpose where it may prove useful.

What substrate surface characteristics, if any influence this behavior? It is possible the functional groups formed during plasma surface treatment of the underlying polyimide surface provide seed sites for crystal formation. Furthermore, polyimide shows susceptibility to degradation during prolonged (or higher temperature) acetone exposure, as demonstrated experimentally during the liftoff step of electrode microfabrication in this study. Similar results were not observed with polyimide substrates given the same treatment (Figure 43). Most polyethylene batches demonstrated clear, smooth surfaces as well. No known contaminants were present in the dimer used for parylene-C deposition.

It has been established that parylene etches well with an oxygen plasma etch. Do the crystals exhibit anisotropic etch rates? i.e. higher etching along dimensions of higher crystal order. If true, this may allow the roughening of the surface along the crystal lines or even perhaps the creation of shallow walls or wells within the parylene layer. By identifying the factor(s) that influence large crystal formation, it remains to be seen whether the crystal formation can be predicted and controlled.

Chapter 4. Sensor System Design

4.1. Sensors on Silicon Substrate[4]

An array of parallel plate sensors was designed to find normal forces by measuring axial strain [61]. This array was also used to verify the ability to use a row-column addressing technique to measure the values of individual capacitors. As shown in Figure 15, the upper electrodes of the sensors are connected in series by row and the lower electrodes are connected in series by column.

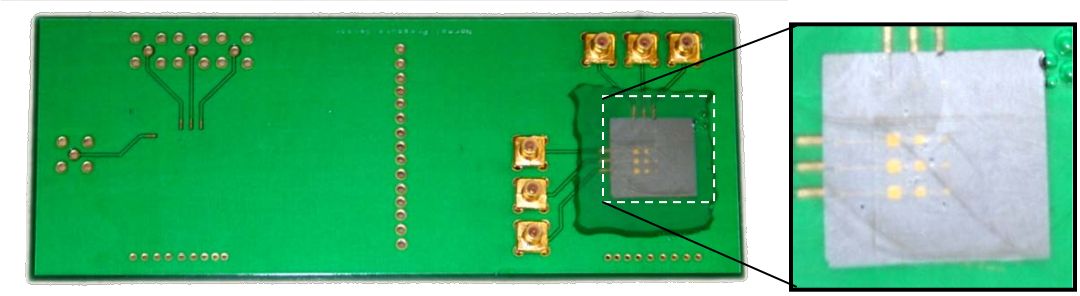

[4] Parallel plate sensors on a silicon wafer were initially reported by Boyd Evans, III in his December 2007 dissertation at the University of Tennessee. I assisted Dr. Evans during the fabrication and testing of these arrays. They serve as a foundation for later sections of this dissertation proposal, and thus a summary is presented in section A.5. For more detail, please refer to [61] B. Evans III, "MEMS Capacitive Strain Sensing Elements for Integrated Total Knee Arthroplasty Prosthesis Monitoring," Department of Mechanical, Aerospace, and Biomedical Engineering, University of Tennessee, Knoxville, 2007..

Figure 44. Parallel plate array fabricated on silicon wafer and mounted on FR4 printed-circuit board for testing.

Individual sensors are addressed by activating the row and column of the sensor of interest. A 3x3 array was constructed with one row each of 10 pF, 5 pF, and 1 pF predicted nominal capacitance using square electrodes.

4.1.1 Fabrication

In order to determine the effect of nominal capacitance on noise and sensitivity, 1 picofarad (pF), 5 pF, and 10 pF capacitors with the dimensions of 275 by 275 micrometers (μm), 614 x 614 μm, and 867 by 867 μm, respectively. The electrodes are a 10 nm titanium layer for adhesion and 300 nm of gold with a 2 μm layer of parylene as a dielectric.

4.1.2 Validation and Testing

The array of sensors was tested using an MTS (Eden Prairie, MN) 858 mechanical testing machine with a 2.5 kN load cell. The sensors were loaded at a rate of 2.5 pounds per second until the peak load was achieved, and then held for 2 minutes before unloading at a rate of 2.5 pounds per second. Peak loads were 25, 50, and 75 pounds and were run consecutively with 2 minutes hold at zero load after each load/unload cycle. Figure 45 shows a plot of the loading profile and corresponding sensor output.

Capacitance was measured with an Agilent (Santa Clara, CA) 4285A LCR meter at 1 MHz. Calibration of the meter was performed both shorted and open with the shielded cables to eliminate cable and other fixtures' capacitance contributions. Sixteen samples per second were taken, and average values were recorded every second to

Labview via GPIB (National Instruments, Austin, TX). Load cell data was also recorded each second.

Table 4. Parallel plate sensors on silicon substrates: Testing Results. Data reformatted from [61].

Sensor	R^2 Coefficient	Capacitance Change with Pressure[5]	
		per kPa	per psi
10 pF	0.936	2.887 aF	64.1 aF
5 pF	0.992	1.87 aF	41.5 aF
1 pF	0.938	.500 aF	11.1 aF

[5] Values given are not intended to represent sensor resolution; rather, they indicate the amount of change for applied loads for comparison between sensors and calculation of total expected change for a given pressure.

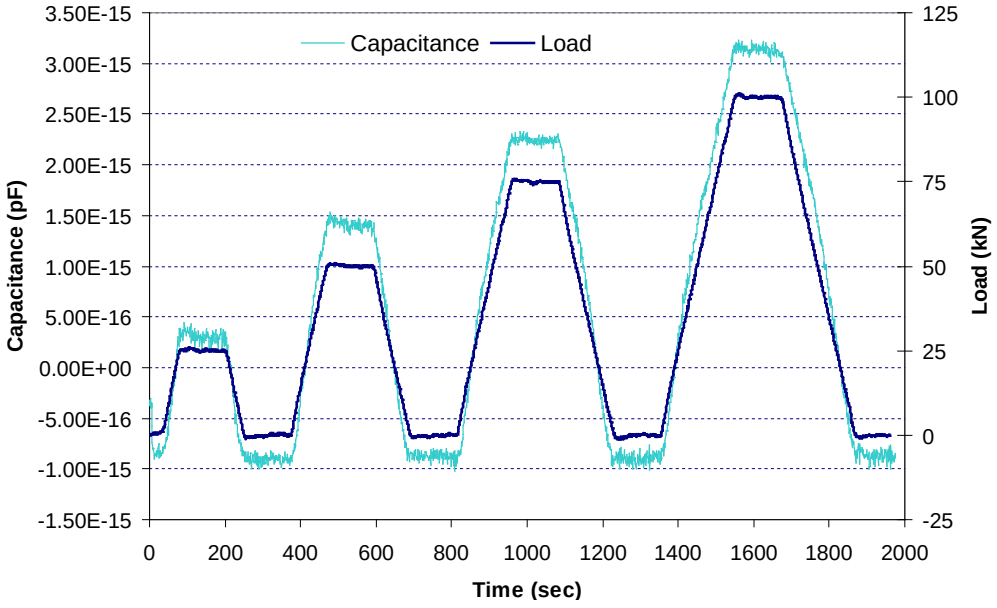

Figure 45. 5 pF capacitive sensor on silicon using a parylene dielectric undergoing mechanical loading [62].

4.2. Conformable Arrays

Although stiff sensor arrays can be configured for adequate pressure measurement on flat surfaces, such as a surgical spacer block, flexible arrays offer significant promise for use in surgical instrumentation. These custom capacitive sensors can operate in a flat configuration or conformed to a curved surface and secured with adhesive, as illustrated in Figure 46. The sensors measure forces normal to the surface, which is especially useful for contact pressures between articulating surfaces. The ability to flex should be distinguished from the ability to stretch. Flexibility implies the ability to bend in multiple directions, while stretchability adds the ability to withstand significant strain within the plane of the sensing array. A flexible circuit favors uses where there is bending primarily about a single axis, since large angles of bending about other axes may cause wrinkling of the material. Thus a stretchable material enables better conformity for an irregular surface, especially at sharp points. In the experimental sections and discussion that follow, “flexible” and “conformable” are used interchangeably and do not imply any stretchability (i.e. a flexible film can be conformed to a surface given no sharp changes in surface topology).

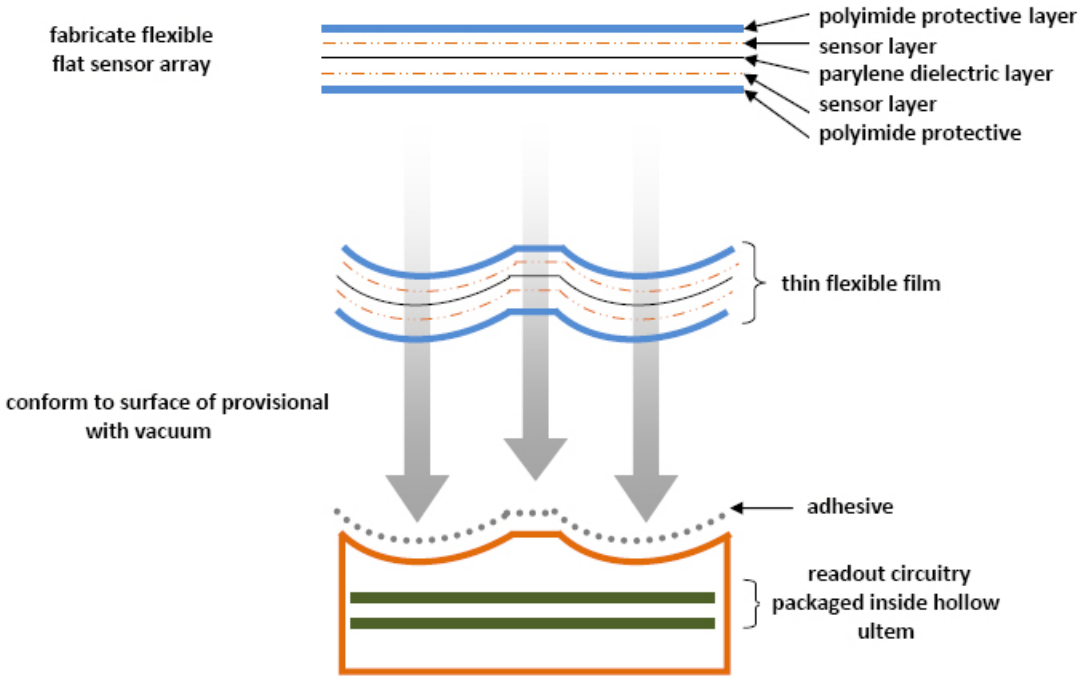

Figure 46. Flat flexible arrays can adhered to the surface of a provisional, with electronics housed inside.

4.2.1 Proof of Concept

First, a flexible parallel plate capacitive array of 5 picofarads (pF) nominal capacitance each was designed for fabrication in a standard flex circuit facility. Unicondylar sensor arrays, designed in house and fabricated at Advanced Circuits (Aurora, CO) successfully underwent preliminary testing with compressive loading (Figure 3). An improved flexible array utilizing standard flex circuit technology was designed. Both these first two iterations utilize stiffener for attachment of shielded connections for sensor readout. The second array is comprised of 3 pF nominal

capacitance sensors in an array, shown in Figure 47. Each individual sensor shows a low, non-linear change with loading to 100 lbs.

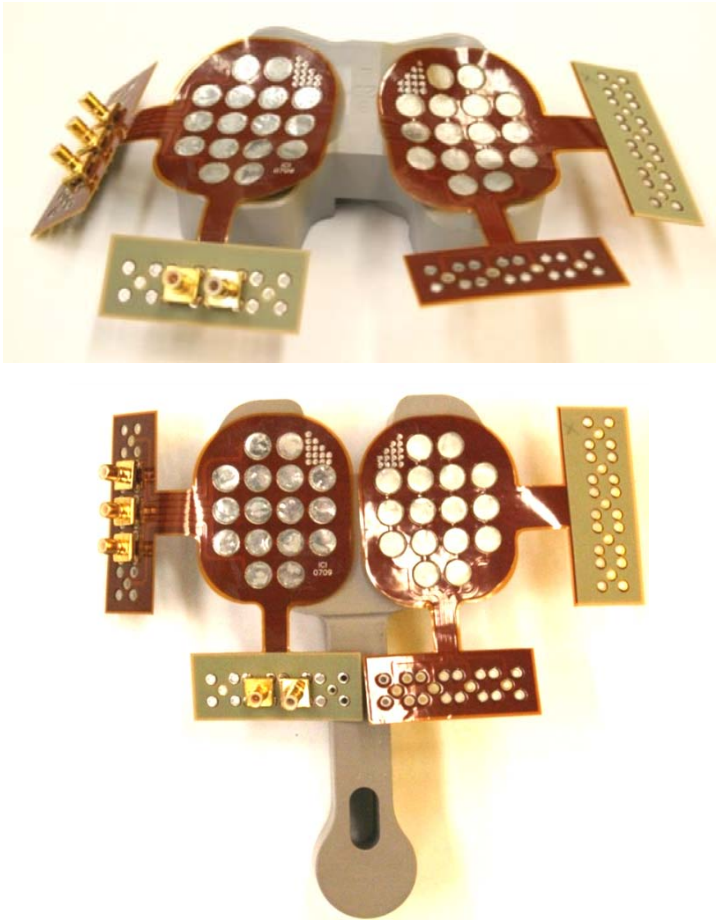

Figure 47. Prototype unicondylar flexible arrays placed on a provisional (top), and first iteration standard flex unicondylar arrays flat on spacer block (bottom).

Table 5. Summary of Various Fabrication Iterations.

Iteration	Description	Capacitance	Flexibility*
1	standard flex, proof of concept		5
2	standard flex with ground plane, proof of concept	3 pF	2
3a	microfabricated, 25 µm polyimide	5 pF, 20 pF	9
3b	microfabricated, 50 µm polyimide	5 pF, 20 pF	7
3c	microfabricated, spin-on polyimide	5 pF, 20 pF	0
3d	microfabricated, ~10 µm parylene	5 pF, 20 pF	10
3e	microfabricated, 50 µm UHMWPE	5 pF, 20 pF	7
4a	Full tibial tray microfabricated on 50 µm polyimide	5 pF	7
4b	Full tibial tray microfabricated on UHMWPE	5 pF	7

*rated from 0 – 10: rigid to very flexible

Figure 48. Flexible 3 pF capacitive array on provisional (right) and spacer block (left).

Further reductions of capacitive size are achievable with photolithography-based microfabrication; the limiting factor is ability to read the sensor (i.e. reliably detect minute changes in capacitance). Custom substrates, thinner dielectric materials, and biocompatibility options are all advantages to these new sensors, but care must be taken for electrical cross talk between excited sensors. In addition, the smaller the sensor, the smaller the change in capacitance with applied load; changes can become hard to detect even with custom cutting-edge readout circuitry.

4.2.1.1 *Choice of Dielectric*

Based on the manufacturing processes governing thickness and the dielectric constant of each material, the theoretical capacitance was calculated for a capacitor with 500 µm diameter plates using different dielectric materials, as shown in Figure 48. Parylene is the optimal material, resulting in a theoretical capacitance of 3.5 pF, primarily due to the 1-2 µm dielectric thickness and absence of adhesive. Parylene was selected as the dielectric for future experiments.

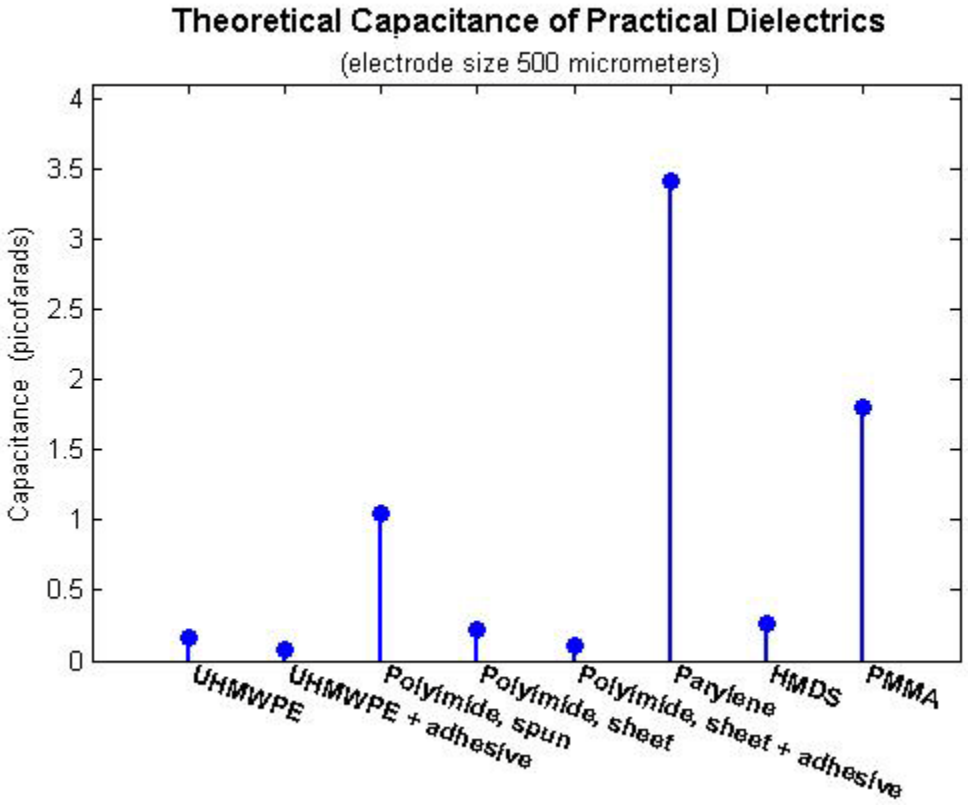

Figure 49. Capacitance using 500 µm diameter plates and laboratory-accessible dielectrics of practical thicknesses.

4.2.2 Design and Fabrication

Smaller arrays were designed with greatly reduced footprint, as shown in Figure 18. Four test designs were fabricated using the layer methodology outlined in Figure 49. First, cleaning was carried out, after which electrodes were patterned on the surface using standard photolithography techniques. Samples were coated with NFR 016 55cP 255 photoresist by spin-casting (Doe and Ingalls, Durham, NC). The substrates were soft-baked on a hotplate at 90° C for 2 minutes and exposed using a Karl Suss MA6 mask aligner (Waterbury Center, VT). A 2 minute post-exposure bake was performed prior to development in positive resist developer. In the case of the compression-molded samples, bake times were increased significantly to allow proper photoresist solvent evaporation during pre- and post-exposure bakes. Liftoff was achieved in acetone.

Parylene C was used as the dielectric layer (dielectric constant of 3). A Specialty Coating Systems Parylene Deposition System was used with 1.0 ± 0.001 g dimer per batch. Dielectric thickness was approximately 1.5 µm thick. The parylene deposition process is a conformal, pin-hole free thin-film process completed at room temperature. Pads to access the sensor lines on the bottom layer were left uncoated by masking either by a photoresist layer or by tape.

The same photolithography process was used for the upper electrode patterning after parylene deposition. A protective parylene layer was then deposited over the capacitive plates, with pads left open to air (Figure 50).

Each circular sensor is .5 mm across. Polyimide was demonstrated as a substrate material, and parylene as the dielectric material (1.5 μm). It is noted that parylene has served as a substrate layer in early capacitive fabrication when the sensor was left on the silicon wafer, but it poses a problem due to adhesion and mechanical strength of the thin film during removal from the silicon substrate. A negative-resist based photolithography fabrication was implemented to reduce time and number of steps for fabrication. The electrodes consist of a 10 nanometer (nm) titanium adhesion layer and 300 nm of gold deposited on the substrate via physical vapor deposition.

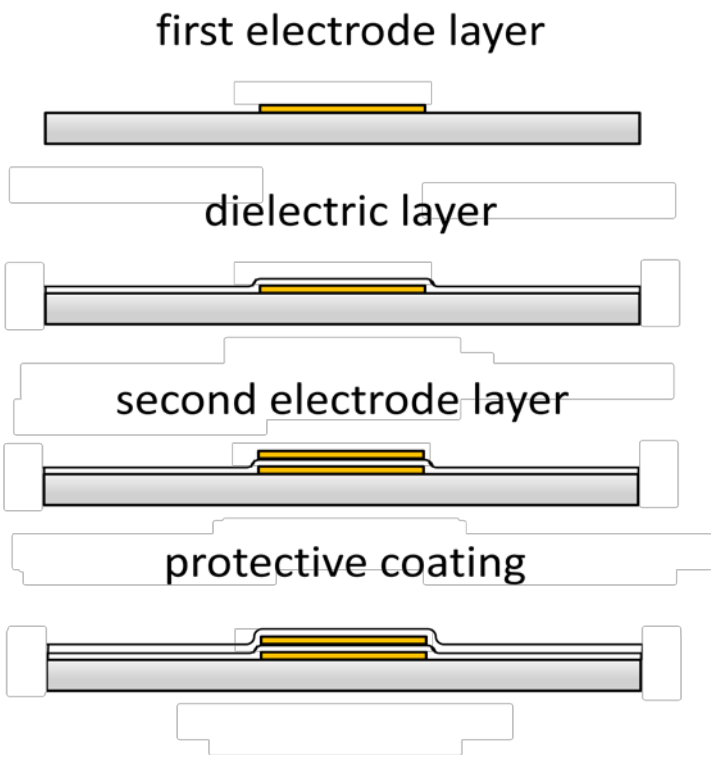

Figure 50. Device microfabrication steps.

Array design is multi-faceted to understand the behavior of the sensors at a small scale and to optimize design to boost readout speed, increase nominal capacitance, and decrease crosstalk and parasitic effects specific to the configuration of this array. Increasing nominal capacitance is most easily achieved through larger electrode size and thinner dielectric layers, thus presenting a tradeoff between keeping sensor size to a minimum and nominal capacitance at an appropriate level for accurate measurement. Similarly, the spacing needs to be optimized between closeness (providing high spatial resolution across the array), and crosstalk (sensors too close to one another affecting readout, although excitation timing also plays a role). As shown in figures 18 and 19, four sensor layouts were designed; 1mm electrodes with 1 mm between sensors (2mm center-to-center), 1 mm electrodes with .5 mm between electrodes (1 mm center-to-center), .5 mm electrodes with 1.5 mm between electrodes (2mm center-to-center), and .5mm electrodes with .5 mm between electrodes (1 mm center-to-center).

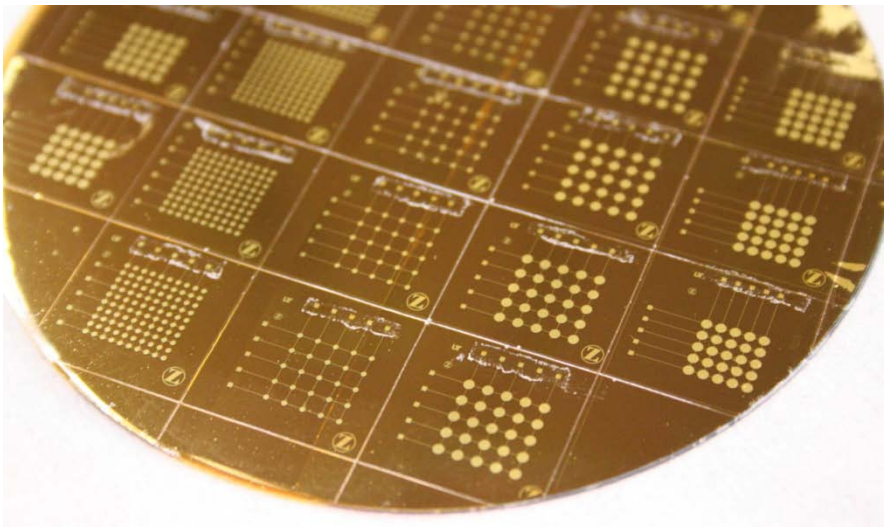

Figure 51. Wafer with multiple size test arrays.

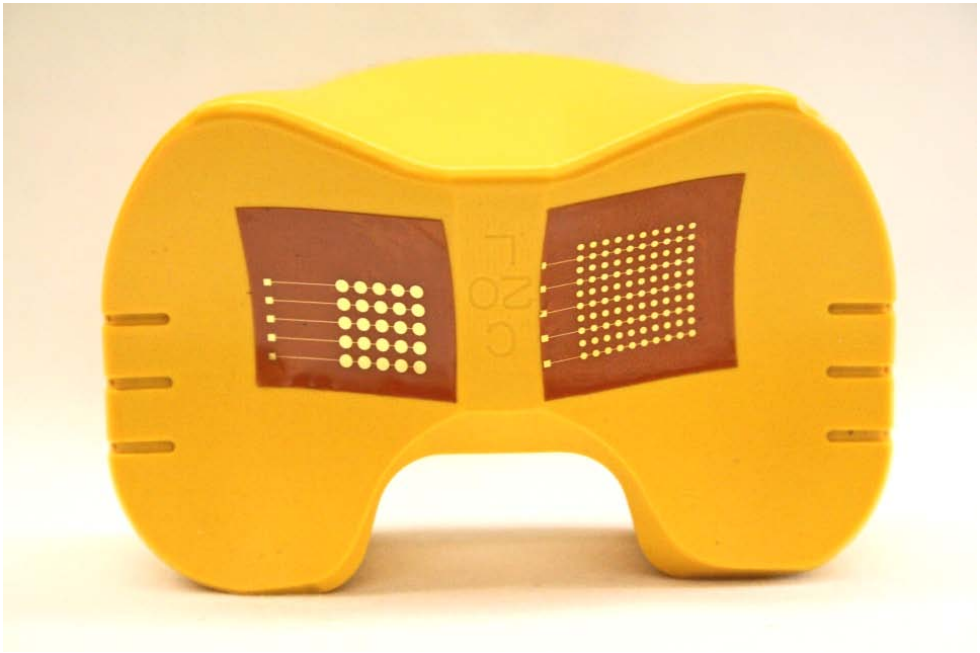

Figure 52. Test sensor arrays mounted on the articulating surface of a knee provisional, showing the conformability of the array on the instrument surface.

4.2.3 Sensor Testing

Sensor arrays were diced by hand on the surface of the wafer and removed with a spatula. They were then adhered to FR4 printed circuit boards and conductive silver-filled epoxy was used to connect the sensors to the circuit board. A protective polyimide layer was placed over the electrodes and a second protective layer over the entire assembly after the epoxy had cured. Sensor arrays were mounted flat on FR4 printed circuit boards for capacitance reading via subminiature B (SMB) using a 4285 LCR meter (Agilent, Santa Clara, CA). After calibration of the shielded lead wires, nominal capacitance of each individual sensors within each array was measured without load, pre-loaded with 5 lb, and then monitored continuously with loading up to 444 N and 667 N (80 lb and 155 lb at 1.5 lb/min) on a hydraulic MTS (Eden Prairie, MN) 858 mechanical testing machine with a 2.5 kN load cell. The arrays were unloaded at the same rate. A 1MHz frequency was used at 2 volt peak-to-peak excitation on the LCR meter. An average value of 16 samples per second was recorded each second via GPIB cable to a computer. The MTS testing machine recorded data at the same interval. Data from the LCR meter was read and saved with Labview software (National Instruments, Austin, TX). Machined polymer pieces (polyacetal resin) were used to administer the load to minimize noise.

The standard flex circuit design incorporated rigid flex so the SMB connector could be directly attached for measurement with the LCR meter.

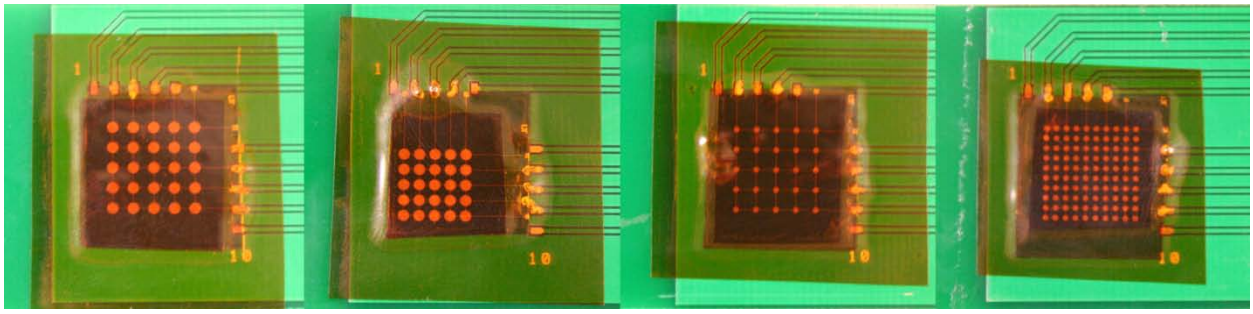

(a) **(b)** **(c)** **(d)**

Figure 53. Microfabricated sensor arrays of varying size and spacing mounted on FR4 circuit boards for testing. Sensor Diameter:Center-to-center spacing, in mm: a) 1:2 b) 1:1.5 c) .5:2 d) .5:1 .

4.2.4 Mechanical Testing

The sensing array should be calibrated and validated within the application pressure range on a mechanical testing machine. The sensor response to loading and unloading, hysteresis, baseline drift, and resolution are established under known compressive loads from 0 to 2 MPa. The ability to map pressure profiles across the sensing array is also demonstrated in benchtop testing.

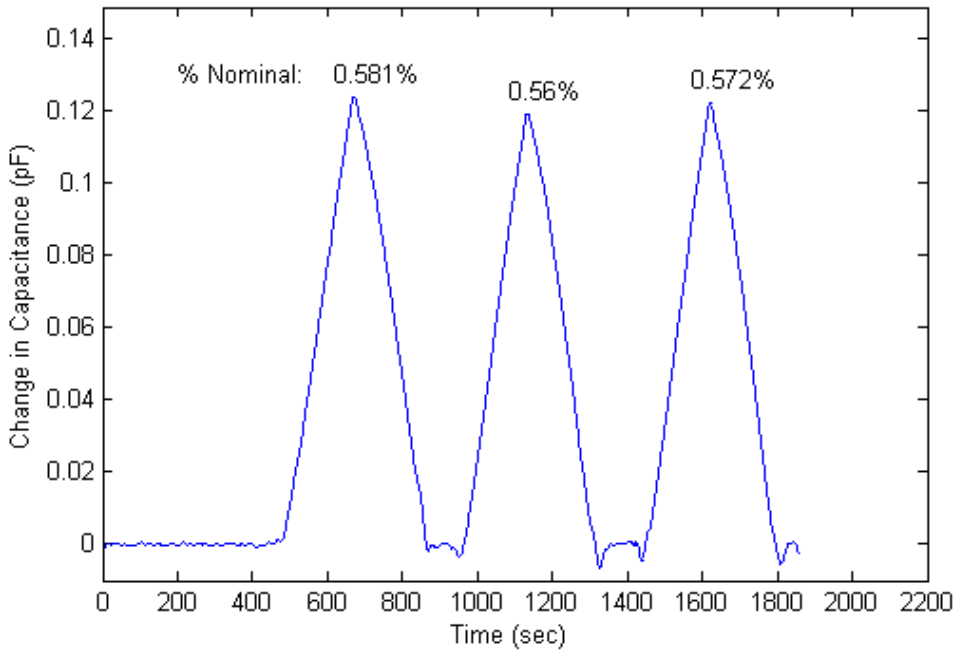

Figure 54. Data with noise and baseline correction for sensor with 21.077 pF nominal capacitance.

Table 6. Comparison of capacitive response for repeated loads.

Capacitance rates for 1 lb/sec loading	
0.000665 pF/sec	loading cycle 1
-0.000669 pF/sec	unloading cycle 1
0.000717 pF/sec	loading cycle 2
-0.000676 pF/sec	unloading cycle 2
0.000720 pF/sec	loading cycle 3
-0.000720 pF/sec	unloading cycle 3

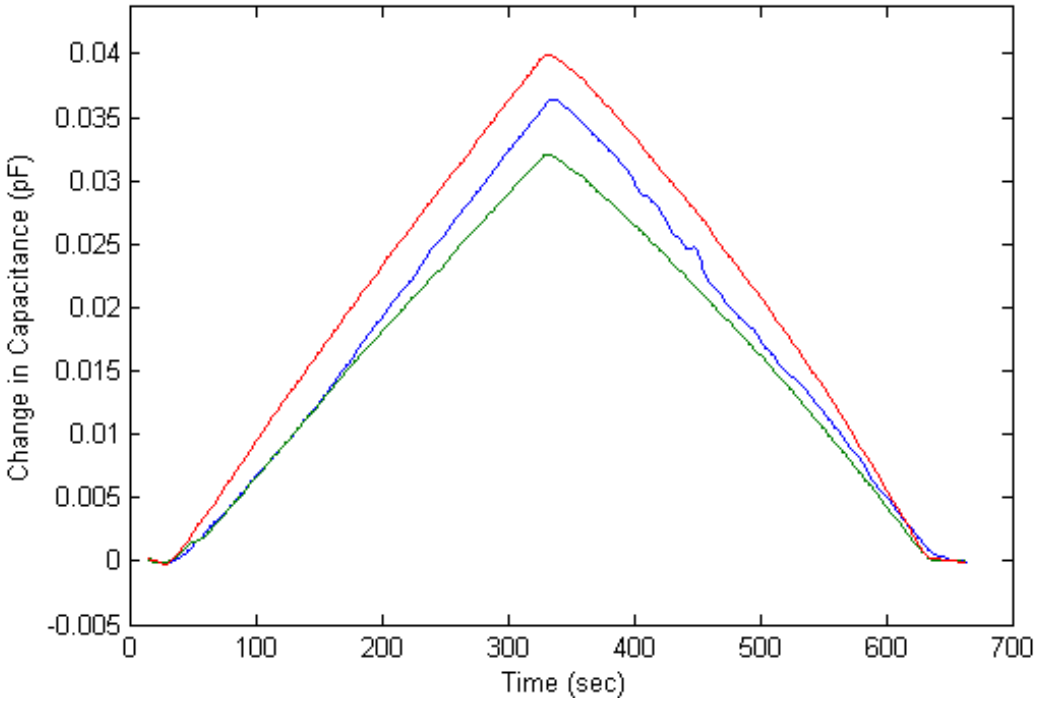

Figure 55. Loading and unloading of 2.25 MPa for three sensors in a row, with noise removal. Sensors are 0.5 mm in diameter with 0.5 mm edge to edge spacing.

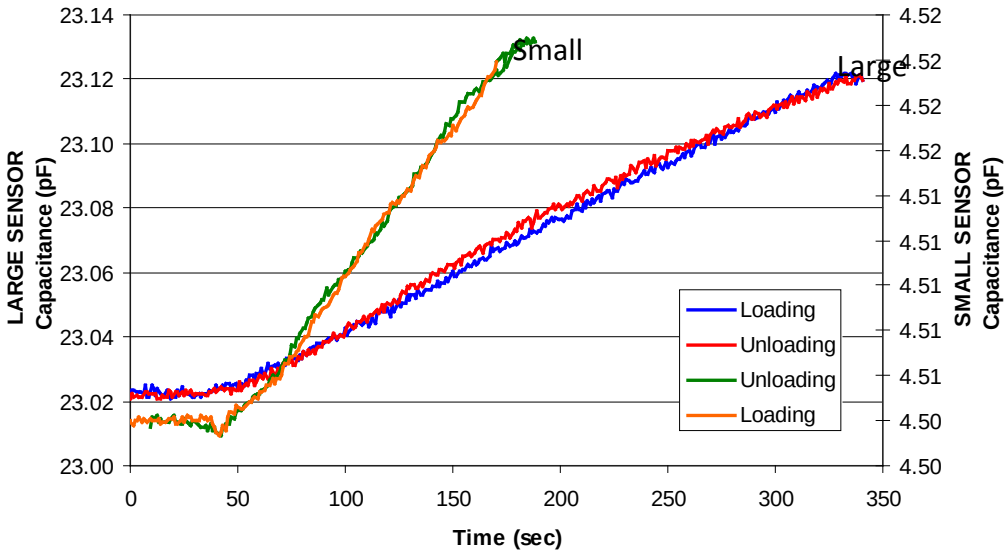

Figure 56. Loading and unloading raw data for a sensor in large dense array (to 700 kPa) and small dense array (to 350 kPa). Nominal values are 4.505 pF and 21.023 pF, respectively.

The 23 pF sensor showed 30 fF of capacitance change per pound load (Figure 56) which can also be interpreted as 15 fF change for each 10 kPa of pressure applied. Similarly, the 5 pF capacitor showed 1.4 fF capacitance change per pound load, or 0.7 fF per 10 kPa (.01 MPa) applied pressure. For comparison, previous studies have shown 1.6 MPa maximum pressure in the intraoperative knee with a resolution of .3 MPa (300 kPa)[20]. Thus our capacitive sensors are deemed to have adequate load resolution. In addition, the density of the sensing array provides superior spatial resolution, which is higher than the sensor-to-sensor spacing with standard post-processing interpolation but has not yet been quantified.

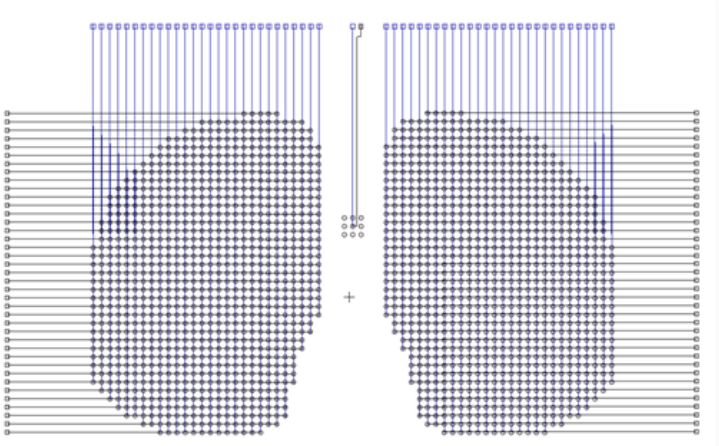

Figure 57. Capacitive array design.

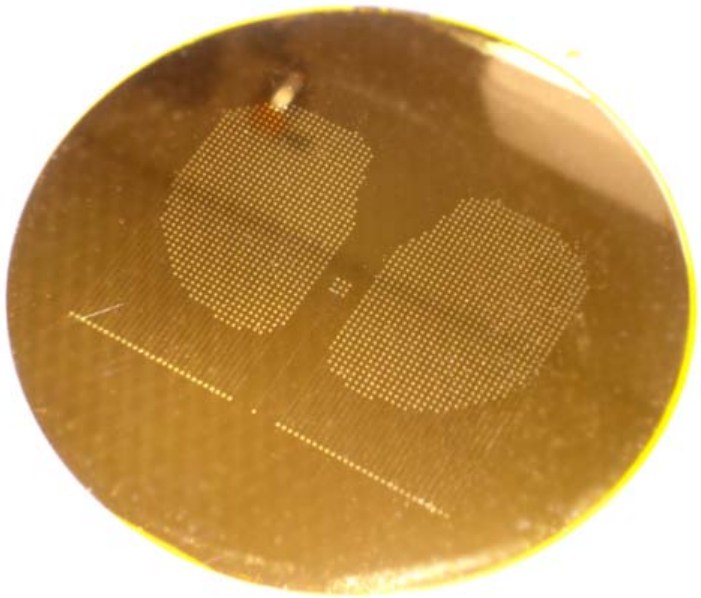

Figure 58. Capacitive sensor array bottom layer fabricated on polyimide on a silicon wafer. Array has 970 sensors per condyle.

Two large capacitive arrays were designed with the dense 5 pF configuration (electrode diameter .5 mm and center-to-center spacing of 1 mm). Sensor density is 100 sensors per square centimeter. A reference capacitor is included between the condyles to enable the option of differential capacitive measurement which not only reduces noise but also compensates temperature effects. Dummy sensor pads are placed around the reference capacitor for appropriate matching with sensors in the array during measurement. This array can be adhered to a curved provisional surface as visualized in Figure 51.

Sensors were then fabricated on polyethylene sheet, which was adhered to a silicon wafer for processing and peeled off after all fabrication layers are complete.

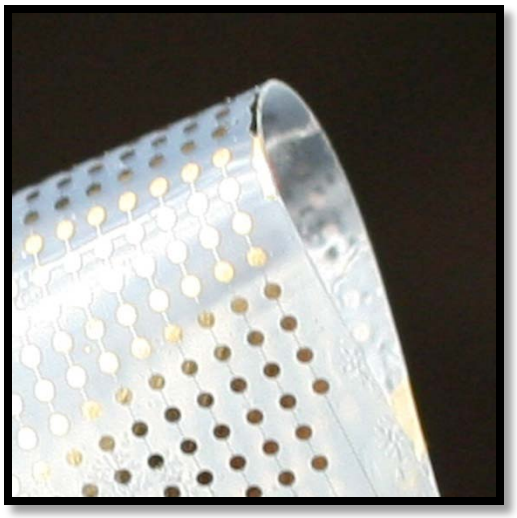

Figure 59. Sensor array after removal from wafer, showing flexibility.

Figure 59 shows an UHMWPE sensor array atop an UHMWPE implant component. Edge wrinkles can be fixed with a stronger adhesive; however, a molding and heat anneal in a final implant product eliminates any adhesive and allows a solid polyethylene block with sensors. The sensors may be placed on the surface of the implant, but that exposes them to the possibility of wear and thus premature sensor failure. It is recommended that the sensors be placed within the volume of the UHMWPE block by molding two blocks. The further away from the articular surface, the more computer simulation is needed to calculate the resulting pressure map at the articulating surface.

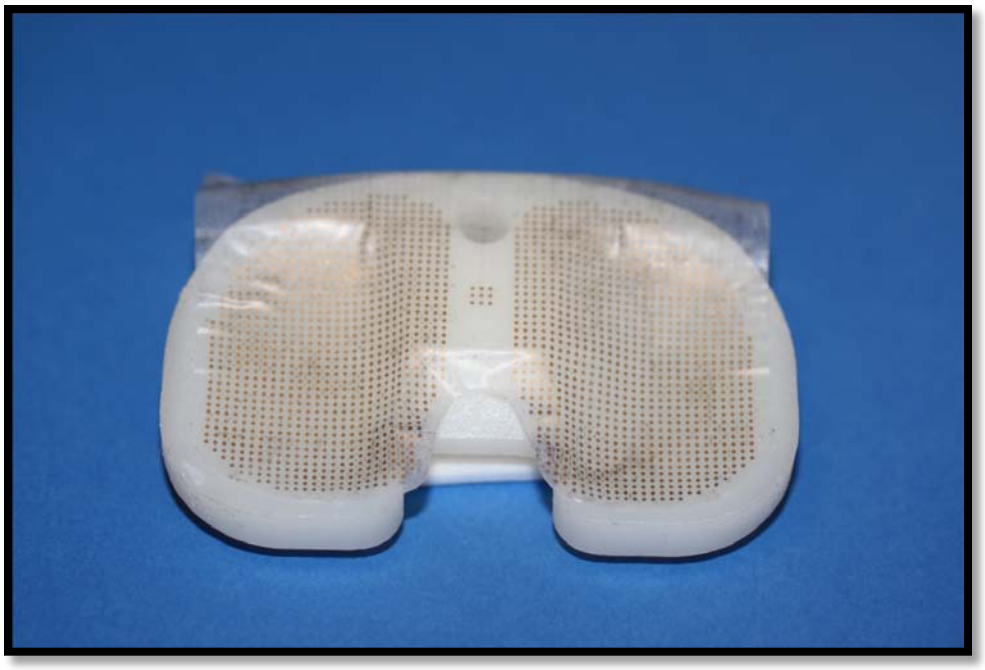

Figure 60. Polyethylene sensor array shown on arbitrary UHMWPE implant component.

4.3. Baseline Correction

Savitzky-Golay algorithms were originally described by 1964 by Abraham Savitzky and Marcel J. E. Golay. It became widely used spectrometric measurements for noise removal, and has since expanded to a number of other fields as a generalized noise removal tool. It performs a least squares regression on a window of size *n* across the signal, thus preserving signal features that may be lost with other smoothing algorithms. The least squares regression can be weighted to tweak filter performance if needed. As a type of finite impulse response (FIR) filter, Savitzky-Golay is used for both noise removal on the main signal, and for removal of small baseline drift that occurs despite shielding implemented to minimize drift.

For a signal $f_i = f(t_i)$ where $t_i = t_0 + \Delta t$ where Δ is a constant so that time sampling is equally spaced, a digital filter, *g*, is designed to approximate the signal, *f*, for each datapoint by replacing each datapoint with a linear combination of its nearest neighbors,

$$g_i = \sum_{n=-k}^{k} c_n \, f_{i+n} \tag{25}$$

which assumes a symmetric window of size *2n+1* around the datapoint of interest. A moving average provides the simplest example of this type of filter, where

$$c_n = \frac{1}{2k+1}. \tag{26}$$

However, a moving average is not ideal for treatment of real-world signals, as it tends to reduce local maxima and increase local minima and widen both maxima and minima, thereby flattening the signal over and beyond noise smoothing.

Savitzky-Golay algorithm finds new filter coefficients, c_n, by using a polynomial fit of the points within the moving window. The polynomial fit is optimized by minimizing the least-squares error using

$$A_{ij} = i^j \tag{27}$$

$$i = -k, \dots, k+1 \tag{28}$$

$$j = 0, \dots, M \tag{29}$$

where a polynomial of degree M is fit to the values of $f_{-k}, \dots, f_{k+1}$ to produce

$$a_0 + a_1 i + a_2 i^2 + \cdots + a_M i^M. \tag{30}$$

Then g_0 (Eq. 25) is the value of the polynomial at $i=0$, or a_0. In matrix notation, this is written as

$$(A^T \cdot A) \cdot a = A^T \cdot f. \tag{31}$$

When f is replaced by a unit vector, u, we have a convenient way to find solutions for many datapoints with windows where $c_n=a_0$:

$$c_n = \{(A^T \cdot A)^{-1} \cdot (A^T \cdot u_n)\}_0 = \sum_{m=0}^{M} \{(A^T \cdot A)^{-1}\}_{0m} n^m. \tag{32}$$

The Matlab signal processing toolbox was utilized to implement Savitzky-Golay filters- one for smoothing of overall signal noise, and one for baseline correction by

removal of very low frequency noise. A 4th order filter is used to smooth out unwanted noise from the sensor signal. A 7th order filter is used to compensate for low-frequency noise that causes the baseline drift. Figure 60 shows the raw data from a calibration test of the flexible sensors. The processed waveform is presented in Section 4.2.4. in Figure 53. Further detail is provided in Appendix A: Experimental Code.

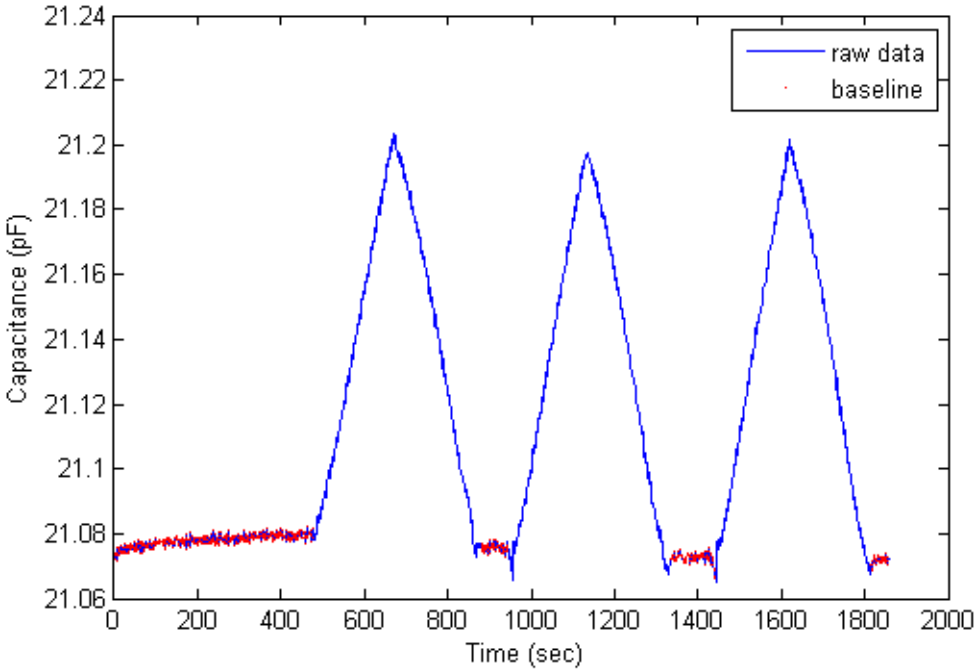

Figure 61. Raw rata for three consecutive load/unload cycles of sensor with 21.077 pF nominal capacitance. Baseline is selected from raw data is highlighted red. Maximum applied pressure is 2.25 MPa plus 0.05 MPa preload.

Chapter 5. Hardware Design

5.1. Readout Circuitry

5.1.1 Intra-operative Readout with Bluetooth

A series of 5 iterations of hardware design were carried out, iteratively improved and refined each time. The proof of concept board was wired to the DAQ to validate using the AD CDC chip for the application at hand. Sensors were input to the board using mini-SMB cables and connectors, allowing manual switching by changing the cable position (Figure 61). This board was validated using silicon capacitive sensors from previous work and comparing to existing LCR meter data [62]. The first iteration board until mechanical testing is shown in

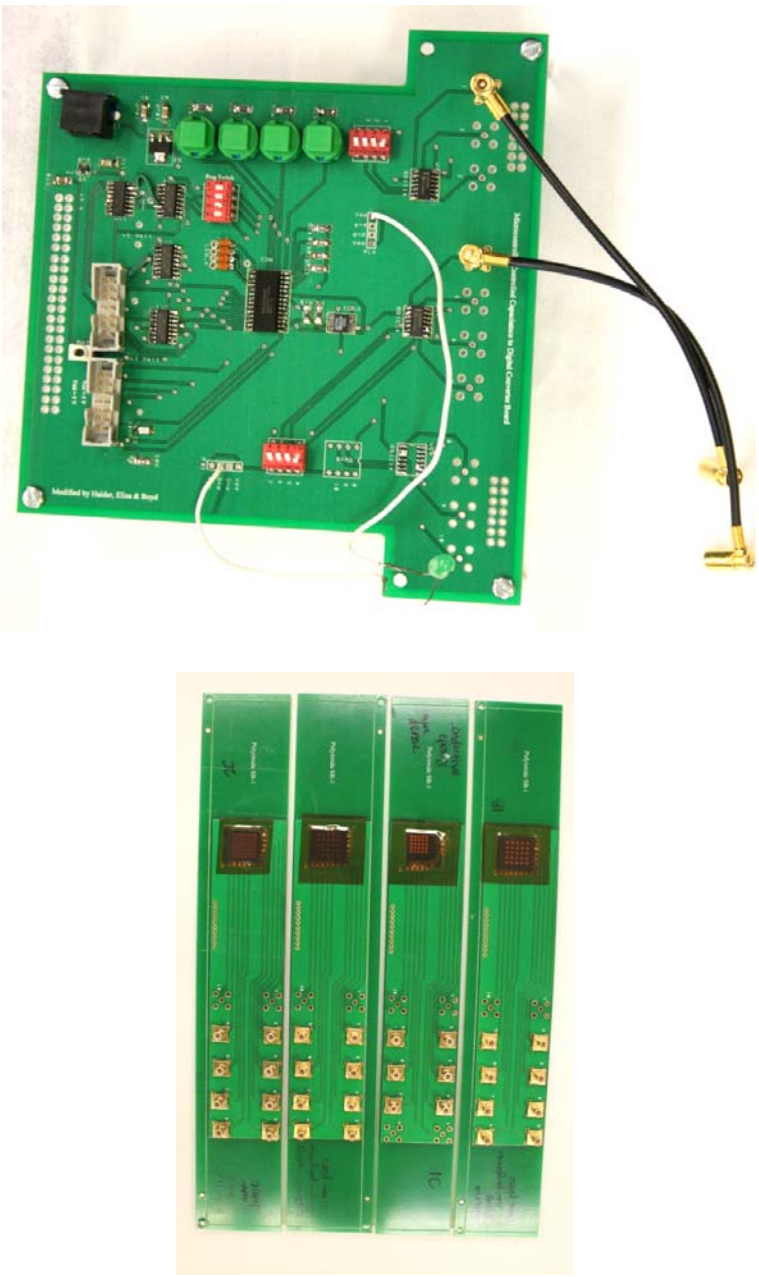

Figure 62. First iteration proof of concept hardware configuration, showing CDC board and flex sensor boards.

A printed circuit board (PCB) and Labview program have been implemented to utilize an existing 24-bit capacitance to digital chip from Analog Devices[1]. The printed circuit board iteration 1, shown in Figure 62 is designed to utilize the chip for reading hardwired capacitors and monitors the capacitance at a rate of 50 Hz. The RMS error is 3.77556 fF for a reference capacitance of 4.255 pF.

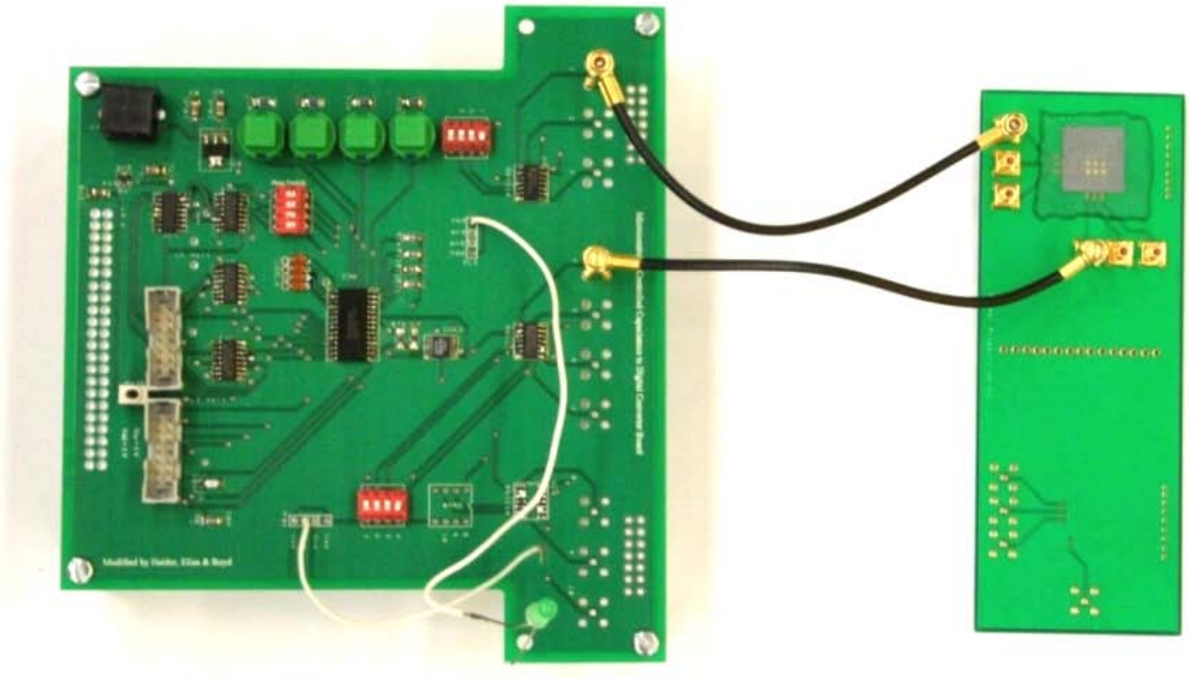

Figure 63. First iteration CDC board with silicon sensors for validation of the test circuit with previous results.

The circuit has been tested with continuous load on a 5 pF nominal capacitance (Figure 62). The Labview program monitors the capacitance at a rate of approximately 1 data point per second for the first iteration. The RMS error is 3.77556 fF (10^{-15}) for a reference capacitance of 4.255 pF (Figure 64).

The AD chip and readout board were tested with the silicon capacitive sensors under loading, as shown in Figure 64. A slight shift in baseline after the load test is attributed to hysteresis of the flex system materials, not abnormalities in the readout. There is also a sign change in the signal processing to lend a more intuitive presentation of the capacitive data for trend comparison purposes. Noise for a reference capacitance of 4.532 pF as measured using the Analog Devices chip. Shift in the baseline (~0.001 pF) is attributed to additional capacitance within the readout circuit Figure 64.

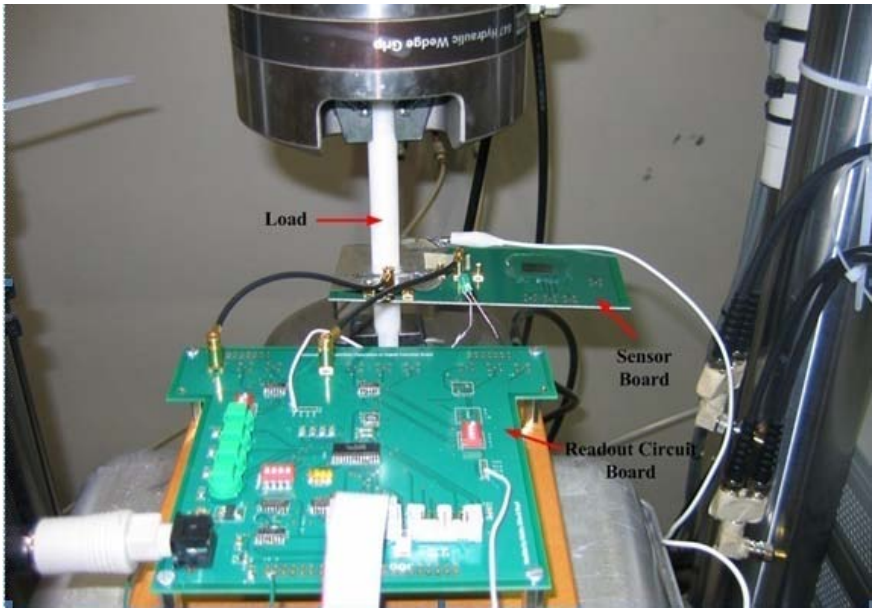

Figure 64. Testing setup showing CDC board connected to sensor board under loading.

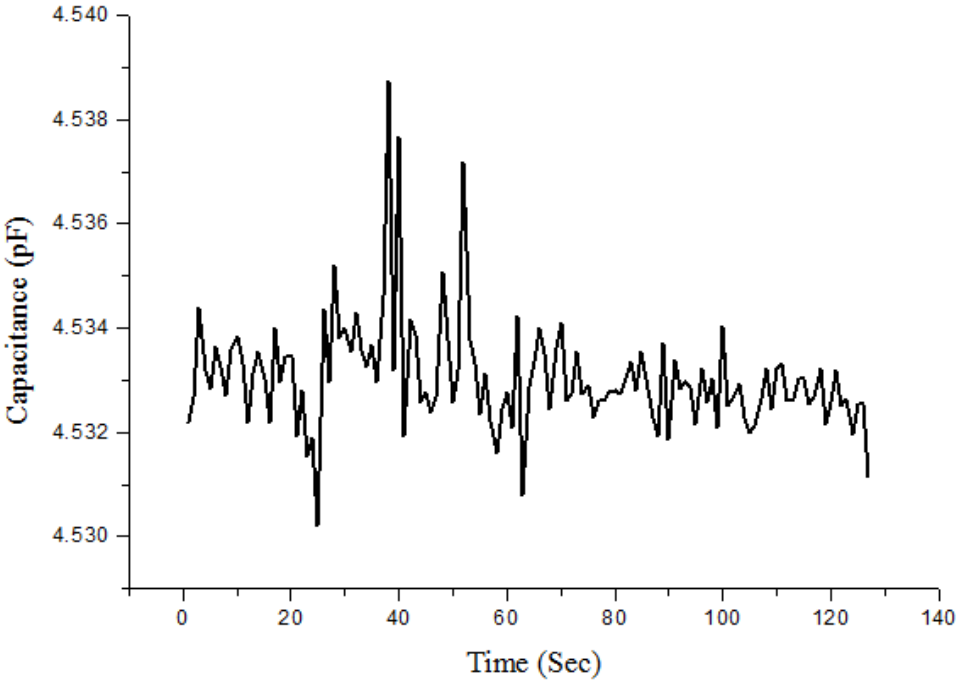

Figure 65. Baseline noise of the system for CDC board iteration 1. Noise of the load machine is inherent in the measurement.

A Labview virtual instrument was written to send the control signals to the µC, read sensor data from the µC through the DAQ, and display the output on screen. The front-end application is shown in Figure 65.

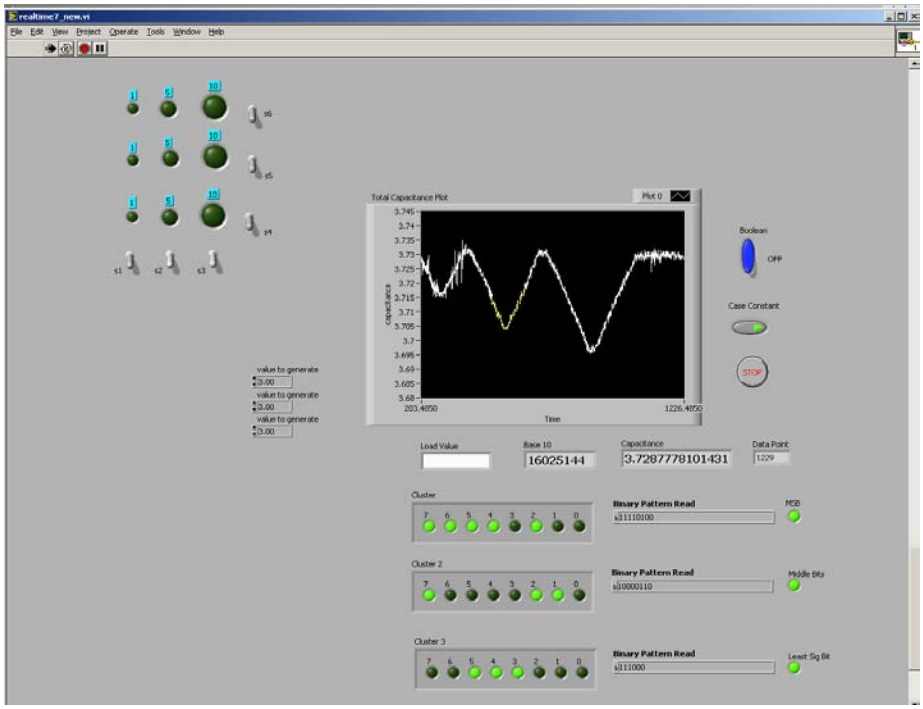

Figure 66. Labview interface for hardware iterations 1, 2, and 3. In iterations 2 and 3, the sensor within the array is selected through Labview instead of manually.

A second iteration of PCB board utilizing the AD chip was designed, as shown in Figure 67. The footprint of the board has been reduced to fit within the provisional shape and additional functionality has been added. Multiplexers (Analog Devices ADG 706) have been added for automated sensor addressing so that a 4x4 array can be read with each sensor readout cycle. Bluetooth capability has been added for wireless data transmission to a receiver. A microcontroller (MSP430x1232) is used for programming the capacitance to digital chip and configuring the Bluetooth antenna. The PCB is designed to interface with the small 1x1 cm arrays (Figure 52) and the large provisional array (Figure 57). It is noted that with smaller array reading capability the sensors to be

read are evenly spaced throughout the large array until suitable electronics to read the entire array can be designed.

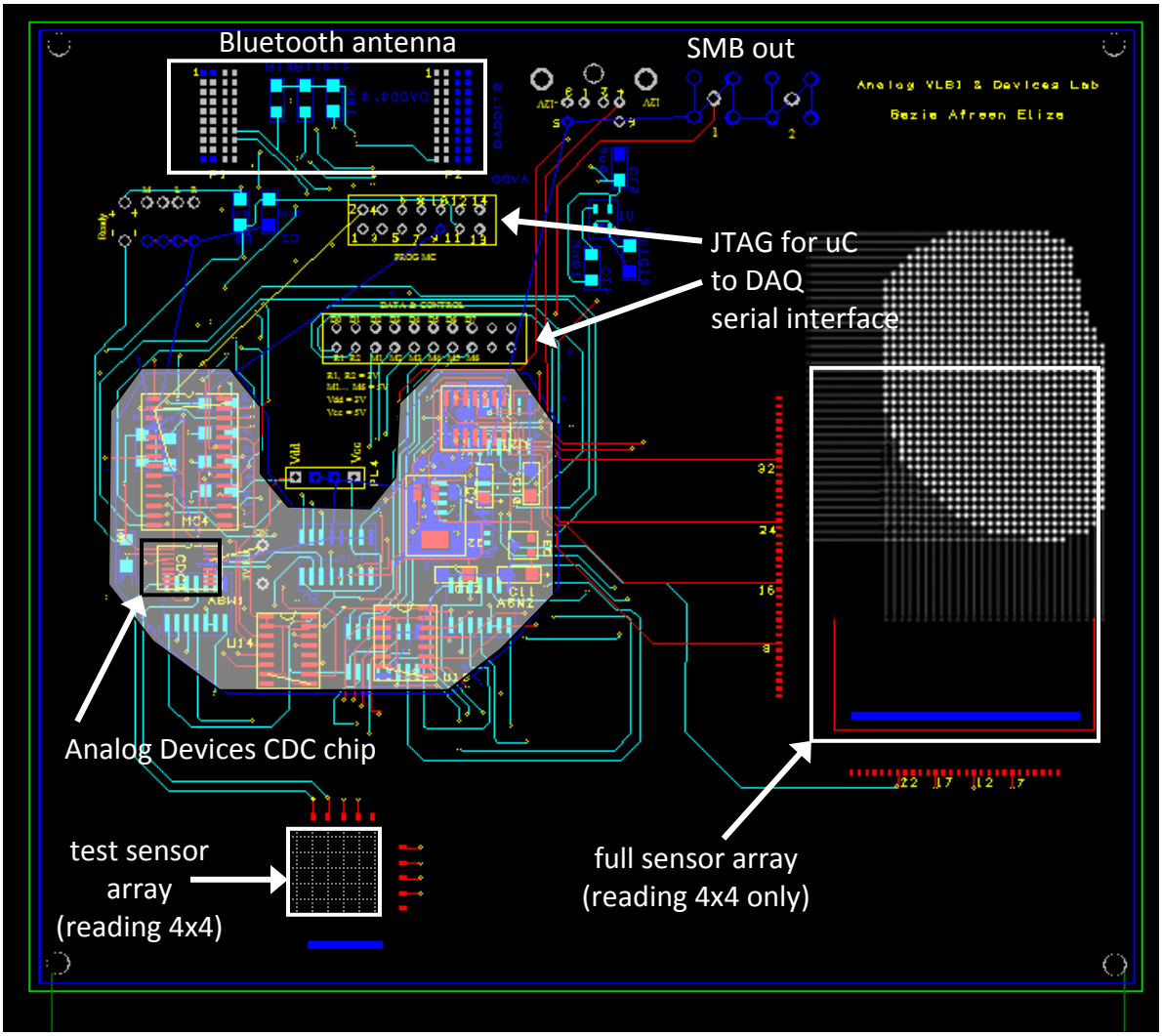

Figure 67. Second iteration PCB design layout for interfacing with Analog Devices CDC chip, showing provisional footprint with only connectors outside the main footprint for research purposes.

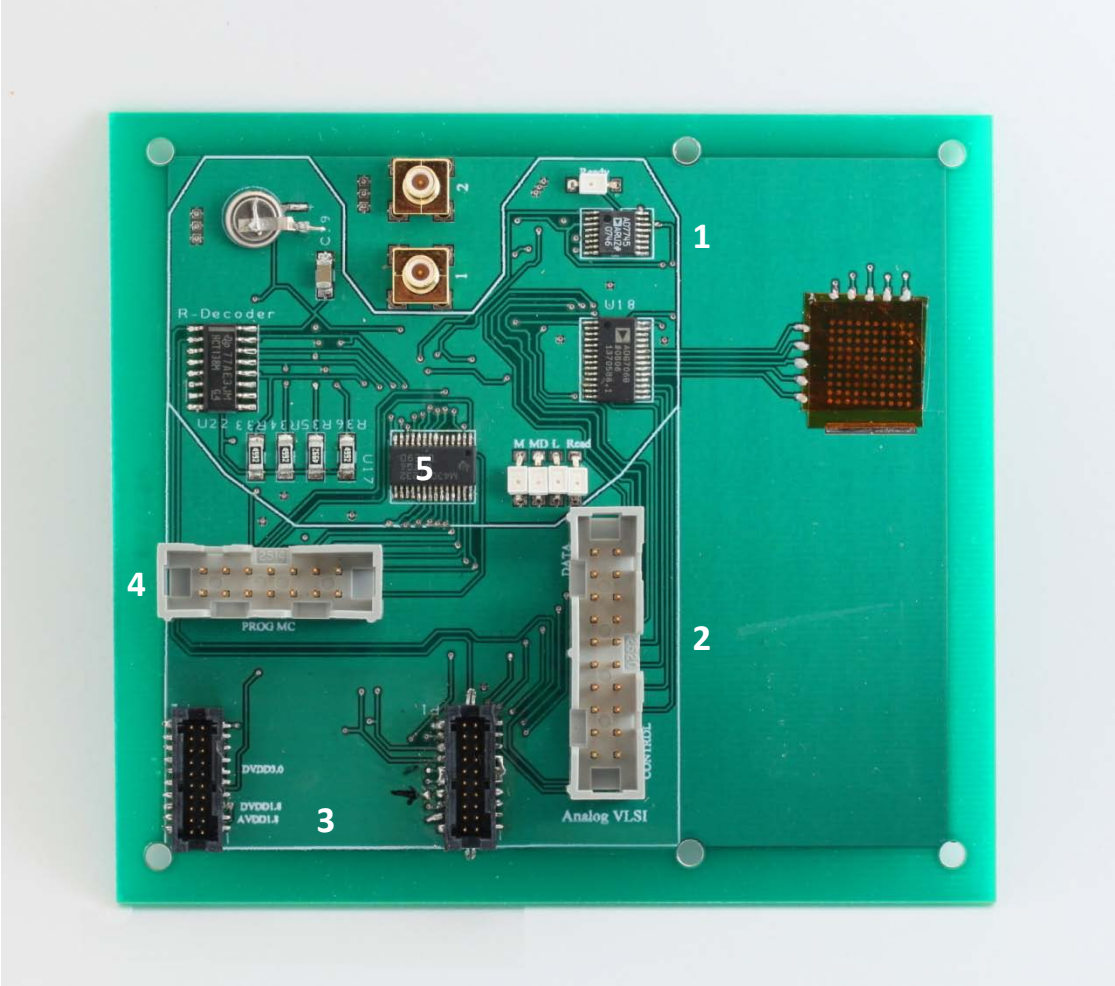

Figure 68. Third iteration test board retaining optional DAQ interface or CC2400 bluetooth output. Key: 1- CDC chip, 2- DAQ serial interface, 3-CC2400 connection, 4- JTAG for µC programming, 5- µC.

The 3rd and 4th iterations were used to validate the microcontroller to Bluetooth interface since the boards could also be used on the serial DAQ interface from iteration 1. For packaging purposes, a smaller Bluetooth antenna was needed, so the 5th iteration included complete removal of the wired serial interface and addition of the Roving Networks (Los Gatos, CA) RN-41 bluetooth transceiver with on-board chip antenna.

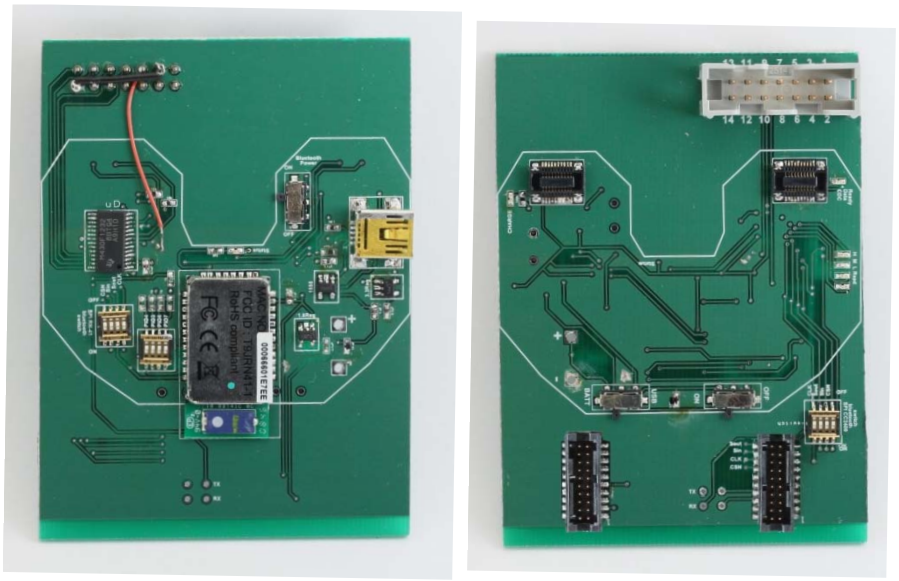

Figure 69. Final iteration of CDC readout board (bottom of stackable boards). This figure shows both sides of the bottom board, which uses a small, shielded Bluetooth module but still allows testing with the older TI CC2400 chip and large antenna.

Furthermore, the sensor array is moved to a separate, stackable board. This dramatically reduces the PCB trace capacitance prior to the analog signal reaching the CDC chip. The CDC chip is located on the back of the sensor board, so that digital signals are exchanged between board, avoiding the large parasitic capacitance effects of board-to-board connectors prior to CDC reading. Also, vias were eliminated in sensor traces

wherever possible to reduce parasitic effects on the way to the CDC chip. This board incorporates a second microcontroller responsible for MUX selection and the data sync between boards for sending of the digital sensor signal to the bottom board for Bluetooth readout. The microcontroller on the bottom board (Figure 69) is primarily responsible for sending the data to the Bluetooth chip. The Bluetooth hardware selection is controlled via manual switches on the board to choose between the RN-41 and the CC2400. The RN-41 also has manual configuration switches implemented for ease of settings changes for commonly used experimental settings. RN-41 data is available on the COM-port of any Bluetooth capable computer, and a mini-USB port has been added to the provisional ligament balancing tool as an easy optional power supply. The mini-USB can also be used for data-readout when the manual switch is set.

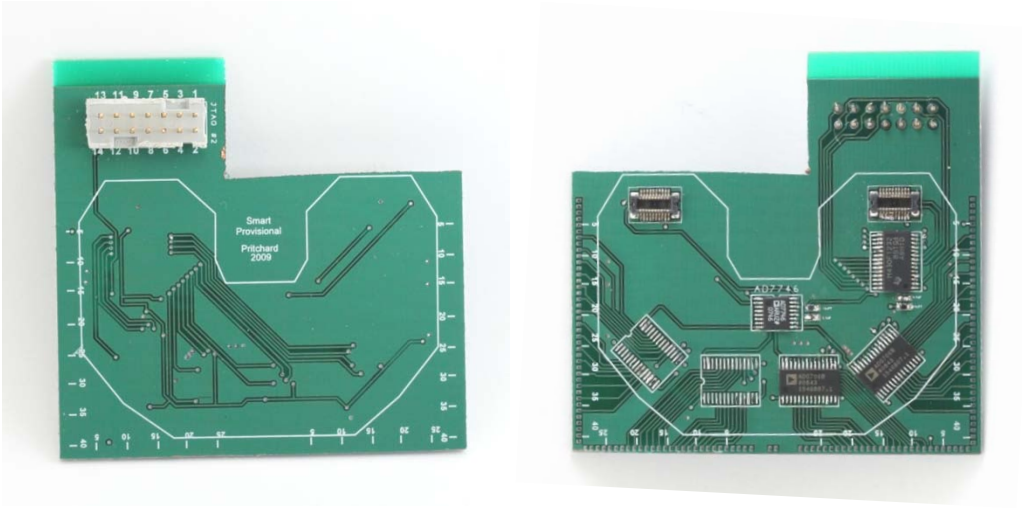

Figure 70. Iteration 4, top sensor board. Configured for unicondylar testing, but expandable to full condylar array. Left: top side ready for sensor mounting. Right: bottom side with MUX, CDC chip, and board-to-board connectors.

JTAG wired interfaces are maintained for both microcontrollers so that programs can be downloaded and uploaded as they are modified. Once the program demonstrates satisfactory performance, the JTAG portions of the board can be removed completely, creating room for posterior tissue space during ligament balancing. Likewise, the larger CC2400 bluetooth module connectors can be removed completely from the anterior side of the board to allow the device to fit the basic footprint of a provisional.

The final board prototype (Figure 71) fit the functional requirements set out in Section 2.1. As demonstrated by mechanical testing in Section 4.2.4 , the developed sensor array shows promise of putting convenient, quantitative data at the surgeon's fingertips.

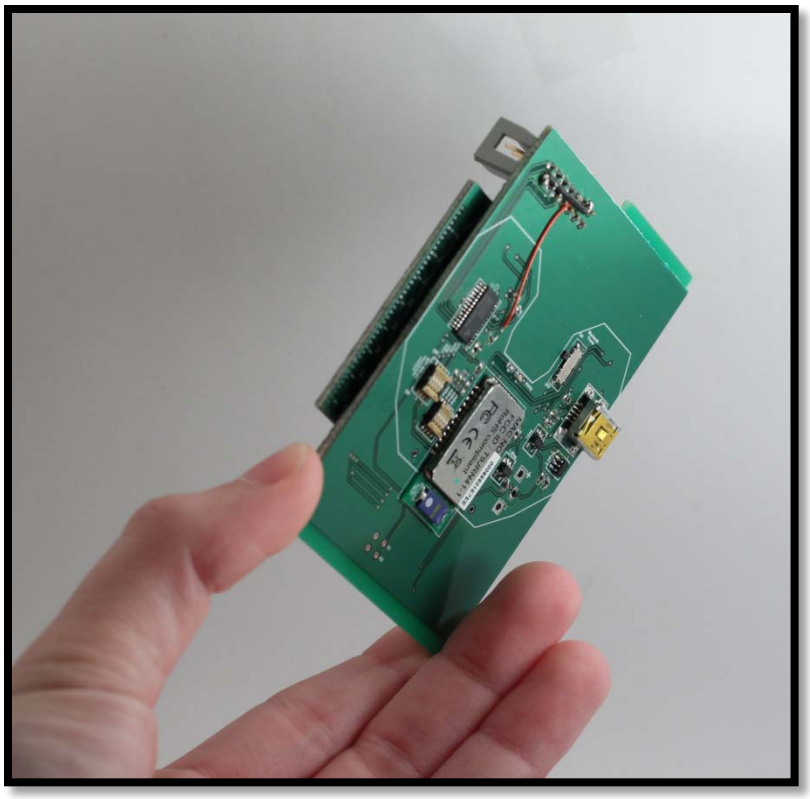

Figure 71. Final CDC readout boards, showing stacked configuration. View is from the bottom. Configuration ports for both µC remain intact, but are removable, further reducing the size of the device.

5.1.2 ASIC for Implant Use

A prototype circuit is designed on PCB to validate the circuit design before integration on a CMOS chip. The prototype board operates with a dual ±5 V supply. The board level prototype is interfaced with the capacitive pressure sensor and the corresponding DC outputs are monitored for a repeated loading profile. For calibration of the read-out circuit, surface mount capacitors of various known values are arranged

on a PCB to form a calibration board (Figure 72). The corresponding DC output from the prototype circuit is measured for each known capacitance. [45]

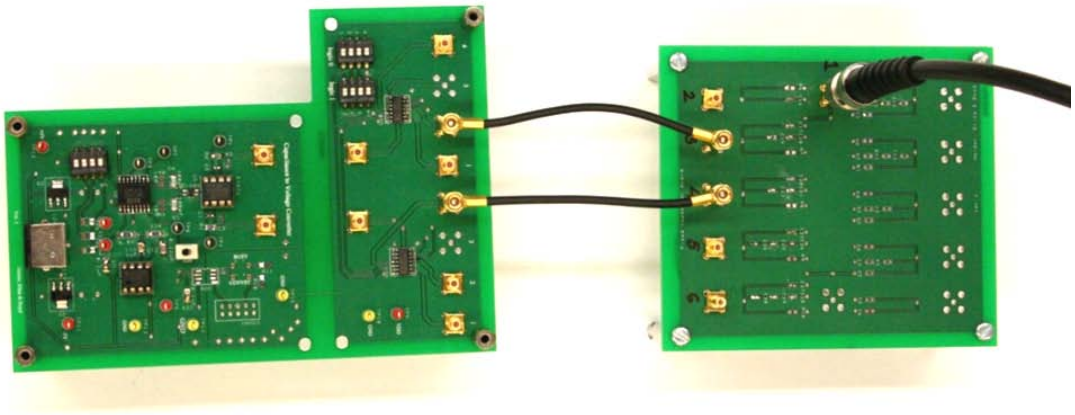

Figure 72. Prototype PCB for capacitance to voltage circuit (left) with calibration board (right).

The circuit design was simulated to predict noise performance as shown in Figure 73.

Figure 73. Noise Simulation of Capacitance to Voltage Circuit.

The performance with the calibration board showed promising results for the prototype capacitance to digital circuit, so it was also tested with our in-house custom capacitive pressure sensors undergoing various load levels (Figure 74). The linearity with applied load was also measured, as shown in Figure 75, for loading and unloading of a 5 pF nominal capacitor on silicon undergoing 100 lb loading.

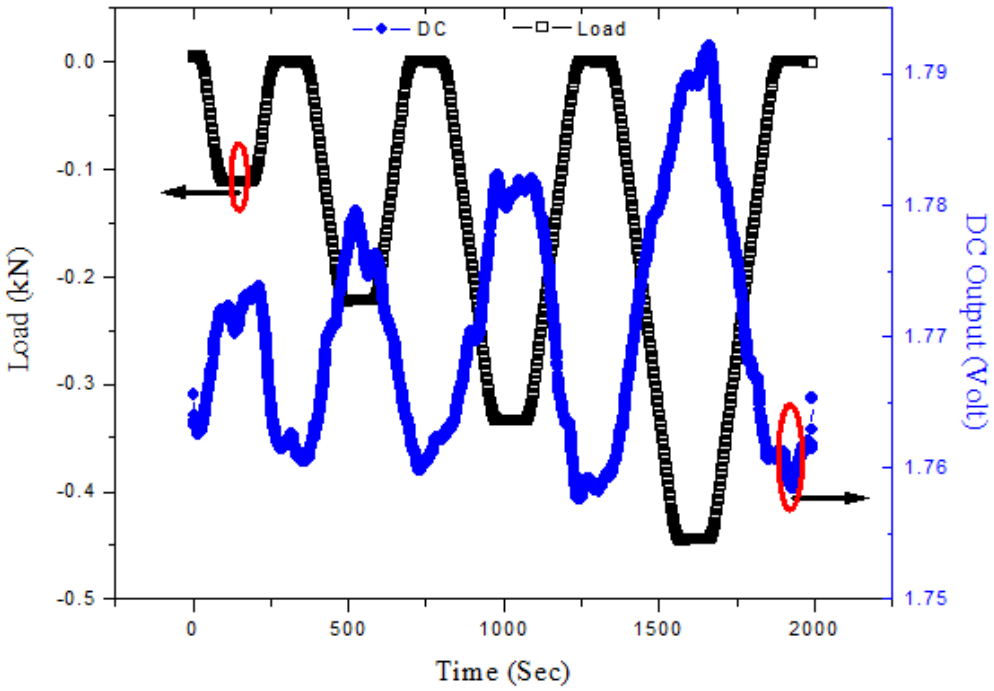

Figure 74. DC output from prototype circuit with custom capacitive sensor on silicon undergoing loading.

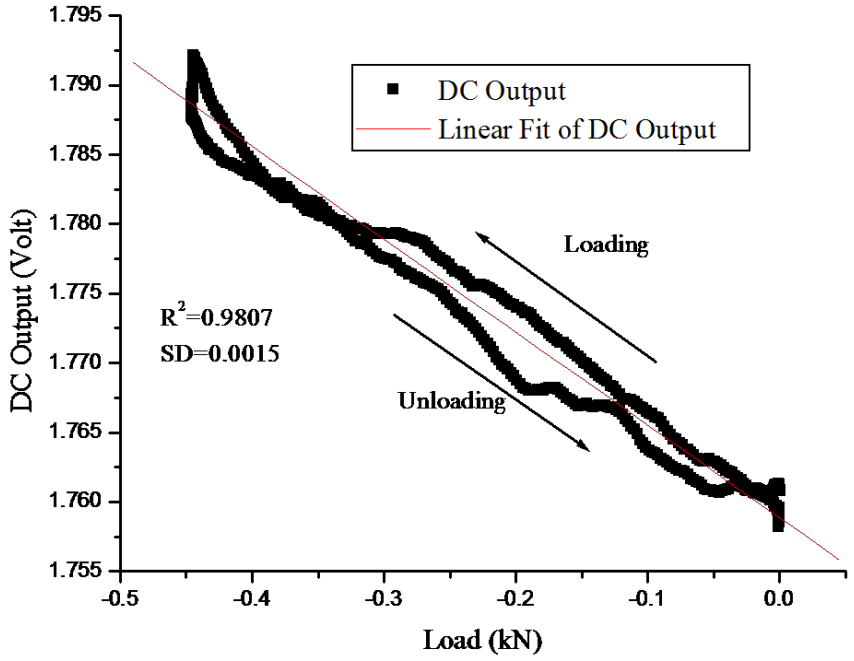

Figure 75. DC Linearity of the capacitance to voltage converter.

After validation with the prototype design, the circuit was designed, simulated and fabricated using TSMC 0.35 µm 2-poly 4-metal bulk CMOS process (fabrication by Mosis, Marina del Rey, CA). The circuit consumes only (1 mm X 1 mm) $1mm^2$ of area without pad.

An N-well shield was used to isolate the noisy substrate from the sensitive input signal tracks. Bottom plates of each capacitor are also shielded to eliminate any noise coupling from the substrate. Finally, a custom designed high gain Op-Amp and instrumentation amplifier were used to achieve high sensitivity of the circuit (Figure 77).

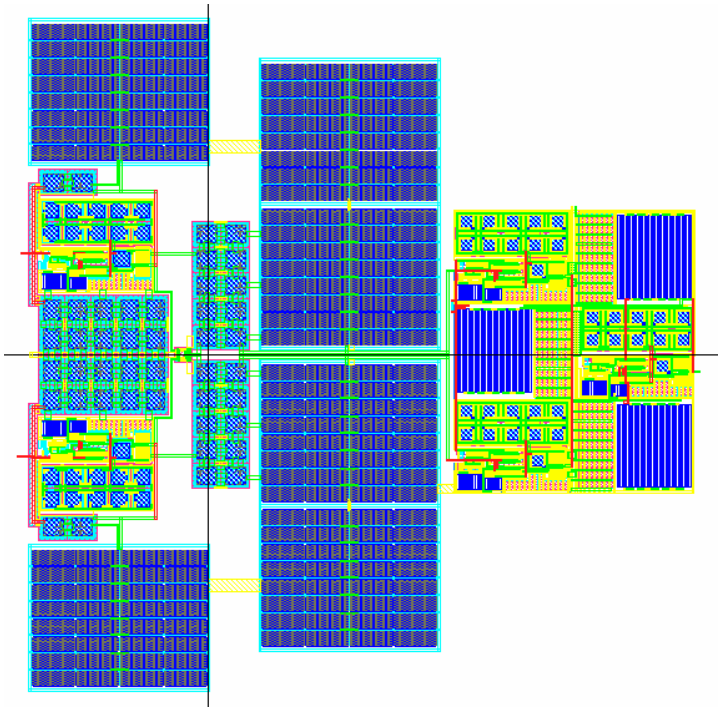

Figure 76. Entire layout of read-out circuit in the ASIC design.

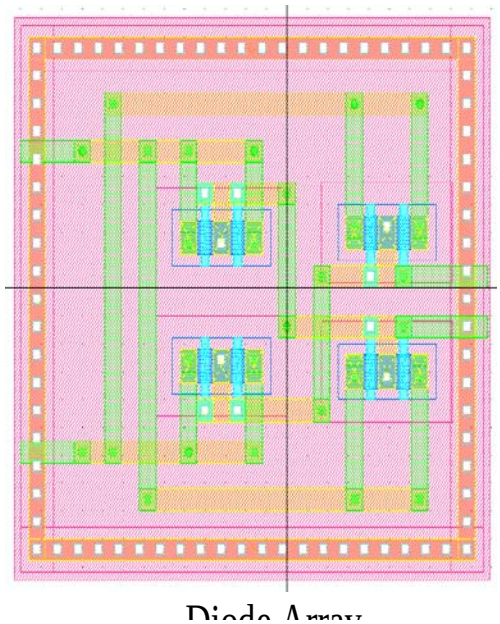

Figure 77. Various blocks of the ASIC design.

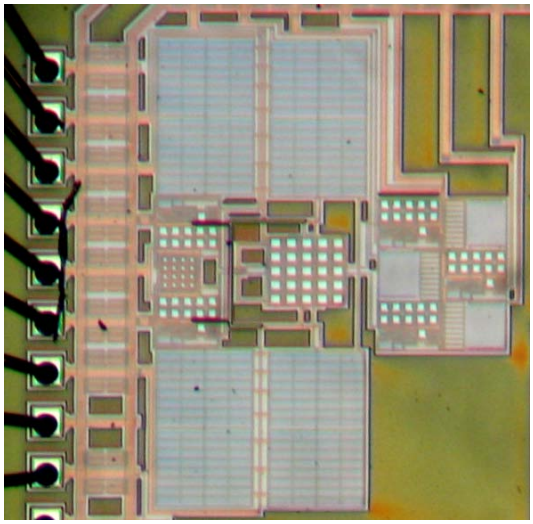

Figure 78. Microscopic view of ASIC after fabrication.

A small-footprint PCB was designed and debugged to utilize the ASIC chip. It was validated using a calibration board.

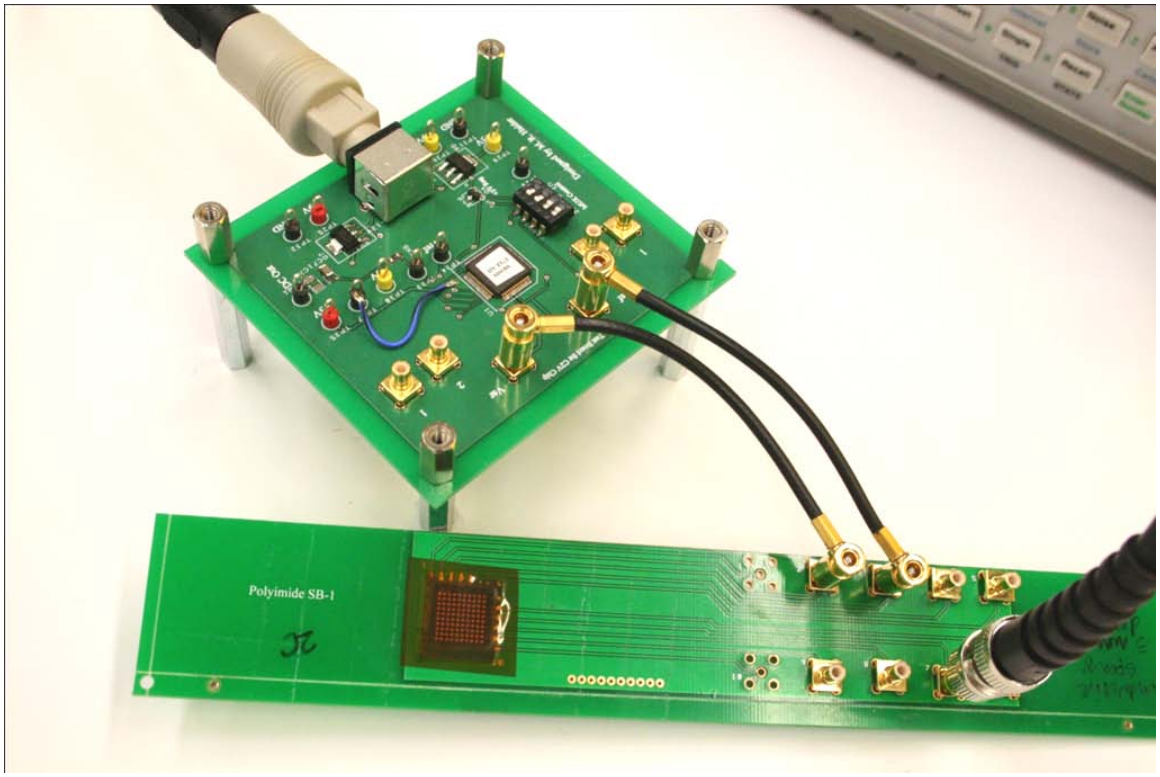

Figure 79. Testing setup for ASIC reading of flexible capacitive sensors.

The ASIC test board was tested with an Instron 5544 tabletop mechanical testing machine.

Figure 71 shows well-defined steps but readout resolution. Each step is a 5 lb load increase up to 50 lbs (253 kPa), with less machine overshoot during unloading. Sensors demonstrate full return to zero. Eight steps are taken during load/unload, although steps are not evenly spaced due to manual control of the Instron machine. Figure 81 shows a similar test where unloading was also stepped to examine hysteresis of the sensors. The timing of the steps is not completely consistent due to the manual control, but the sensor does fully return to zero after zero load.

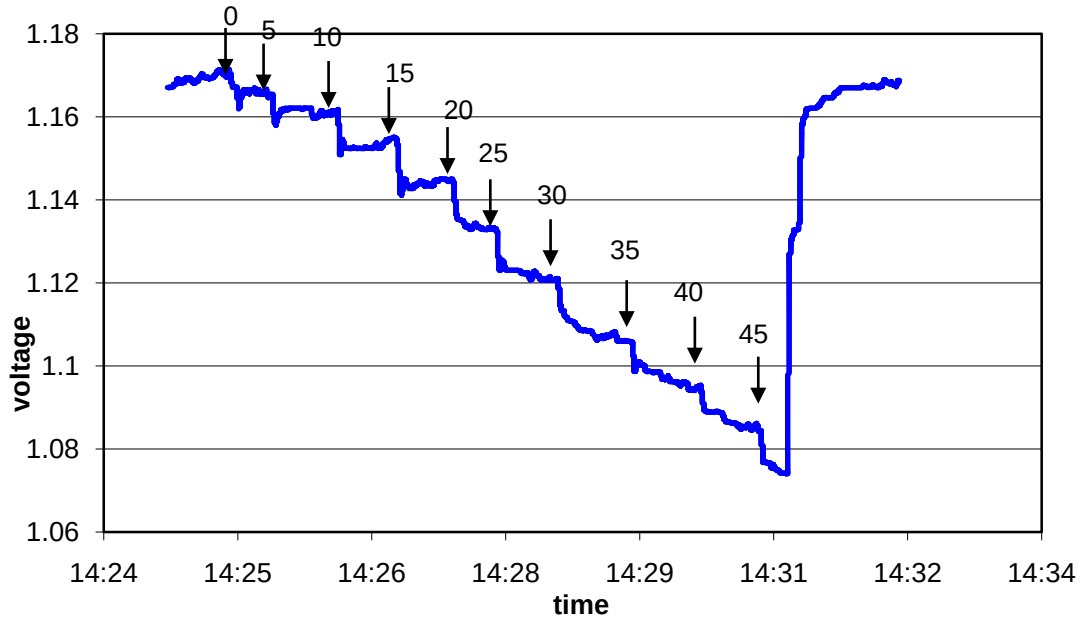

Figure 80. ASIC readout circuit with flexible capacitive sensors under loading. Plot shows moving average (100). Data rate is approximately 100 pts/sec. Note that the machine showed difficulty maintaining loads between 30-45 lbs. The Instron machine also accounts for the overshoot and undershoot seen between steps.

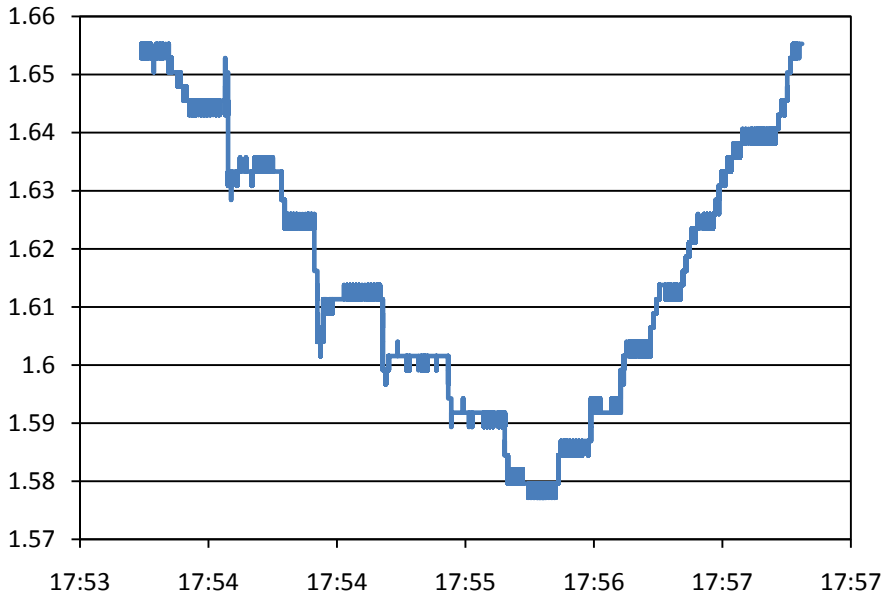

Figure 81. Load testing of flexible array with ASIC board.

5.2. Uncertainty Analysis of Testing Methods

5.2.1 Agilent 4285A Precision LCR meter

An Agilent 4285A Precision LCR meter was used to make measurements during mechanical testing of initial prototype designs. It uses an autobalacing bridge methods for 4 probe points, where current is applied through one pair of probes and voltage through a second pair of probes. The test signal frequency range can be manually set anywhere from 75 kHz to 30 MHz with 100 Hz resolution and an accuracy of 0.01%. The manual for this instrument states that its display has a resolution of 0.00001 pF – 999.999 µF. When using this instrument in experimental setup, may factors outside the LCR meter can significantly affect the accuracy of its readings, including cable length (3 ft cables were used), temperature (settling time was allowed by a 30 minute warm-up period for the LCR meter- all other testing apparatus remained at room temperature), and internally by LCR settings such as test device impedance, measurement frequency, and voltage. The measurement accuracy was calculated to be ±0.3% of the displayed value [62].

During testing, the calibration procedure for removing parasitic capacitances was used to subtract the base capacitance of the sensor such that the LCR meter reported the change in capacitance over the test instead of the actual capacitance value. This allowed operation of the instrument at resolutions intended for the measurement of smaller capacitance values. The LCR meter was carefully calibrated in the test fixture just prior to testing. Interfacing from a laptop computer to the instruments

microprocessor using HP-IB connections to processor the instrument reported capacitance values to the laptop with a resolution of 1×10^{-10} pF. The RMS error of the MTS load actuator was measured to be 1.21 N (0.27 pounds) during this evaluation which would result in an error of 6.11 kPa in the applied pressure.

Table 7. Error Propagation using LCR meter setup

Source	Error	Error Mitigation
Epoxy pad connection	unknown[6]	minimize epoxy, shielding
PCB trace	1.054 pF	shorten traces (capacitance to ground, tolerated)
mini SMB connector	unknown	shielded connector
coaxial cable and BNC connectors	negligible, unknown (calibrated out)	calibration within 1×10^{-10} pF
LCR meter	±0.3%[7]	warm-up and calibration
MTS load machine	1.21 N / 6.11 kPa[8]	warm-up and calibration

[6] See discussion and simulation in Section 2.4.

[7] [62] B. Evans III, *MEMS Capacitive Strain Sensing Elements for Integrated Total Knee Arthroplasty Prosthesis Monitoring*. Knoxville: University of Tennessee, 2007.

[8] [62] Ibid.

5.2.2 Custom Board Error Analysis

The custom board uses the Analog Devices7745 24-bit capacitance to digital converter. The chip accuracy is 0.004 pF with allowable 60 pF capacitance to ground. (Theoretically, capacitance to ground does not affect measurements at all, rather, parasisitic capacitance within the circuit does.) Output noise is 0.0606 aF RMS for the selected settings. The large connectors have been eliminated from the board design, reducing parasitic capacitance effects in the circuit compared to LCR meter testing.

Table 8. Error Propagation using AD chip custom board setup

Source	Error	Error Mitigation
Epoxy pad connection	unknown[9]	minimize epoxy, shielding
PCB trace	0.2108 pF	shorten traces (capacitance to ground, tolerated)
MUX[10]	<200 pF (on) 13 pF (off) capacitance to ground	[11]
AD 7745	0.004 pF (absolute) .032 pF (offset)	offset calibrated out at device start-up

[9] See discussion and simulation in Section 2.4.

[10] Analog Devices ADG706 16-to-1 multiplexer specifications sheet.

[11] These are spec sheet typical for 1 Mhz operation, actual frequency is much lower and should reduce these parasitic to ground effects.

MTS load machine	1.21 N / 6.11 kPa[12]	warm-up and calibration

Chapter 6. Future Directions

6.1. Plasma Experimental Explorations

Various topics to further explore the cause and effects of plasma-modification of UHMWPE surfaces include Fourier-Transform Infrared Spectroscopy (FTIR) or X-ray photoelectron spectroscopy (XPS) to measure surface functionalization after plasma treatment, exploration of the effects of atmospheric plasma in air (a combination of nitrogen and oxygen, with no need for expensive, slow vacuum pumps). Sterilization investigations; are the finished sensors arrays robust enough to withstand a type of sterilization, and as a separate topic, investigate whether commercial plasma sterilization machcines are capable of providing a level of surface treatment adequate to activate the surface of the polyethylene surface.

6.1.1 Cadaver and Clinical Trials

Cadaver and live patient clinical trials are a natural capstone to show the sensing array in use in its intended application. The expected intraoperative (e.g. passive)

[12] [62] B. Evans III, *MEMS Capacitive Strain Sensing Elements for Integrated Total Knee Arthroplasty Prosthesis Monitoring*. Knoxville: University of Tennessee, 2007.

compartmental pressures are not well established to date. Cadaver testing requires special consideration to mimic intraoperative live patient use. The flexion angle should be tracked in 3D space while the provisional records pressure data so that the pressure profiles correspond to a specific flexion angle. This can be achieved using any surgical navigation system independent of mode of operation (e.g. optical, electromagnetic, radiofrequency). A registration step for the femur and tibia is required with a method of bone tracking in order to locate the joint in 3D space during the entire range of motion.

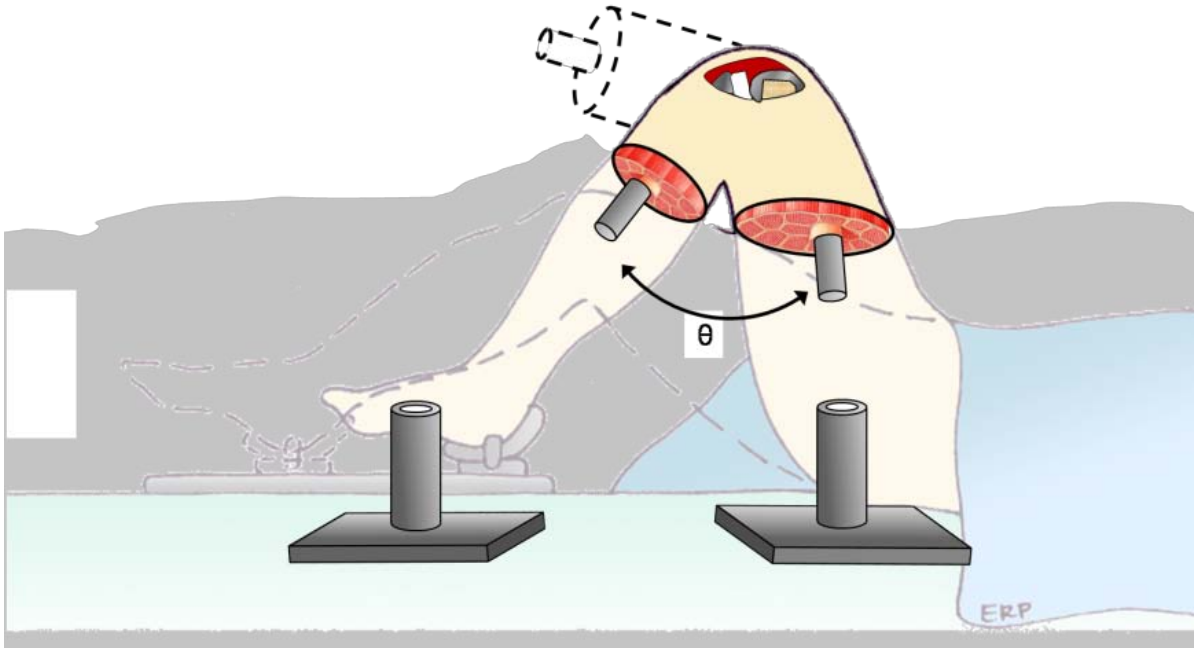

Figure 82. Design for cadaver experiment using an isolated knee, where flexion angle θ is measured while the sensing provisional records pressure profiles.

While cadaver trials can be useful for demonstration purposes, the benchtop laboratory tests outlined in this dissertation provide more than adequate justification to move to clinical trials directly. The device should be sealed completely in a biocompatible epoxy so that the electronics are not harmed and so that the patient is never in contact with the circuit itself. An epoxy such as EP30MED (Masterbond, Hackensack, NJ) will provide the protection needed.

Further possibilities for clinical studies include comparison of implant families or manufacturers, such as posterior-stabilized and posterior cruciate retaining or mobile bearing versus rigid. Furthermore, the effect of implant size as it pertains to the patient fit in the effect on contact area and pressure can be clinically evaluated and compared to kinematic contact area analyses. The sensors could also be configured to cover the cam-post in posterior stabilized designs to investigate cam engagement contact areas and forces present. Initially implemented as a provisional study, the real research value of investigating cam engagement would come from smart implants with real weight-bearing scenarios, but such a study remains in long-term plans.

6.2. Broader Uses and Implications

The technologies presented in this dissertation are applicable to a wide variety of biomedical and non-biomedical scenarios where a responsive, accurate pressure profile measurement is required. Minimal modification to the sensor design, materials, and layout can allow these applications to benefit from the use of flexible MEMS strain sensor arrays. Two are presented here are contact pressure mapping for biomechanics

and intracranial pressure measurement, although many more possibilities from robotic tactile skins to high resolution intraocular lense electrodes can be explored.

6.2.1 Contact for Mapping In-Shoe

Measurement of ground reaction forces during human activity has been become a pillar of clinical biomechanics. Knowledge about ground reaction forces aid in clinical diagnosis, treatment, and engineering design of orthotics, braces, and implants. In addition to magnitude of forces present, the location of those forces is also relevant to assess how the ground reaction forces are transferred to the weight-bearing limb during various activities. This section outlines a view of how the custom sensors developed as a part of this dissertation could be used to implement a novel pressure-sensing in-shoe measurement system.

Noting differences in the main phases of gait (Figure 83) can aid in diagnosis of underlying ankle, knee, and hip disorders. Schutte, et al, used principal component analysis to identify 16 characteristics of gait that can be used to indicate clinically-relevant abnormalities [63].

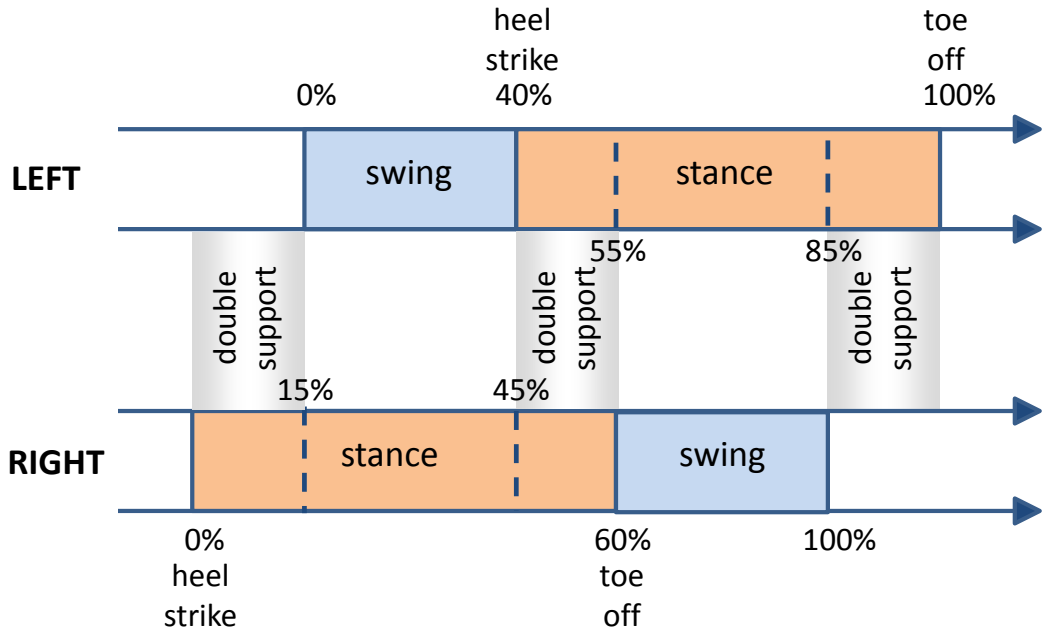

Figure 83. Normal gait pattern.

Force measurement greatly increases the discriminatory power of plantar measurements to identify atypical and symptomatic patterns to correlate with joint diagnoses. Force measurements to of ground reaction forces began using force plates, where a load cell is located between two metal plates. All three axes are of interest so that horizontal forces during contact with the ground can also give an idea of how loads are transferred to the foot during stance phase of gait or other activities. Force plates maintain the ability to measure all three components of the ground reaction force (in the x, y, and z directions). This also can be interpreted as a measure of shear or frictional forces present between the foot at the ground. Each principal axis shows distinctly different but repeatable patterns for various activities, as shown in Figure 85.

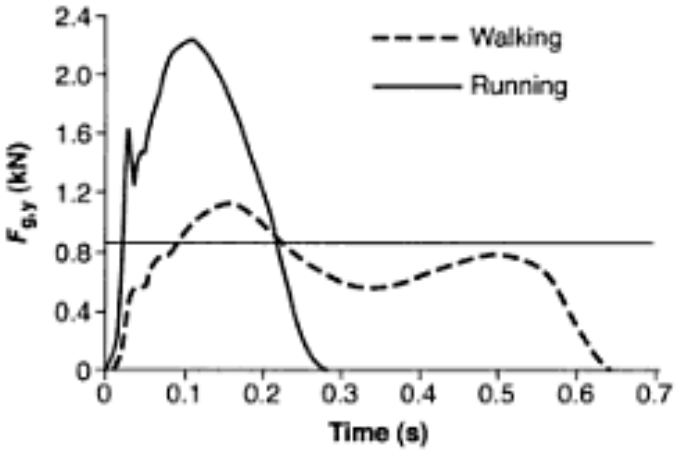

Figure 84. Vertical Ground Reaction forces during walking and running. Graph starts at heel strike and ends at toe off. [64]

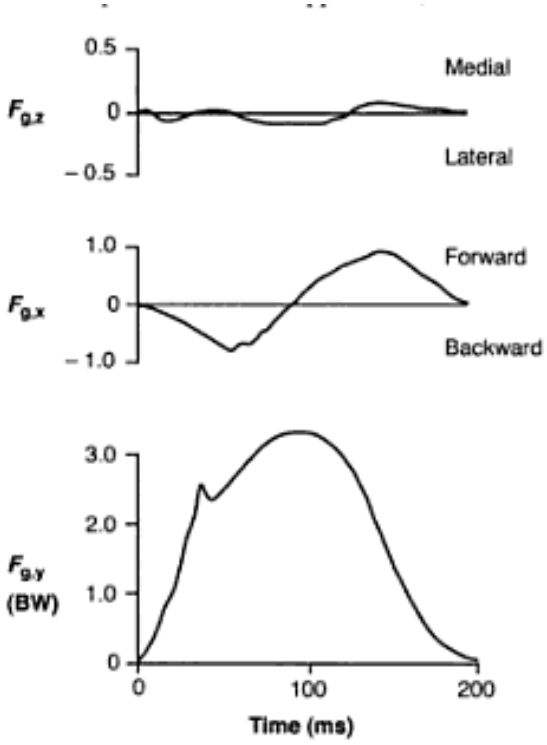

Figure 85. Generalized 3-axis ground reaction forces during support phase of gait. [65]

Flexible sensor arrays have added to the experimental capability of plantar pressure measurement by allowing higher spatial resolution measurements and real-time data. Initial research systems provided a few pressure point per foot, but soon technology expanded the number of available datapoints. Ground pressure mats by Xsensor, Inc, provide axial pressure profiles, and in-shoe systems by Novel and Tekscan provide in-shoe measurement systems. The core technologies behind these systems are covered in greater detail in Section 1.2.2 , and spatial resolution is typically a few mm.

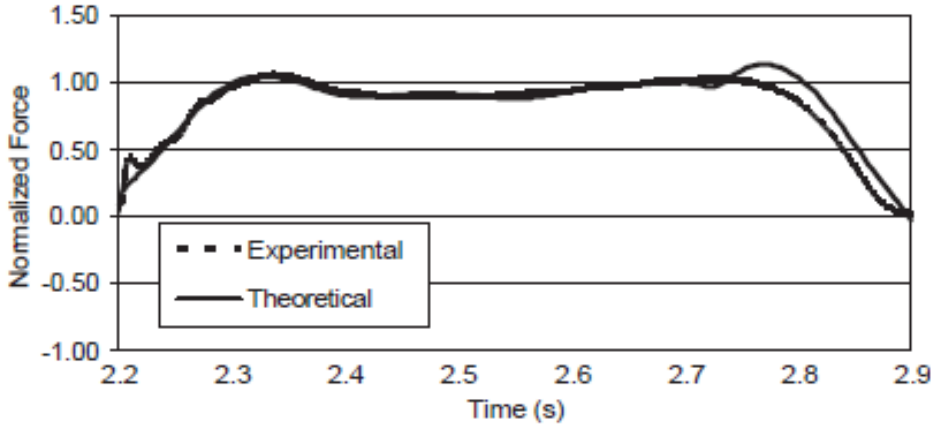

Figure 86. Ground Reaction Forces during gait. [64]

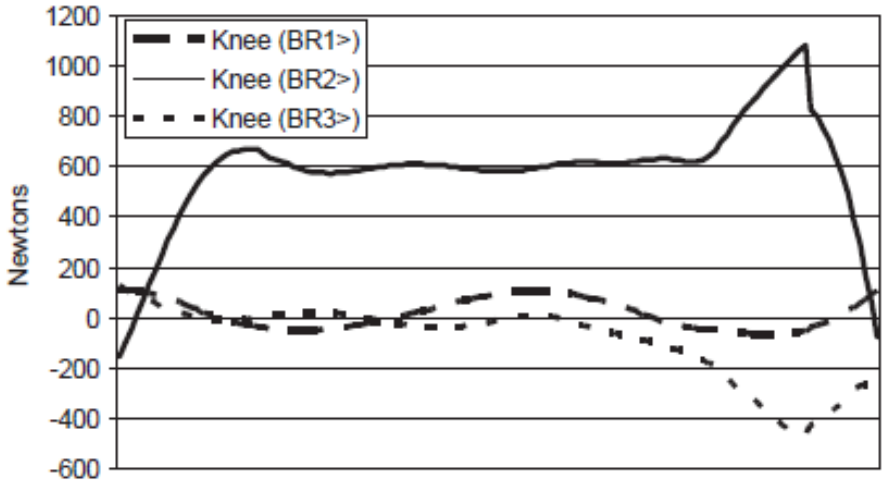

Figure 87. Resultant forces within the knee. [64]

Knee kinematics are influenced by foot kinematics and kinetics, as well as vice versa. Understanding normal interaction between the ground, the foot, and the knee can lead to a better understanding of changes that occur with knee osteoarthritis. The way the foot contacts the ground is both an indicator of biomechanical issues farther up the limb, and can also serve as a means of modification of the kinematics and kinetics of the knee and hip.

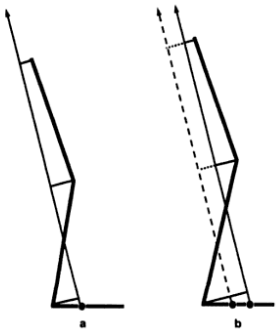

Figure 88. Illustration of how the center of pressure on the foot is modified by a person with a longer tibia so that knee moments are similar for both the person with the tall tibia and the one with the short tibia. [66]

Researchers report pressures of 200-500 kPa present in the shoe during running depending on the type of shoe sole, running surface, and running style [67], [68].

A system designed for surgical instrumentation has been optimized to measure pressures less than 2 MPa. This covers the dynamic range of pressures present within the shoe for various common activities.

With a parylene dielectric thickness of 1.5 μm and a desired nominal capacitance of 5 pF, the radius of the required circular electrode is 295 μm. Because the capacitance is inversely proportional to the dielectric thickness, the change in capacitance is expected to be highly non-linear for large deformations, as shown in Figure 17.

However, such large deformations are not realistic for most dielectric materials. For the case of a parylene dielectric described above, an applied axial stress of 2 MPa results in a strain of 725 microstrain, which corresponds to a dielectric deformation of 1.09 nm.

The sensor may be considered “solid state”, as there are no moving parts (e.g. diaphragms), and the pressure ranges and output capacitance can be controlled by the choice of dielectric medium. Stiffer dielectrics enable higher pressure operating ranges, while softer dielectrics enhance resolution of lower pressure ranges. For a fixed plate dimension, the dielectric constant of the material determines the nominal capacitance and influences the change in capacitance for a given load, making higher dielectric constant materials more desirable.

6.2.2 Intracranial Pressure (ICP) Monitoring

Existing ICP monitors require external connections (i.e. coaxial cables), and are quite large in size, protruding from the skull after a hole is drilled in the cranium for insertion. Thus they are frequently disrupted or dislodged, resulting in infection, replacement, and device malfunction. Ventricular catheters are prone to occlusion and to life-threatening infections if contaminated. Even monitoring devices designed to work without direct fluid coupling, such as fiberoptic and implanted strain gauge transducers cannot be recalibrated once inserted and thus suffer from significant signal drift. Their utility is limited over time, and the devices often require replacement after 5 days for longer duration monitoring needs. Noninvasive monitors, which rely on acoustic, ultrasonic or intraocular pressure readings, have not proven to be reliable [69-71]. Hence, none of the devices presently available is suitable for long-term ICP monitoring, and even acute cases would benefit from more accurate and less invasive monitors to lower overall treatment costs.

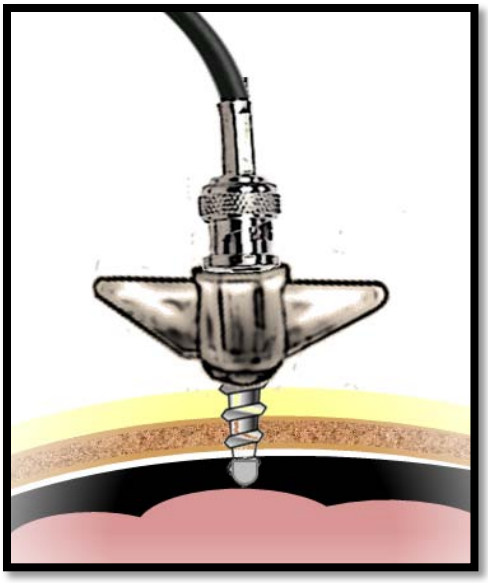

Figure 89. Typical wired ICP monitor

Various approaches have been developed to implement ICP estimation using the invasive techniques. These include lumbar puncture, intra-ventricular catheter, sub-arachnoid screw (Richmond bolt), fiber optic transducer tip catheters, and acoustic apparati. The United States Patent and Trademark Office database includes over 80 patents issued since 1975 for devices which claim to measure ICP to address the clinical need and circumvent problems with existing techniques. These devices utilize various measurement methods: radio frequency tuned circuits, vibrating mechanical components, moving magnetic parts and optical components. Devices with large magnetic or inductive elements are not MRI compatible. The performance of optical components varies widely with absorption and scattering coefficients of the heterogeneous composition of the tissues. These coefficients are subjective depending on a number of factors including pigmentation of the scalp, oxygenation levels, rate of thermal diffusion, etc.

Existing techniques to determine ICP are wired and involve penetrating the skull with a risk of exposure to the external environment throughout the time the device is in place. However, the duration of ICP monitoring is severely limited by safety concerns. These monitors require external connections, which are frequently disrupted or dislodged, and carry an increased risk of life-threatening infection if contaminated [72]. Thus their utility is limited over time, and the devices often require replacement for long-term use. Measurement accuracy is also a concern, as monitoring devices designed to work without direct fluid coupling, such as fiberoptic and implanted strain gauge transducers cannot be recalibrated once inserted and thus suffer from significant signal drift [73]. As mentioned previously, noninvasive monitors, which rely on acoustic, ultrasonic or intraocular pressure readings, have not proven to be reliable [69-71]. Hence, none of the devices presently available is suitable for long-term ICP monitoring.

At present, the most common method used for ICP monitoring in the United States is a fiber optic based transducer tipped catheter developed at Camino Laboratories (San Diego, CA). However, Camino catheters show significant drift and sub-par performance [74], These catheters need to be replaced after 5 days for longer duration monitoring needs. The fiber optic catheters with a pressure transducer tip can be inserted in intra-ventricular, sub-arachnoid, or parenchymal sites, giving a more realistic ICP estimation than other methods. However, these systems are prone to becoming malpositioned. Disposable fiber optic based catheters are available, but prove to be invasive and expensive. A second commercial device with widespread clinical use

is the Codman Microsensor (Johnson & Johnson), which utilizes strain gauges on a catheter. Multiple studies show it is common to find significant discrepencies of 10 mmHg or more when comparing the Camino and Codman devices [74].

Overall, complications involved with the above mentioned techniques include infection, hemorrhage, tissue damage, malfunction, misplacement, obstruction and stroke. These are unlikely to lead to increased patient morbidity because the devices are replaced. However, replacement of the ICP monitor and treatment of the complication incur pain and added costs compared with proper device design. With such complications, high cost, and inaccurate readings, current systems are woefully inadequate.

The goal of this research is to develop a novel permanently implantable, wireless intracranial pressure monitoring device that is less invasive and lower-cost than commercially available systems. This proposal outlines the design, in vitro testing, and in vivo testing in an animal study to establish a wireless ICP device for deployment in low-resource settings.

Major challenges in accuracy, cost, and clinical complications exist in current systems that utilize wires through the skull. Through multidisciplinary collaboration, a wireless, low-cost implantable ICP monitor will be developed and tested in vivo in an animal model to address major challenges to reduce cost, reduce complications, and improve accuracy. A wireless, implantable, low-cost device has significant potential to decrease incidence of permanent brain damage due to elevated ICP for acute use in

hospital intensive care, trauma, and neurosurgery (Figure 90). The device will also enable chronic monitoring of patients with recurring symptoms or severe disease progression without requiring a hospital setting. The device is relevant to general hospitals and low-resource settings, and the convenience and decreased clinical complications promise lower treatment costs for these patient populations while improving clinical outcomes.

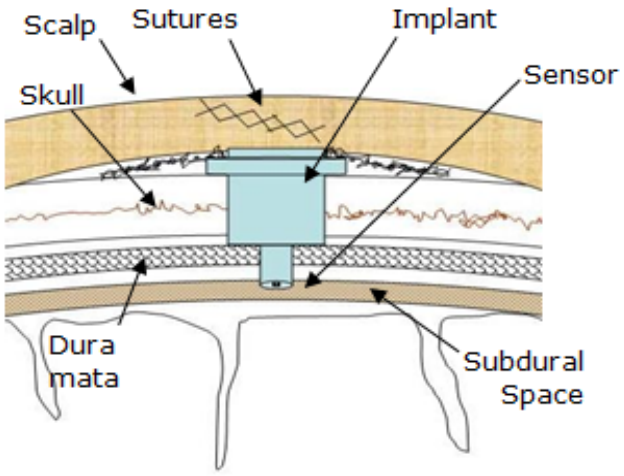

Figure 90. Conceptual design of a wireless ICP monitor.

Wireless monitoring of ICP by a completely implantable device without an exclusive neurosurgical procedure is a novel approach. The patient already requires a neurological surgery, so a small device can be implanted at the time of the surgery and retained thereafter for subsequent ICP monitoring, thus reducing the invasiveness and cost of the procedure. In cases where a surgery is not scheduled for other treatment, a small burr hole can be used to implant the device, and the benefit of an implant reduces the chance of complication and replacement. Recent advances in MEMS sensors and the affordability of RF-CMOS submicron processing suggest a wireless, Bio-MEMS-based, ICP monitoring device as a viable solution that can be implemented with low cost and employed in critical care settings as well as non-hospital settings where long-term monitoring is required.

Chapter 7. Conclusion

Biomedical applications requiring high sensitivity in low pressure ranges can benefit greatly from the developed capacitive MEMS pressure sensing array. The biocompatibility and flexibility of the array also allow it to be used in a variety of applications, including joint arthroplasty, surgical navigation, gait analysis, tactile robotics, and any contact-pressure measurement surface, especially between rigid bodies with curved surfaces. The two-dimensional pressure profiling is useful in determining contact area and inference of stress concentrations at the contact interface.

The goal of this dissertation is to develop conformable real-time capacitive pressure sensor technology suitable for implementation in a surgical ligament balancing tool. The sensors outlined here provide improved spatial resolution as well as improved accuracy and pressure resolution over flexible sensor solutions that are commercially available or presented in the literature today. This presents a valuable tool for quantitative surgical guidance for ligament balancing in total knee arthroplasty, as a stand-alone tool or as part of a surgical navigation suite. The technology presented facilitates static pressure measurement such as a surgical spacer block for flexion and extension and facilitates dynamic pressure measurement throughout the range of motion when implemented on the surface of a provisional component.

Biocompatibility is maintained to leave open the possibility of smart implants in the future. Biocompatible and fabrication processes have been developed to maintain standard biomaterials if the sensors should be migrated to a smart implant platform without degradation of sensor performance. The ultra-high molecular weight polyethylene (UHMWPE) surface characterization presented here has not yet been undertaken by others in the field of research, establishing a basis for future exploration of low-surface energy MEMS devices with micron-level resolution for electrode patterning, especially where ultra-high molecular weights may be desirable.

References

[1] "Osteoarthritis," National Institute of Arthritis and Musculoskeletal and Skin Diseases2006.

[2] V. Pavone*, et al.*, "Total Condylar Knee Arthroplasty: A Long-Term Followup," *Clinical orthopaedics and related research,* vol. 368, pp. 18-25, 2002.

[3] J. Rodriguez*, et al.*, "Total Condylar Knee Replacement A 20-Year Followup Study," *Clinical orthopaedics and related research,* vol. 388, pp. 10-17, 2001.

[4] P. Sharkey, "Why are total knee arthroplasties failing today?," *Clinical orthopaedics and related research,* vol. 404, pp. 7-13, 2002.

[5] K. Bozic and H. Rubash, "Modes of Failure in Revision Hip and Knee Replacement," *Center for Disease Control, National Center for Health Statistics,* 2004.

[6] F. Orozco, "Why Are Knee Replacements Failing Today?," in *American Academy of Orthopaedic Surgeons 69th Annual Meeting*, 2002.

[7] K. Mulhall*, et al.*, "Current etiologies and modes of failure in total knee arthroplasty revision," *Clinical orthopaedics and related research,* vol. 446, pp. 45-50, 2006.

[8] J. N. Insall*, et al.*, "Correlation Between Condylar Lift-Off and Femoral Component

Alignment," *Clinical Orthopaedics,* vol. 403, 2002.

[9] D. MacIntosh, "Hemiarthroplasty of the knee using a space-occupying prosthesis for painful varus and valgus deformities," *J Bone Joint Surg Am,* vol. 40, p. 1431, 1958.

[10] R. Robinson, "The early innovators of today's resurfacing condylar knees," *J Arthroplasty,* vol. 20, pp. 2-26, 2005.

[11] R. Booth*, et al.*, "Instrumentation for Use in Orthopaedic Surgery," USA Patent 5688280, 1997.

[12] H. Asano*, et al.*, "Soft-Tissue Tension Total Knee Arthroplasty," *Journal of Arthroplasty,* vol. 19, pp. 558-561, 2004.

[13] A. Wymenga*, et al.*, "Posterior Cruciate Ligament Balancing in Total Knee Arthroplasty with a Dynamic PCL Spacer," in *Total Knee Arthroplasty*, J. Bellemans, Ed., ed Berlin: Springer, 2005.

[14] D. Viskontas*, et al.*, "Computer-Assisted Gap Equalization in Total Knee Arthoplasty," *Journal of Arthroplasty,* vol. 22, pp. 334-342, 2007.

[15] I. Zimmer. (1997, *Variable Soft Tissue Alignment Tensor (V-STAT)*.

[16] (2008, 8/29). *Prescale Measurement Film*. Available: http://www.fujifilm.com/products/prescale/index.html

[17] J. Wu*, et al.*, "A method for dynamically measuring the Soft Tissue Balance in the Total Knee Replacement," in *World Congress on Medical Physics and Biomedical Engineering 2006*, ed, 2007, pp. 723-727.

[18] M. Suzuki*, et al.*, "Dynamic Soft Tissue Balancing Sensor for Total Knee Arthroplasty," in *International Society for Technology in Arthroplasty*, Paris, France, 2007.

[19] A. Wallace*, et al.*, "Intraoperative assessment of tibiofemoral contact stresses in total knee arthroplasty.," *The Journal of arthroplasty,* vol. 13, pp. 923-927, 1998/12// 1998.

[20] R. Wasielewski*, et al.*, "An intraoperative pressure-measuring device used in total knee arthroplasties and its kinematics correlations.," *Clinical orthopaedics and related research,* pp. 171-178, 2004/10// 2004.

[21] M. Harris*, et al.*, "An Improved Method for Measuring Tibiofemoral Contact Areas in Total Knee Arthroplasty: A Comparison of K-Scan Sensor and Fuji Film," *Journal of Biomechanics,* vol. 32, pp. 951-958, 1999.

[22] Synvasive. (2007, *Flexion-Gap and Ligament Balancing Made Easy, Accurate and Repeatable: eLIBRA Dynamic Knee Balancing System*. Available: http://www.synvasive.com/resources/LIBRA-eLIBRA-Product-Brochure.pdf

[23] N. Rydell, "A new apparatus for the measurement of the compression between two bony surfaces and a construction for compression in fractures of the femoral neck. A preliminary report.," *Acta orthopaedica Scandinavica,* vol. 31, pp. 1-17, 1961/// 1961.

[24] N. Rydell, "Forces acting on the femoral head-prosthesis. A study on strain gauge supplied prostheses in living persons.," *Acta orthopaedica Scandinavica,* vol. 37, 1966/// 1966.

[25] T. English and M. Kilvington, "In vivo records of hip loads using a femoral implant with telemetric output (a preliminary report)." *Journal of biomedical engineering,* vol. 1, pp. 111-115, 1979/04// 1979.

[26] W. Hodge*, et al.*, "Contact pressures in the human hip joint measured in vivo.," *Proceedings of the National Academy of Sciences of the United States of America,* vol. 83, pp. 2879-2883, 1986/05// 1986.

[27] W. Hodge*, et al.*, "Contact pressures from an instrumented hip endoprosthesis," *J Bone Joint Surg Am,* vol. 71, pp. 1378-1386, 1989/10/01/ 1989.

[28] D. Davy*, et al.*, "Telemetric force measurements across the hip after total arthroplasty," *J Bone Joint Surg Am,* vol. 70, pp. 45-50, 1988/01/01/ 1988.

[29] G. Bergmann*, et al.*, "Hip joint loading during walking and running, measured in two patients.," *Journal of biomechanics,* vol. 26, pp. 969-990, 1993/08// 1993.

[30] G. Bergmann*, et al.*, "Design and Calibration of Load Sensing Orthopaedic Implants," *Journal of Biomechanical Engineering,* vol. 130, pp. 2-9, 2008.

[31] C. Ashruf, "Thin flexible pressure sensors," *Sensor Review,* pp. 322-327, 2002/// 2002.

[32] *Tekscan*. Available: www.tekscan.com

[33] H. Hsiao*, et al.*, "Accuracy and precision of two in-shoe pressure measurement systems.," *Ergonomics,* vol. 45, pp. 537-555, 2002/06/20/ 2002.

[34] E.-S. Hwang*, et al.*, "Flexible polysilicon sensor array modules using "etch-release" packaging scheme," *Micromechanics section of Sensors and Actuators, based on contributions revised from the Technical Digest of the 16th IEEE International conference on Micro Electro mechanical Systems (MEMS 2003) Sensors and Actuators A: Physical,* vol. 111, pp. 135-141, 2004/03/01/ 2004.

[35] *XSensor Technology Corporation*. Available: www.xsensor.com

[36] *Novel*. Available: www.novel.de

[37] *Pressure Profile Systems*. Available: www.pressureprofile.com

[38] C. Hierold*, et al.*, "Implantable low power integrated pressure sensor system for minimal invasive telemetric patient monitoring," in *Micro Electro Mechanical Systems, 1998. MEMS 98. Proceedings., The Eleventh Annual International Workshop on*, 1998, pp. 568-573.

[39] C. Hierold*, et al.*, "Low power integrated pressure sensor system for medical applications," *Sensors and Actuators A: Physical,* vol. 73, pp. 58-67, 1999/03/09/ 1999.

[40] M. Akiyama*, et al.*, "Flexible piezoelectric pressure sensors using oriented aluminum nitride thin films prepared on polyethylene terephthalate films," *Journal of Applied Physics,* vol. 100, 2006/// 2006.

[41] D.-H. Kim*, et al.*, "Dissolvable films of silk fibroin for ultrathin conformal bio-integrated electronics," *Nat Mater,* vol. advance online publication, 2010.

[42] J. Daintith, *Biographical Encyclopedia of Scientists*: CRC Press, 1994.

[43] B. N. Taylor and P. J. Moore, "NIST Reference on Constants, Units, and Uncertainty," National Institute of Standards and Technology2003.

[44] P. Rousche*, et al.*, "Flexible polyimide-based intracortical electrode arrays with bioactive capability," *IEEE Transaction on Biomedical Engineering,* vol. 48, pp. 361-371, 2001.

[45] M. Haider. (2008). *System-on-Package Low-Power Telemetry and Signal Conditioning unit for Biomedical Applications*.

[46] D. F. Williams, *Williams Dictionary of Biomaterials*. Liverpool, U.K.: Liverpool University Press, 1999.

[47] G. Bergmann*, et al.*, "Hip joint loading during walking and running, measured in two patients," *J Biomech,* vol. 26, pp. 969-90, Aug 1993.

[48] L. Hsu*, et al.*, "Characterization of Parylene-C film as an encapsulation material for neural interface devices," presented at the Third International Conference on Multi-Material Micro Manufacture, Borovets, Bulgaria, 2007.

[49] H. K. Yasuda, *Plasma Polymerization and Plasma Interactions with Polymeric Materials*: John Wiley and Sons, 1990.

[50] K. Mittal, Ed., *Contact Angle, Wettibility, and Adhesion*. Utrect, Netherlands: VSP, 1993, p.^pp. Pages.

[51] V. Mangipudi and M. Tirell, "Direct Measurement of the Surface Energy of Corona-Treated Polyethylene Using the Surface Forces Apparatus," *Langmuir,* vol. 11, pp. 19-23, 1996.

[52] S. O'Kell*, et al.*, "Effects of low-power plasma treatment on polyethylene surfaces," *Surface and Interface Analysis,* vol. 23, pp. 319-327, 1995.

[53] K. Mittal, *Adhesion Measurement of Films and Coatings*. Utrecht, The Netherlands: VSP BV, 1992.

[54] B. Evans*, et al.*, "Biocompatible MEMS Electrode Array for Determination of Three-Dimensional Strain," in *Engineering in Medicine and Biology Society, 2006. EMBS '06. 28th Annual International Conference of the IEEE*, 2006, pp. 4092-4095.

[55] S. Kurtz, *The UHMWPE Handbook: Ultra-High Molecular Weight Polyethylene in Total Joint Replacement*. San Diego, CA: Elsevier Academic Press, 2004.

[56] J. Fortin and T.-m. Lu, *Chemical Vapor Deposition Polymerization: The Growth and Properties of Parylene Thin Films*. Norwell, Massachusetts: Kluwer Academic Publishers, 2004.

[57] Y.-S. Yeh*, et al.*, "Polymerization of <I>para</I>-xylylene derivatives. VI. morphology of parylene N and parylene C films investigated by gas transport characteristics," *Journal of Polymer Science Part B: Polymer Physics,* vol. 28, pp. 545-568, 1990.

[58] J. J. Senkevich*, et al.*, "The facile surface modification of poly(p-xylylene) ultrathin films," *Colloids and Surfaces A: Physicochemical and Engineering Aspects,* vol. 216, pp. 167-173, 2003.

[59] J. J. Senkevich*, et al.*, "Unique structure/properties of chemical vapor deposited parylene E," *Journal of Vacuum Science & Technology A: Vacuum, Surfaces, and Films,* vol. 20, pp. 1445-1449, 2002.

[60] T. Y. Chang*, et al.*, "Cell and protein compatibility of parylene-C surfaces," *Langmuir,* vol. 23, pp. 11718-11725, 2007.

[61] B. Evans III, "MEMS Capacitive Strain Sensing Elements for Integrated Total Knee Arthroplasty

Prosthesis Monitoring," Department of Mechanical, Aerospace, and Biomedical Engineering, University of Tennessee, Knoxville, 2007.

[62] B. Evans III, *MEMS Capacitive Strain Sensing Elements for Integrated Total Knee Arthroplasty*

Prosthesis Monitoring. Knoxville: University of Tennessee, 2007.

[63] L. M. Schutte*, et al.*, "An index for quantifying deviations from normal gait," *Gait & Posture,* vol. 11, pp. 25-31, 2000.

[64] R. D. Komistek*, et al.*, "Knee mechanics: a review of past and present techniques to determine in vivo loads.," *J. Biomech.,* vol. 38, 2005.

[65] R. Enoka, *Neuromechanics of Human Movement. Human Kinetics.*, 2008.

[66] D. J. Meldrum and C. E. Hilto, Eds., *From Biped to Strider: The Emergence of Modern Human Walking, Running and Resource Transport*. Springer, 2004, p.^pp. Pages.

[67] M. Shorten, "Plantar pressure distribution and footwear design," *Footwear Science,* vol. 1, pp. 88 - 90, 2009.

[68] B. E. Williams and J. D. Yakel, "Clinical Uses of In-Shoe Pressure Analysis in Podiatric Sports Medicine," *J. Am. Pod. Med.Ass.,* vol. 97, pp. 49-58, 2007.

[69] R. P. Dutton*, et al.*, "Preliminary trial of a noninvasive brain acoustic monitor in trauma patients with severe closed head injury," *J Trauma,* vol. 53, pp. 857-63, Nov 2002.

[70] G. C. Steinbach*, et al.*, "Intracranial pressure dynamics assessed by noninvasive ultrasound during 30 days of bed rest," *Aviat Space Environ Med,* vol. 76, pp. 85-90, Feb 2005.

[71] C. E. Counsell and R. Grant, "Incidence studies of primary and secondary intracranial tumors: a systematic review of their methodology and results," *J Neurooncol,* vol. 37, pp. 241-50, May 1998.

[72] M. Gelabert-Gonzalez*, et al.*, "The Camino intracranial pressure device in clinical practice. Assessment in a 1000 cases," *Acta Neurochir (Wien),* vol. 148, pp. 435-41, Apr 2006.

[73] R. D. Dickerman*, et al.*, "Intra-ocular pressure changes during maximal isometric contraction: Does this reflect intra-cranial pressure or retinal venous pressure?," *Neurological Research,* vol. 21, pp. 243-246, Apr 1999.

[74] M. Gelabert-González*, et al.*, "The Camino intracranial pressure device in clinical practice. Assessment in a 1000 cases," *Acta Neurochirurgica,* vol. 148, pp. 435-441, 2006.

Appendix A: Experimental Code

7.1. Savitzky-Golay Smoothing and Baseline Correction in Matlab

```
% Enter raw data

     x = rawdata(:,1);   % time
     y = rawdata(:,2);   % capacitance

% Separate a priori zero load sections of data from
% calibration data stream

     for j=1:length(iso)
         for i=1:length(isodata)
             if i > iso(j,1) && i < iso(j,2)
                 isodata(i)= y(i);
             else
                 i=i+1;
             end
         end
     end

Plot data


% High frequency noise removal

Apply 7th order 7.1. Savitzky - Golay filter on y

     window size 51


% Low frequency noise removal (baseline correction)

Apply 12th order Savitzky - Golay filter on isodata

     window size data length / 3


% Adjust raw data accordingly

     for i=1:length(y)

     Baseline_corrected(i) = y(i)-Low_filtered(i);

     Total_corrected(i) = High_filtered(i)-Low-Filtered(i);

     end

% Plot output
```

7.2. Capacitance to Digital Microcontroller Program for Labview

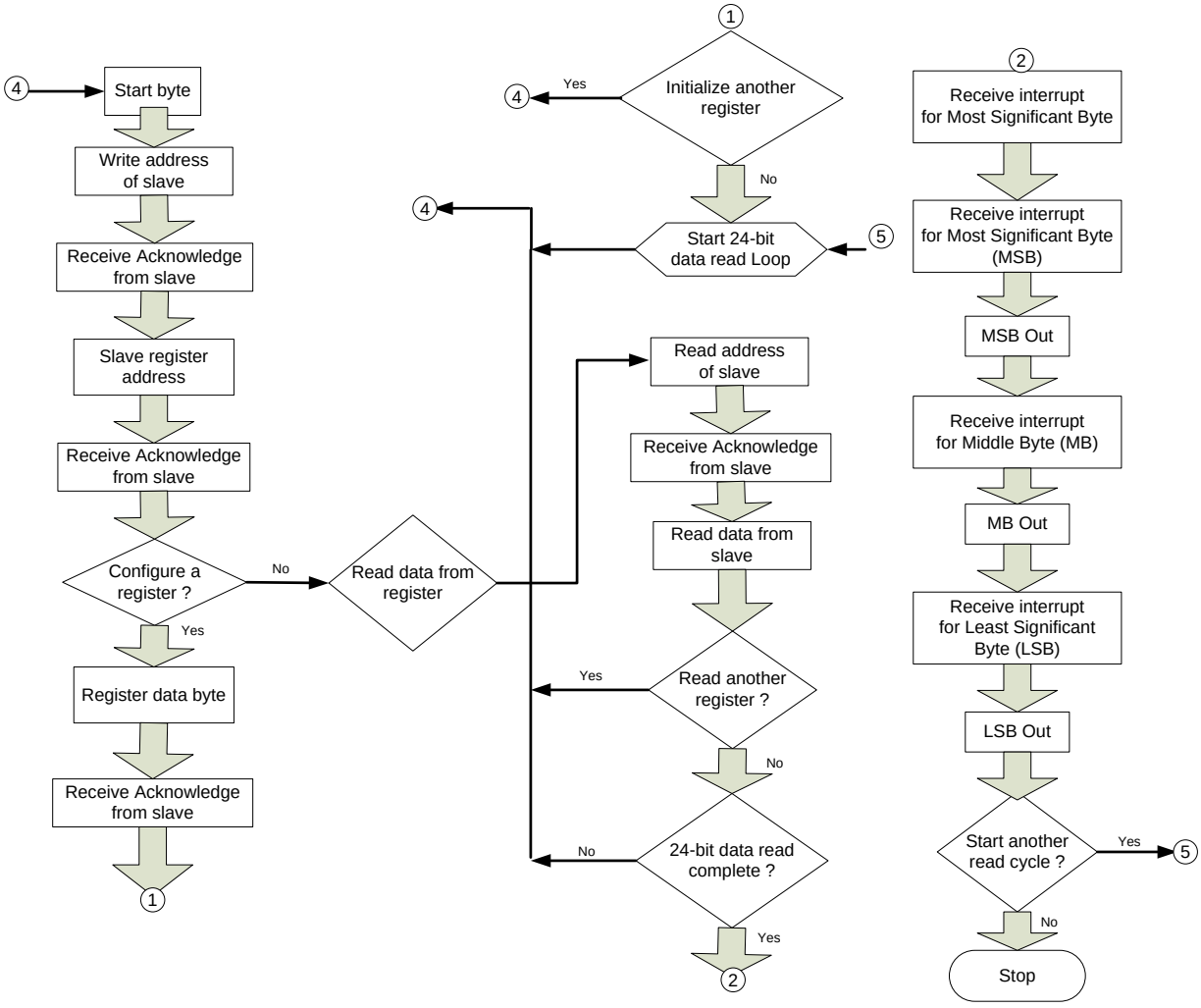

Figure 91. Flow diagram showing microcontroller program for Labview interface.

Appendix B: Technical Specifications

Table 9. Bluetooth-enabled sensing instrument specifications.

Sensor Nominal Capacitance	5 pF
Sensors per condyle	918
Total sensors present	1836
Spatial resolution (raw)	0.5 mm
Max number of sensors supported by board	1024
Analog input channels	64
CDC input range	0-8 pF
ADC resolution	24 bit
ADC resolution (effective)	21 bit
Excitation frequency	32 Hz
Offset error	32 aF
Power supply	1.8-3.3V
Switching time	programmable
Modulation	pi/4 DQPSK
Carrier frequency	2.4 GHz
Max data rate	2 Mbps

Vita

Emily Reagan Pritchard was born in Nashville, Tennessee, and raised in Johnson City, Tennessee. She graduated from Science Hill High School in 2002, and completed a Bachelor of Science in Biomedical Engineering at the University of Tennessee, Knoxville, in 2006. She completed an internship at the Oak Ridge National Laboratory in 2004 during her undergraduate studies. In 2006, she entered the Ph.D. program in Biomedical Engineering at the University of Tennessee, Knoxville. From 2004-2010, she worked at the Center for Musculoskeletal Research under Dr. Mohamed Mahfouz on projects including smart instruments, anatomical and implant analysis, and fluoroscopic in vivo kinematic studies. She graduated with her Ph.D. in Biomedical Engineering in May 2010.